UNIVERSITY OF CALIFORNIA, SAN DIEGO

Enhanced Light-Matter Interactions for Biosensing

A Dissertation submitted in partial satisfaction of the requirements for the degree of Doctor of Philosophy

in

Chemical Engineering

by

Brandon Christian Marin

Committee in charge:

Professor Darren J. Lipomi, Chair
Professor Olivia A. Graeve
Professor Jesse V. Jokerst
Professor Noah Malmstadt
Professor Donald J. Sirbuly

2017

This dissertation of Brandon Christian Marin is approved, and it is acceptable in quality and form for publication on microfilm and electronically:

Chair

University of California, San Diego

2017

DEDICATION

This thesis is dedicated to my wife, Anastasia.

EPIGRAPH

“If you only do what you can do, you'll never be better than what you are.”

TABLE OF CONTENTS

LIST OF FIGURES

LIST OF TABLES

ACKNOWLEDGEMENTS

My thesis has truly been a journey. At the very least, it has made me a well-rounded scientist with exposure to a variety of extremely technical topics. The most valuable take-away from this experience has been the people: *the friendships and relationships that were born of this thesis and those that laid the foundation for this thesis.*

David Halushka has been a friend and source of inspiration for the last decade. Dave has been there for me through the lows and highs and done nothing but support me in my journey over the last decade. At the very least, he has been an inadvertent distraction from my own vexing, imagined or real. Truck Torrence and Max Goldman are two of my best friends, and their friendships have provided a world of jocularity that served as a glorious escape from the daily droll of graduate school. Jessica Gao is one of my oldest friends, and has been there through thick and thin and her support means the world to me. Unofficially, you could even say that Jessica Gao wrote this thesis![†] Max Bernstein keeps me on my toes. I need to thank Kunaal Kanagal for all the late study nights at Medici and Visconti that resulted in me getting into graduate school. Kunaal is another one of my best friends, and his friendship is priceless to me. Justin Shahbaz is a dear friend I met at USC and has been a confidant to me for over 15 years now. Justin is like a brother to me, and his humor has truly made this thesis a more tolerable one. ([†]Jessica Gao did not write this thesis)

Chaitanya Rama Murthy deserves his own paragraph so here it is.

Doug Graham and Donna Owens were some of my high school teachers. Mr. Graham taught me calculus, and Mrs. Owens taught me chemistry and physics. They taught me that an erratic, misbehaving, wise-cracking, Mexican, skateboarder kid could be

anything that he wanted to be, granted that he was willing to work hard for it. Mr. Graham helped me build my confidence in math, which follows me to this very day. Interestingly, math was a topic I was not comfortable with until I took his course. Mrs. Owens noticed that I did really well on her exams, but also had to constantly reprimand me in her class for being a distraction to other students. One day, she came to me after class and said "I don't know why I am doing this, but I think you would be a good fit for our Science Bowl team. We will compete at Caltech later this year." With her recommendation, I joined Science Bowl and my love for engineering was seeded. I owe these two teachers so much, I hope one day they read this acknowledgement and know that their efforts changed my life. Noah Malmstadt and Theodore Tsotsis have been my greatest champions at USC. I am grateful for their tireless support and encouragement.

I'd like to thank Lindsay Freeman for motivating me to apply to graduate school and Josh Villanueva and Olivia Simpson for their friendship. Conor Riley has been a welcome source of funny pictures, caustic hallway conversations, and high-energy jam sessions (as well as Kyle Mooney). Thanks to Peter Chung for wandering into my life in 2012 and putting up with me for so many years after, I am really lucky to have you as a beloved friend and jam buddy. I am very grateful for the help and support of Professor Andrea Tao, my first PhD faculty advisor. Although it didn't work out in the end, Andrea has been nothing but a constant supporter and advocate of my education since I started in her group back in 2012. Back then, Andrea pushed for my acceptance to the NanoEngineering department, a decision that has reshaped my life for the better. All that Andrea asked in return was that I "fiercely prove" that my acceptance was deserved. I hope

that I have done so in the past 5 years. Thank you, Andrea, for all the guidance, shared experience, and support.

The Tao Research Group was my first research group as a PhD student and has been nothing but supportive, even since my departure in 2015. I have spent more hours with Tyler Dill than anyone else in the department, he has been an endless source of ingenuity, knowledge, support, cross-examination, and friendship. I'd like to thank Andrea Rodarte for being a constant source of laughter and witty responses. Yahya Alvi and David Rosen were the first undergraduates I worked with at UC San Diego and to this day are the most creative and brightest that I have ever met. Whitney Bryks (AKA Whitey) is one of the funniest and sharpest scientists I know, I am proud to have him join me at Intel after graduation and even prouder to have him as a friend. Guru Kargal is just the best, I miss him and his peculiar sense of humor.

Professor David Miller has been an inspiration to me as an educator. His tireless efforts set the bar for me as a teaching assistant under his tutelage. This resulted in the UCSD Senate Distinguished Teaching Award, which he wrote me a recommendation for. The Jacobs School of Engineering and I are eternally indebted to Dave Miller for his service to the community as an educator.

The Lipomi Research Group. Charles Dhong for an introduction to full-blown lizard brain (full walnut) and completely wrapping the Orion heat exchanger with thermally insulative foam. I have known Julian Ramirez since he was an undergraduate; he has developed into an excellent researcher and I thank him for his help as a colleague. I'd like to thank Daniel Rodriquez for keeping the lab sense of humor on point and his help in shaking the cages. I'd like to thank Adam Printz for his friendship, support, and peculiar

sense of humor. Suchol Savagatrup started graduate school with me, and became one of my closest confidants; I am grateful to have him in my life. Sam Root is one of my best friends, I'd like to thank him for putting up with me and for his willingness to disregard responsibility to spend time with me and make hot-dog lips. Thanks to Mickey Finn III for taking the reins on the Orion. Thanks to Andrew Kleinschmidt for being a friend and the voice of reason in the lab. Thanks to Fumitaka for tolerating me as a desk neighbor and is wisdom in chemistry. Thanks to Laure Kayser for being a friend, colleague and for always being down to explore San Diego county. Thanks to Tim F. O'Connor III for fighting the good fight with me for 5 years.

Professor Darren John Lipomi is truly an inspiration to his field and profession. Never have a met an academic so committed the people around him, his efforts have been indispensable in shaping me to be the researcher I am today. Darren's innovation and creativity in his work is infectious, which is refreshing in a field that has become increasingly pedestrian. I truly feel like I found my home in academia when I joined Darren's group, his genuine care for his students has created a unique dynamic that fosters growth in the highest degree. The world is a better place with Darren in it, I cherish his friendship and I am grateful to have him as an advisor.

I would like to thank my mother, Evelyn, for showing me what strength is. I would like to thank my sister, Ash-leigh, for her infinite support and love. I'd like to thank my father, Frank, for showing me how to laugh and how to enjoy life.

Above all things I would like thank my wife, Anastasia. She has taught me what true love is. She has been my rock and I could not have pushed through this endeavor

without her immeasurable support and care. I am so happy to have this woman (women?) in my life and I can't wait to see what the next chapter has in store for us.

I also include the following acknowledgements below as required by the University of California, San Diego:

Chapter 2, in full, is a reprint of the material as it appears in *ACS Photonics*, 2016, 3 (4), 526- 531. The American Chemical Society, 2016. **Brandon C. Marin**, ‡ Su-wen Hsu, ‡ Li Chen, Ashley Lo, Darwin W. Zwissler, Zhaowei Liu, and Andrea R. Tao. (‡ Equal contribution). The dissertation author was the primary investigator and author of this paper.

Chapter 3, in part, is currently being prepared for submission for publication of the material by **Brandon C. Marin**, ‡ Sameer S. Walavalkar, ‡ Chieh-feng Chang, ‡ Andrea R. Tao, Axel Shearer, and Scott Fraser. (‡ Equal contribution). The dissertation author was the primary investigator and author of this material.

Chapter 4, in part, is currently being prepared for submission for publication of the material by **Brandon C. Marin**, Julian Ramirez, Eden Aklile, and Darren J. Lipomi. The dissertation author was the primary investigator and author of this material.

Chapter 5, in full, is a reprint of the material as it appears in *Nanoscale*, 2017, 6, 1292-1298. The Royal Society of Chemistry, 2017. **Brandon C. Marin**, Justin Liu, Eden Aklile, Armando D. Urbina, Andrew S-C. Chiang, Natalie Lawrence, Shaochen Chen, and Darren J. Lipomi. The dissertation author was the primary investigator and author of this paper.

Chapter 6, in full, is a reprint of the material as it appears in *ACS Omega*, 2017, 2(2), 626-630. The American Chemical Society 2017. **Brandon C. Marin**, Samuel E.

Root, Armando D. Urbina, Eden Aklile, Rachel Miller, Aliaksandr V. Zaretski, and Darren J. Lipomi. The dissertation author was the primary investigator and author of this material.

Appendix A, in full, is a reprint of the material as it appears in *ACS Photonics*, 2016, 3 (4), 526- 531. The American Chemical Society, 2016. **Brandon C. Marin**, ‡ Su-wen Hsu, ‡ Li Chen, Ashley Lo, Darwin W. Zwissler, Zhaowei Liu, and Andrea R. Tao. (‡ Equal contribution). The dissertation author was the primary investigator and author of this paper.

Appendix B, in part, is currently being prepared for submission for publication of the material by **Brandon C. Marin**, ‡ Sameer S. Walavalkar, ‡ Chieh-feng Chang, ‡ Andrea R. Tao, Axel Shearer, and Scott Fraser. (‡ Equal contribution). The dissertation author was the primary investigator and author of this material.

Appendix C, in full, is a reprint of the material as it appears in *Nanoscale*, 2017. The Royal Society of Chemistry, 2017. **Brandon C. Marin**, Justin Liu, Eden Aklile, Armando D. Urbina, Andrew S-C. Chiang, Natalie Lawrence, Shaochen Chen, and Darren J. Lipomi. The dissertation author was the primary investigator and author of this paper.

Appendix D, in full, is a reprint of the material as it appears in *ACS Omega*, 2017, 2(2), 626-630. The American Chemical Society 2017. **Brandon C. Marin**, Samuel E. Root, Armando D. Urbina, Eden Aklile, Rachel Miller, Aliaksandr V. Zaretski, and Darren J. Lipomi. The dissertation author was the primary investigator and author of this material.

.

VITA

2011	Bachelor of Science in Chemical Engineering. University of Southern California
2012	Engineer. Sinpex Corporation and Baxter International
2012-2017	Graduate Researcher. University of California, San Diego
2013	Master of Science in NanoEngineering. University of California, San Diego
2013-2014	Teaching Assistant. Department of NanoEngineering, University of California, San Diego
2014-2015	Technical Engineering Intern. Intel Corporation
2015-2016	Teaching Assistant. Department of NanoEngineering, University of California, San Diego
2017	Doctor of Philosophy in Chemical Engineering, University of California, San Diego
2017	Research and Development Semiconductor Packaging Engineer. Intel Corporation

PUBLICATIONS

Brandon C. Marin, Julian Ramirez, Eden Aklile, Darren J. Lipomi. "Graphene-metal composites for chemical, mechanical and optical sensing." (***In preparation***)

Brandon C. Marin, Samuel E. Root, Armando D. Urbina, Eden Aklile, Rachel Miller, Aliaksandr V. Zaretski, Darren J. Lipomi "Graphene-metal composite sensors with near-zero temperature coefficient of resistance," *ACS Omega*, **2017**, 2(2), 626-630, DOI: 10.1021/acsomega.7b00044

Brandon C. Marin, Justin Liu, Eden Aklile, Armando Urbina, Andrew S-C. Chiang, Shaochen Chen, Darren J. Lipomi "Piezoplasmonic Effect in Metallic Nanoislands- Strain Sensing using SERS," *Nanoscale*, **2017**, 9, 1292-1298, DOI: 10.1039/C6NR09005B

Brandon C. Marin,‡ Su-Wen Hsu,‡ Li Chen, Ashley Lo, Darwin Zwissler, Zhaowei Zhu, Andrea Tao "Plasmon-Enhanced Two-Photon Absorption in 'All-in-One' Photoluminescent Semiconductor Nanocrystals," *ACS Photonics*, **2016**, 3(4), 526-531, DOI: 10.1021/acsphotonics.6b00037.

Aliaksandr V. Zaretski, **Brandon C. Marin**, Herad Moetazedi, Tyler Dill, Andrea R. Tao, and Darren J. Lipomi, "Using the Thickness of Graphene to Template Lateral Sub-Nanometer Gaps between Gold Nanostructures," *NanoLetters*, **2015**, 15(1), 635-640, DOI: 10.1021/nl504121w.

Laura Lazarus,‡ Carson T. Riche,‡ **Brandon C. Marin**, Malancha Gupta, Noah Malmstadt, Richard Brutchey, "Two-Phase Microfluidic Droplet Flows of Ionic Liquids for the Synthesis of Gold and Silver Nanoparticles," *Applied Materials and Interfaces*, **2012**, 4(6), 3077-3083, DOI: 10.1021/am3004413. (**cover article**)

Carson T. Riche, **Brandon C. Marin**, Noah Malmstadt, Malancha Gupta, "Vapor Deposition of Cross-linked Fluoropolymer Barrier Coatings onto Pre-assembled Microfluidic Devices," *Lab on a Chip*, **2011**, 11, 3049-3052, DOI: 10.1039/C1LC20396G. (**cover article**)

‡Equal contribution

ABSTRACT OF THE DISSERTATION

Enhanced Light-matter Interactions for Biosensing

by

Brandon Christian Marin

Doctor of Philosophy in Chemical Engineering

University of California, San Diego, 2017

Professor Darren J. Lipomi, Chair

Metallic nanostructures can confine light to nanoscale dimensions through surface plasmon resonance, leading to extraordinary effects such as enhancements in light emission and scattering. This thesis explores the use of these enhanced light-matter interactions for applications in optical biosensing. First, we demonstrate plasmon-enhanced multiphoton absorption in covellite-phase copper sulfide (CuS) nanocrystals. The near-infrared plasmon resonance wavelength of these semiconductor nanocrystals is tuned towards the two-photon absorption edge using selenium doping. This tuning results in a 300% enhancement in the two-photon action cross section, resulting in a "brightness" that is an order of magnitude greater than conventional fluorophores. The resulting luminescence demonstrates the efficacy of CuS nanocrystals as a solid-state dye for biological imaging. CuS nanocrystals also offer the first "all-in-one" platform for studying plasmon-exciton coupling without the need for a physicochemical interface between the plasmonic and excitonic materials. Second, the use of lithographically-patterned gold nanobulbs for detection of complex bioanalytes using surface-enhanced Raman scattering (SERS) is reported. Highly uniform SERS enhancement factors in these gold nanobulbs permit the use of 2D-correlation spectroscopy for the identification of molecular rearrangement and complementary binding in single-stranded DNA. Third, we demonstrate the use of metal nanoislands on graphene for strain sensing using SERS. These metal nanoisland-graphene composite films contain gaps between the nanoislands which behave as hot spots for SERS when functionalized with benzenethiolate. Mechanical strain increases the sizes of the gaps; this increase attenuates the electric field and the resultant SERS signal. This compounded, SERS-enhanced "piezoplasmonic" effect can be quantified using a plasmonic gauge factor, and is among the most sensitive mechanical sensors of any type.

These sensors can detect tensile deformations of less than 0.04% with a resolution of less than 0.002%. Since the nanoisland-graphene composites are thin films that are both conductive and optically active, they permit simultaneous electrical stimulation of myoblast cells and optical detection of the strains produced by the cellular contractions. Last, we demonstrate a method to fabricate metal nanoisland-graphene composites with a temperature coefficient of resistance (TCR) that is close to zero. A thin film with this property can be used as a piezoresistive sensor that is stable against temperature fluctuations of the type encountered in the real world—e.g., in a wearable sensor. The stability of a sensor fabricated with this method is demonstrated by subjecting a wearable pulse sensor to simulated solar irradiation.

Chapter 1

An Introduction to Enhanced-Light Matter Interactions and Applied Plasmonics

Brandon C. Marin [a]

[a] *NanoEngineering Department, University of California, San Diego. 9500 Gilman Drive MC 0448, La Jolla, CA 92093-0448*

1.1 Overview

My thesis work can be summarized into three main topics: (1) the fabrication of nanostructures, (2) their applications for optical biosensing, and (3) increasing their sensitivity for biosensing using enhanced light-matter interactions. The fabrication aspect (1) discusses both top-down and bottom-up techniques used in this thesis for the assembly of nanostructures. The optical biosensing aspect (2) of this thesis includes sensing primarily through scattering and fluorescence spectroscopy. Lastly, the enhanced light-matter interactions (3) are facilitated through plasmons – collective oscillations of electrons that have the ability to confine light to sub-wavelength dimensions and subsequently enhance their interactions with surrounding matter. The concept of plasmons, and their applications, will be briefly expanded upon and discussed further in this chapter.

1.2 Plasmonics: A Brief Introduction

Quasiparticles are systems of individual particles that collectively interact with matter in a particular way, first postulated by Lev Landau in his seminal works on Fermi fluids in the late 1950s.[1,2] One of the simplest examples of a quasiparticle is the phonon, which is a collective oscillation, or vibration, of atoms in a lattice. We observe phonons through sound, and interpret different resonant frequencies of oscillations through different tones. The quasiparticle of greatest interest in this thesis is the plasmon. A plasmon is the collective oscillation of conduction electrons in a metal at a dielectric interface and was first described by Rufus Ritchie in 1957.[3] Generally, a plasmon is instigated by an oscillating electric field (like light, an electric-field wave) at a metal-dielectric interface. The oscillating electric field exerts an oscillatory force on the weakly bound electrons of

the metal. The electrons respond by also oscillating, an interaction known as "coupling" between the incident electric field and the labile electrons. The mobile electrons act as a plasma, (which is the reasoning behind the term *plasmon*, a portmanteau of electron and plasma) and are sensitive to other electromagnetic phenomena in their labile state. The study of plasmons and their applications in applied science is known as a plasmonics. Plasmonics has been a field of ardent work in the last half-century since its inception. Applications have ranged from optical rulers[4], waveguides,[5,6,7,8,9] enhanced emissive phenomena,[10,11,12,13,14] subwavelength lensing,[15] extraordinary transmission,[16,17,18] optical cloaking,[19],[20] negative refractive index materials,[19] hyperbolic metamaterials,[21] and even single-molecule spectroscopy.[22,23,24] A plethora of work exists that described the field of plasmonics. However, I will give a brief and very simple introduction to plasmons and applied plasmonics as they pertain to the scope of the work covered in this thesis. *The goal of this chapter is to introduce applied plasmonics in a way that is digestible to anyone who has a rudimentary understanding of how electricity and light works, and to entice the reader to consider the more detailed chapters that follow*. A formal description of the field of plasmonics is covered in masterly detail by Stefan Maier, and can be referenced for much greater detail and theoretical frameworks.[25]

When the oscillation of electrons in a plasmon is confined geometrically in a nanostructure, it is called a localized-surface plasmon (LSP). An LSP is a non-propagating phenomenon, coupled to an incident electromagnetic (EM) wave (i.e., light), and occurs in nanostructures with surfaces that exhibit a high radius of curvature with respect to the incident wavelength. Conveniently, the curvature provides a restoring force by electrostatic repulsion when the electron plasma is focused to a point. The simplest case is a sphere,

where the focal point is at the poles of the sphere for a dipole mode oscillation. The salient feature behind LSPs is the amplification of the electric field (called the "near-field enhancement") that results from the accumulation of charge as the electron plasma is spatially focused during different periods in the oscillation. This leads to interesting effects such as the sub-wavelength lensing of light, nanoscale heating, and enhanced emissive effects. All of these phenomena are a consequence of the extraordinary concentration of light that results from the accumulation of charge and coupled electric field in an LSP mode.

1.3 Applied Plasmonics: Enhanced-Raman Scattering and Enhanced Photoemission

1.3.1 Raman Scattering and Spectroscopy

Raman scattering is the inelastic scattering of light, as opposed to elastic Rayleigh scattering. The phenomenon was first described by C.V. Raman,[26] who received a Nobel Prize in Physics in 1930 for his contributions. Raman spectroscopy is a type of vibrational spectroscopy, a molecular spectroscopy concerned with the vibration of individual atoms in a chemical moiety. Raman spectroscopy is similar to infrared absorption (IR) spectroscopy, but relies on the energy difference (Raman shift) between incident and Raman scattered light from a sample to determine the resonance energies of vibration. This is in contrast to IR spectroscopy, which relies on the wavelength absorbed to determine the resonance energies of vibration. Furthermore, IR and Raman differ in their selection rules and thus give different information on a chemical compound. IR spectroscopy relies on the change in dipole moment of a chemical bond, while Raman spectroscopy relies on a change in polarizability. Thus, bonds with a strong dipole moment (such as those associated with

carbonyls, nitriles, and halides) are defined as IR-active, while bonds that are highly polarizable are defined as Raman-active.

1.3.2 Surface-Enhanced Raman Scattering

The Raman effect is inherently weak, only 1 out of every 10,000,000 photons is inelastically scattered. Thus, Raman spectroscopy is relegated to using powerful lasers as excitation sources. Interestingly, the high polarizability of an LSP formed by a nanostructured surface can enhance Raman scattering, a phenomena known as the surface-enhanced Raman scattering (SERS) effect. This effect was first reported by Van Duyne and coworkers in 1977.[27] Since then, numerous groups have exploited this technique for mechanical, chemical, and biological sensing. The sensitivity of SERS has been pursued to the limit of single molecule spectroscopy. While astonishing boosts in signal can be achieved, it is vital that the analyte of interest be placed in close proximity (< 20 nm) to the metal interface that contains the LSP for any appreciable enhancement.

1.3.3. Enhanced Emissive Processes

Fluorescence is an emissive phenomenon where a photon is absorbed by molecule and subsequently emitted. The emitted photon is usually lower in energy than the absorbed photon, mostly due to heat dissipation during electronic transitions. Enhanced fluorescence by LSPs can be achieved and has been reported in various nanostructures and schemes.[12,28,29,30] Similar to SERS, the fluorophore must be in close proximity to the metal interface that contains the LSP. However, care must be taken to prevent quenching, which occurs when the fluorophore is close enough to metal surface to allow non-radiative transitions at the physicochemical interface. Solid-state materials, such as transition metal-chalcogenide nanoparticles, have also been reported to demonstrate enhanced linear[14,31] and nonlinear

emissive processes as a result of LSPs. Nonlinear processes include both multi-photon absorption[32] and second-harmonic generation.[33]

1.4 Organization of Chapters

The remainder of this thesis is dedicated to my contributions to the previously described phenomena in this chapter. Particularly, these contributions focus around applications in biological sensing and involve various top-down and bottom up nanofabrication techniques to assemble the experimental platforms necessary for these studies.

Chapter 2 is dedicated to my work on the enhanced emission of covellite-phase copper sulphide (CuS) nanodisks for applications as a solid-state contrast agent for multi-photon microscopy. It involves plasmon-enhanced absorption and subsequent enhanced emission of the CuS nanodisks, by tuning the plasmon resonance to overlap with the two-photon absorption edge. Tuning is achieved by selenium doping, which blue-shifts the plasmon resonance. This study involves a completely bottom-up nanofabrication technique: colloidal synthesis.

Chapter 3 involves the fabrication of gold nanobulbs and their applications as SERS-based biosensors. The nanobulbs are assembled using electron-beam lithography, dry etching, and DC sputtering: a hybrid top-down/bottom-up technique.

Chapter 4 involves an introduction and review on metal-graphene composites, particularly metal-decorated graphene or “metal nanoislands.” I spent the final year of my PhD studying metal-decorated graphene. Chapter 4 discusses metal-graphene composites for mechanical, chemical, energy storage, and optical applications.

Chapter 5 is dedicated to metal nanoislands for SERS-based optical strain sensing in muscoskeletal cells. It involves the discussion and characterization of a "piezoplasmonic" response that was observed.

Chapter 6 is dedicated to the development of a method to fabricate metal nanoislands that were thermal-drift resistant in piezoresistive sensing. Software and parameterization were developed to establish design rule for different metals. Additionally, a wearable application for the sensor was demonstrated.

References

(1) Landau, L. D. On the Theory of the Fermi Liquid. *Sov. Phys. JETP* 1959, *35*, 70–74.

(2) Landau, L. D. The Theory of a Fermi Liquid. *Sov. Phys. JETP* 1957, *3*, 920.

(3) Ritchie, R. H. Plasma Losses by Fast Electrons in Thin Films. *Phys. Rev.* 1957, *106*, 874–881.

(4) Jain, P. K.; Huang, W.; El-Sayed, M. a. On the Universal Scaling Behavior of the Distance Decay of Plasmon Coupling in Metal Nanoparticle Pairs: A Plasmon Ruler Equation. *Nano Lett.* 2007, *7*, 2080–2088.

(5) Choo, H.; Kim, M.-K.; Staffaroni, M.; Seok, T. J.; Bokor, J.; Cabrini, S.; Schuck, P. J.; Wu, M. C.; Yablonovitch, E. Nanofocusing in a Metal–insulator–metal Gap Plasmon Waveguide with a Three-Dimensional Linear Taper. *Nat. Photonics* 2012, *6*, 838–844.

(6) Holmgaard, T.; Bozhevolnyi, S. I.; Markey, L.; Dereux, A. Dielectric-Loaded Surface Plasmon-Polariton Waveguides at Telecommunication Wavelengths: Excitation and Characterization. *Appl. Phys. Lett.* 2008, *92*, 011124.

(7) Maier, S. A.; Kik, P. G.; Atwater, H. A.; Meltzer, S.; Requicha, A. A. G.; Koel, B. E. Observation of Coupled Plasmon-Polariton Modes of Plasmon Waveguides for Electromagnetic Energy Transport below the Diffraction Limit. *Proc. SPIE* 2002, *4810*, 71–81.

(8) Shin, W.; Cai, W.; Catrysse, P. B.; Veronis, G.; Brongersma, M. L.; Fan, S. Broadband Sharp 90-Degree Bends and T-Splitters in Plasmonic Coaxial Waveguides. *Nano Lett.* 2013, *13*, 4753–4758.

(9) Wang, W.; Yang, Q.; Fan, F.; Xu, H.; Wang, Z. L. Light Propagation in Curved Silver Nanowire Plasmonic Waveguides. *Nano Lett.* 2011, *11*, 1603–1608.

(10) Manjavacas, A.; Abajo, F. J. G. De; Nordlander, P. Quantum Plexcitonics: Strongly Interacting Plasmons and Excitons. *Nano Lett.* 2011, *11*, 2318–2323.

(11) Imura, K.; Nagahara, T.; Okamoto, H. Near-Field Two-Photon-Induced Photoluminescence from Single Gold Nanorods and Imaging of Plasmon Modes. *J. Phys. Chem. B* 2005, *109*, 13214–13220.

(12) Kano, H.; Kawata, S. Two-Photon-Excited Fluorescence Enhanced by a Surface Plasmon. *Opt. Lett.* 1996, *21*, 1848–1850.

(13) Achermann, M. Exciton-Plasmon Interactions in Metal-Semiconductor Nanostructures. *J. Phys. Chem. Lett.* 2010, *1*, 2837–2843.

(14) Schietinger, S.; Barth, M.; Aichele, T.; Benson, O. Plasmon-Enhanced Single Photon Emission from a Nanoassembled Metal-Diamond Hybrid Structure at Room Temperature. *Nano Lett.* 2009, *9*, 1694–1698.

(15) Lin, L.; Goh, X. M.; McGuinness, L. P.; Roberts, A. Plasmonic Lenses Formed by Two-Dimensional Nanometric Cross-Shaped Aperture Arrays for Fresnel-Region Focusing. *Nano Lett.* 2010, *10*, 1936–1940.

(16) Roth, R. M.; Panoiu, N. C.; Adams, M. M.; Dadap, J. I.; Osgood, Jr., R. M. Polarization-Tunable Plasmon-Enhanced Extraordinary Transmission through Metallic Films Using Asymmetric Cruciform Apertures. *Opt. Lett.* 2007, *32*, 3414.

(17) Cui, Y.; He, S. Enhancing Extraordinary Transmission of Light through a Metallic Nanoslit with a Nanocavity Antenna. *Opt. Lett.* 2008, *34*, 16.

(18) Walavalkar, S. S.; Latawiec, P.; Homyk, A. P.; Scherer, A. A. Scalable Method for the Fabrication and Testing of Glass-Filled, Three-Dimensionally Sculpted Extraordinary Transmission Apertures. *Nano Lett.* 2014, *14*, 311–317.

(19) Shalaev, V. M. Optical Negative-Index Metamaterials. *Nat. Photonics* 2007, *1*, 41–48.

(20) Miller, O. D.; Polimeridis, A. G.; Reid, M. T. H.; Hsu, C. W.; DeLacy, B. G.; Joannopoulos, J. D.; Soljačić, M.; Johnson, S. G. Fundamental Limits to the Optical Response of Lossy Media. *Opt. Express* 2015, 1–23.

(21) Nasari, H.; Abrishamian, M. S.; Berini, P. Nonlinear Optics of Surface Plasmon Polaritons in Subwavelength Graphene Ribbon Resonators. *Opt. Express* 2016, *24*, 708.

(22) Etchegoin, P. G.; Meyer, M.; Le Ru, E. C. Statistics of Single Molecule SERS Signals: Is There a Poisson Distribution of Intensities? *Phys. Chem. Chem. Phys.* 2007, *9*, 3006–3010.

(23) Dieringer, J. A.; Lettan, R. B.; Scheidt, K. A.; Van Duyne, R. P. A Frequency Domain Existence Proof of Single-Molecule Surface-Enhanced Raman Spectroscopy. *J. Am. Chem. Soc.* 2007, *129*, 16249–16256.

(24) Kneipp, K.; Kneipp, H. Surface-Enhanced Raman Scattering in Local Optical Fields of Silver and Gold Nanoaggregates S From Single-Molecule Raman Spectroscopy to Ultrasensitive Probing in Live Cells Single-Molecule Raman Scattering in Local. 2006, 443–450.

(25) Maier, S. A. *Plasmonics- Fundamentals and Applications*; 1st ed.; Springer: New York, New York, 2007.

(26) Raman, C. V.; Krishnan, K. S. A New Type of Secondary Radiation. *Nature* 1928, *121*, 501–502.

(27) Jeanmaire, D. L.; Van Duyne, R. P. Surface Raman Spectroelectrochemistry. *J. Electroanal. Chem. Interfacial Electrochem.* 1977, *84*, 1–20.

(28) Lakowicz, J. R. Plasmonics in Biology and Plasmon-Controlled Fluorescence. *Plasmonics* 2006, *1*, 5–33.

(29) Ghosh, D.; Chattopadhyay, N. Gold Nanoparticles: Acceptors for Efficient Energy Transfer from the Photoexcited Fluorophores. *Opt. Photonics J.* 2013, *03*, 18–26.

(30) Wang, T.; Halaney, D.; Ho, D.; Feldman, M. D.; Milner, T. E. Two-Photon Luminescence Properties of Gold Nanorods. *Biomed. Opt. Express* 2013, *4*, 584–595.

(31) Zhang, J.; Tang, Y.; Lee, K.; Ouyang, M. Tailoring Light-Matter-Spin Interactions in Colloidal Hetero-Nanostructures. *Nature* 2010, *466*, 91–95.

(32) Marin, B. C.; Hsu, S.-W.; Chen, L.; Lo, A.; Zwissler, D. W.; Liu, Z.; Tao, A. R. Plasmon-Enhanced Two-Photon Absorption in Photoluminescent Semiconductor Nanocrystals. *ACS Photonics* 2016, acsphotonics.6b00037.

(33) Airola, M.; Liu, Y.; Blair, S. Second-Harmonic Generation from an Array of Sub-Wavelength Metal Apertures. *J. Opt. A Pure Appl. Opt.* 2005, *7*, S118–S123.

Chapter 2

Plasmon-Enhanced Two-Photon Absorption in Photoluminescent Semiconductor Nanocrystals

Brandon C. Marin, [†a] Su-Wen Hsu, [†a] Li Chen,[b] Ashley Lo,[a] Darwin W. Zwissler,[a] Zhaowei Liu.[b] and Andrea R. Tao[a*]

([†] Equal contribution)

[a] *NanoEngineering Department, University of California, San Diego. 9500 Gilman Drive MC 0448, La Jolla, CA 92093-0448*

[b] *Department of Electrical and Computer Engineering. University of California, San Diego.*

Abstract

In this work, we demonstrate the two-photon fluorescence of covellite-phase copper sulfide nanodisks and investigate the role of the surface plasmon resonance on emission. Using selenium doping, we blue-shift the plasmon resonance towards the two-photon absorption edge. We observed a three-fold enhancement of emission in these samples and report two-photon action cross sections that are an order of magnitude greater than conventional fluorophores. These nanomaterials offer a novel "all-in-one" platform for engineering plasmon-exciton coupling in the absence of a physical or chemical interface.

2.1 Introduction

Two-photon absorbing (2PA) inorganic nanoparticles that are capable of upconverting near-infrared (NIR) light have the potential to enable a wide range of biophotonic applications, ranging from fluorescence imaging in live tissue[1,2,3,4] to photodynamic therapy[5] and clinical diagnostics.[6,7] Semiconductor quantum dots composed of metal chalcogenides[1,8,9] and Au nanoparticles[10,11,12,13] are the two main types of colloidal solid-state nanoparticles that are currently being explored as contrast agents for *in vivo* two-photon induced emission (2PE) imaging and spectroscopy. A major advantage of utilizing these types of solid-state nanoparticles is the ability to probe live tissue with much larger penetration depths, since NIR light encounters less intrinsic scattering within tissue than visible light. Bright 2PA nanoparticles that operate within the biological tissue transparency window (630-1300 nm) are particularly desirable for

reaching deep tissue for carrying out optical sectioning or achieving three-dimensional imaging.[7] In comparison to conventional organic dyes that are used in 2PE measurements, inorganic nanoparticles also exhibit reduced photobleaching and increased photostabilities.[6] Their chemical surfaces are also readily modified with specific chemistries for increased biocompatibility, cell or tumor targeting, and prolonged circulation upon systemic delivery into an organism.[14,15]

The synthesis of bright nanoparticle probes with large 2PE action cross-sections is still a major challenge. One strategy to increase the brightness of 2PA nanoparticles is to excite a localized surface plasmon resonance (LSPR) that serves as virtual state for NIR photon absorption (**Figure 2.1**).[16] For example, Au nanorods support a LSPR that is polarized along the longitudinal nanorod axis and can be excited between 700-1000 nm, depending on the nanorod aspect-ratio.[17] 2PA is generated by plasmon excitation in the NIR, while fluorescence in the visible range is generated by radiative decay from intraband transitions of Au.[11] However, the 2PE action cross-sections of Au nanorods and nanoparticles are inherently limited by the low fluorescence quantum efficiencies of Au, which is in the range of 10^{-4}.[18] Alternatively, organic dyes have also been demonstrated to exhibit enhanced 2PE when in the close vicinity of a plasmonic Ag or Au nanoparticle,[19,20] but coupling between the LSPR of the nanoparticle and the electronic transition of the dye in this multicomponent system is weak.[21]

The ability to excite an LSPR for enhanced 2PA properties and to obtain strong exciton emission from a single nanoparticle would be highly desired for 2PE measurements. Highly-doped semiconductor nanocrystals (SNCs) have the potential to serve as these “all-in-one” type nanoparticles. We and others have recently demonstrated

that SNCs that possess a large number of free carriers can support LSPR excitation in the NIR and exciton generation in the same structure.[22,23,24] For example, $Cu_{2-x}S$ is a self-doped semiconductor where the introduction of Cu vacancies in the crystal lattice produces hole carriers. $Cu_{2-x}S$ SNCs exhibit an LSPR mode in the NIR range, well below the bandgap energy (1.2 eV for Cu_2S).[22] Advantageously for 2PA, the LSPR of these SNCs can be explicitly tuned within the NIR to mid-IR wavelength ranges. We have characterized how $Cu_{2-x}S$ SNCs respond to changes in carrier density, including the effects of carrier density tuning on near- field confinement and plasmonic coupling.[25] We have also observed shape-dependent LSPRs for SNCs by demonstrating that $Cu_{2-x}S$ nanodisks possess both in-plane and out-of-plane dipolar LSPRs.[24,26] CuS (covellite) nanodisks, in particular, exhibit a strong in-plane dipolar mode that dominates the NIR extinction spectrum.

While the fluorescent and plasmonic properties of highly-doped SNCs have been studied extensively in recent years [22,25,26], very little work has been done to investigate the 2PA properties of these materials. In particular, very little is known about how LSPR excitation and tuning can affect the 2PA cross-sections of colloidal nanomaterials. In this work, we demonstrate the 2PA and 2PE properties of CuS nanodisks. We show that the wavelength of the in-plane LSPR mode is critical to 2PE enhancement and that 2PA can be tuned on- and off-resonance to observe these effects. Our results show that for 2PA that is tuned near the LSPR excitation wavelength, the 2PE intensity observed from CuS nanodisks can be increased by a three-fold enhancement.

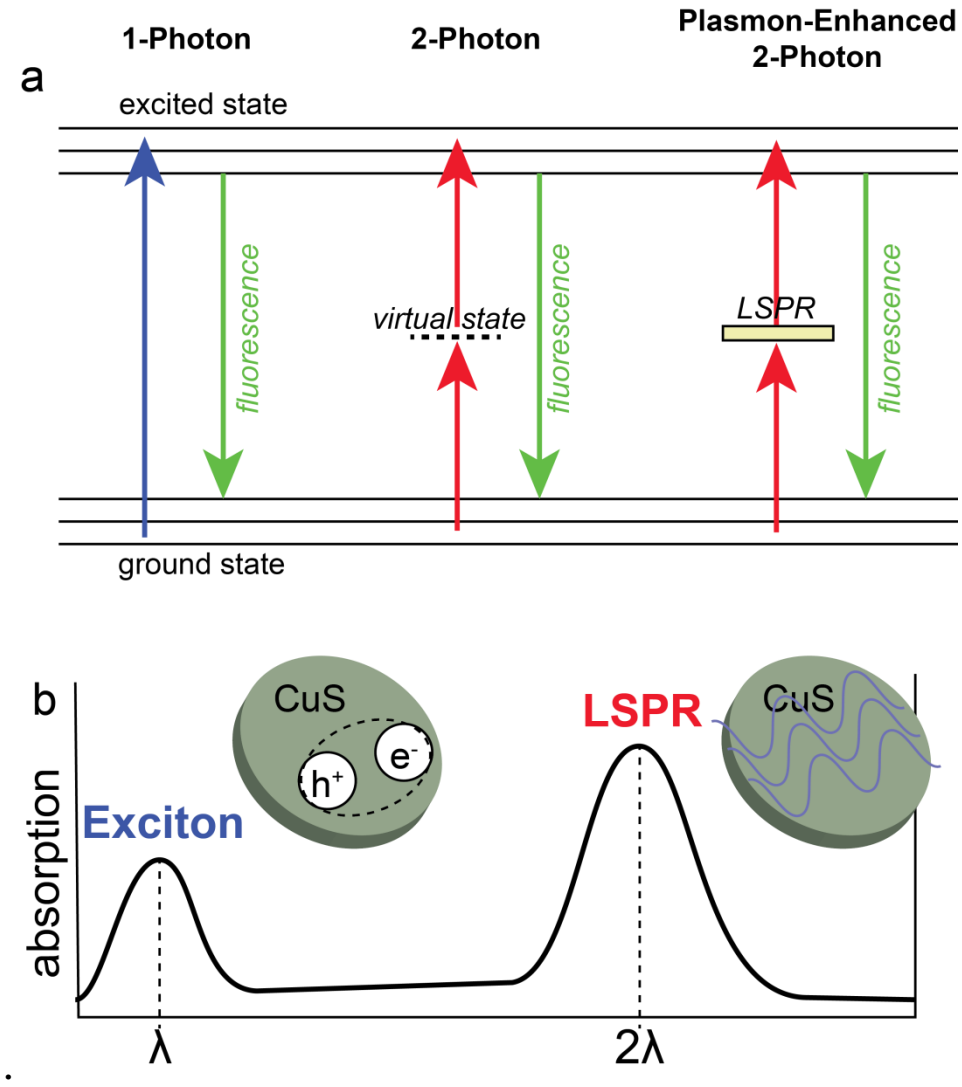

Figure 2.1. Schematic of photophysics in covellite nanoparticles. a) Schematic of the electronic transitions for 2PF. b) Schematic of the absorbance profile for plasmon-assisted 2PA.

2.2 Experimental Methods

2.2.1 Chemicals

1-octadecene ($C_{18}H_{36}$, 90%), oleylamine ($C_{18}H_{35}NH_2$, 70%), and sulfur powder (S, 98.98%) were purchased from Sigma Aldrich. Cupric nitrate hemi-pentahydrate ($Cu(NO_3)_2 \cdot 2.5\ H_2O$, 98%) and chloroform ($CHCl_3$, 99.25%) were purchased from Fisher

Chemical. Selenium powder (Se, 99.99%) was purchased from Alfa Aesar. All reagents were used as purchased.

2.2.2 CuS Nanodisk Synthesis

A solvent mixture of oleylamine and 1-octadecene was prepared in a 1:3 ratio, respectively. 0.0928 g of copper nitrate (0.4 mmol) was dissolved in 4 mL of solvent mixture by sonication, yielding a dark blue 0.1M Cu precursor solution. For CuS nanodisks, 0.0192g of sulfur powder (0.6 mmol) was added to the precursor solution. The mixture was then heated to 160 C in an oil bath for 30 minutes, forming a dark-green solution. To remove excess oleylamine and 1-octadecene, 4 mL of ethanol was added and the mixture was centrifuged at 3K RPM for 5 minutes. The precipitate was then removed, re-dispersed in chloroform and centrifuged at 7.5K RPM for 7.5 minutes to remove any by-products. This final centrifugation was repeated twice. The purified precipitate was then dispersed in 4 mL of chloroform for use and analysis. For Se-doped CuS nanodisks, a 0.6 mmol total mixture of Se:S powder was used in lieu of 0.0192 g of sulfur powder. The ratio of Se:S was varied to control the concentration of dopant in the final product.

2.2.3 Materials Characterization

Se:S content was determined using Energy Dispersive X-ray Spectroscopy (EDX). EDX spectra were obtained using a Philips XL30 ESEM with an Oxford EDX detector attachment coupled with Inca software. Samples were prepared by drop-casting onto a clean silicon support. The EDX detector was calibrated using the K_α peak of a Cu standard. Spot size, magnification, beam accelerating voltage, and process time were all kept constant to ensure accuracy in measurement. Relative errors in measurements are summarized in Appendix **Figure A4**. Powder X-ray Diffraction (XRD) spectra were

taken using a Rigaku RU200B diffractometer coupled with MDI Datascan5 software. A step size of 0.02° and a dwell time of 1.0 seconds was used at a 100 kV operating voltage. Samples were dried and deposited on a clean glass slide for measurement. An FEI Tecnai G2 Sphera running a LaB_6 filament at 200 kV was used for Transmission Electron Microscopy (TEM) micrographs. A Gatan Ultrascan 1000 UHS CCD camera running Gatan Digital Micrograph was used for imaging. TEM samples were prepared by drop-casting nanodisks dispersed in chloroform onto an air-water interface. 200 mesh carbon-film Cu grids were then dip-coated in the dispersion.

2.2.4 Optical Characterization

Optical extinction spectra were taken using a Perkin Elmer Lambda-1050 UV-vis-NIR spectrophotometer with a three-detectors (3D) module. The samples were dispersed in chloroform using a 1 cm quartz cuvette. Scans were performed from 250 nm to 2000 nm. Photoluminescence spectra were acquired using a Princeton Instruments Acton SP2300 monochromator coupled to a Nikon Eclipse LV100 upright microscope. A Kimmon Koha 20 mW 325 nm He-Cd laser was used as an excitation source. Samples were prepared by drop-casting onto a clean glass slide. For 2PE measurements, a Leica SP5 confocal microscope with a Leica HyD detector was used. This system was coupled to a Spectra Physics Mai Tai HP tunable laser. The excitation wavelength of the Mai Tai HP was varied from 690 nm to 1040 nm with an average power of 2.5 mW and pulsed at 100 fs through a 10x Leica objective. For sampling, a colloidal solution of nanodisks in chloroform was sealed in a glass chamber. For direct sample comparison, signal intensity was normalized for particle concentration which was determined using reported methods[27]. Chambers were sealed using 65 μL 15x15 mm frame seals by Bio-Rad. Mean

2PE emission intensity values for varied excitation wavelengths were determined by integrating the detector signal over a specified and fixed wavelength range. This collected range was 400-650 nm, which covers the range of the emission spectra for all samples and is described further in Appendix A (**Figure A1**). Molar absorptivity (α) values were calculated directly from particle concentration and absorbance. Laser power measurements were performed using an Ophir Vega Handheld Laser Power Meter.

2.3 Results and Discussion

CuS nanodisks were synthesized using solvent-based methods as described in the Experimental Section. An excess of sulfur powder was used to ensure the formation of the stoichiometric CuS (covellite) phase, as opposed to the $Cu_{7.2}S_4$ (digenite) phase which preferentially occurs at higher Cu:S ratios [26]. **Figure 2.2a** shows a TEM micrograph of a dispersion of un-doped (left) and Se-doped (right) CuS nanodisks using the solvent-based method, which yielded particles with an average diameter of 31.14 ± 7.45 nm with an aspect ratio of 4.54 ± 1.51. The diameters and aspect-ratio distributions of individual samples are fully listed in **Table A1**. The powder XRD spectrum of CuS nanodisks is shown in **Figure 2.2b**, highlighting the characteristic diffraction peaks of the covellite phase. CuS is a p-type semiconductor that exhibits semi-metal behavior [28]. Furthermore, it exhibits absorptive and emissive optical responses. **Figure 2.2c** plots an overlay of the photoluminescence emission (λ_{ex}=325 nm) and the extinction spectrum for a typical colloidal CuS nanodisk sample dispersed in chloroform. The extinction peak in the NIR is a maximum at λ_{LSPR}=1125 nm and is attributed to a strong in-plane dipole mode. The onset of the absorption edge can be observed at *ca.* 400 nm and is the result of excitonic

absorption due to quantum confinement and a direct band gap.[29] The Stokes-shifted photoluminescence emission maximum occurs at λ_F=505 nm. λ_{LSPR} in un-doped CuS nanodisks occurs at well over double the wavelength of the absorption edge, which enables 2PA.

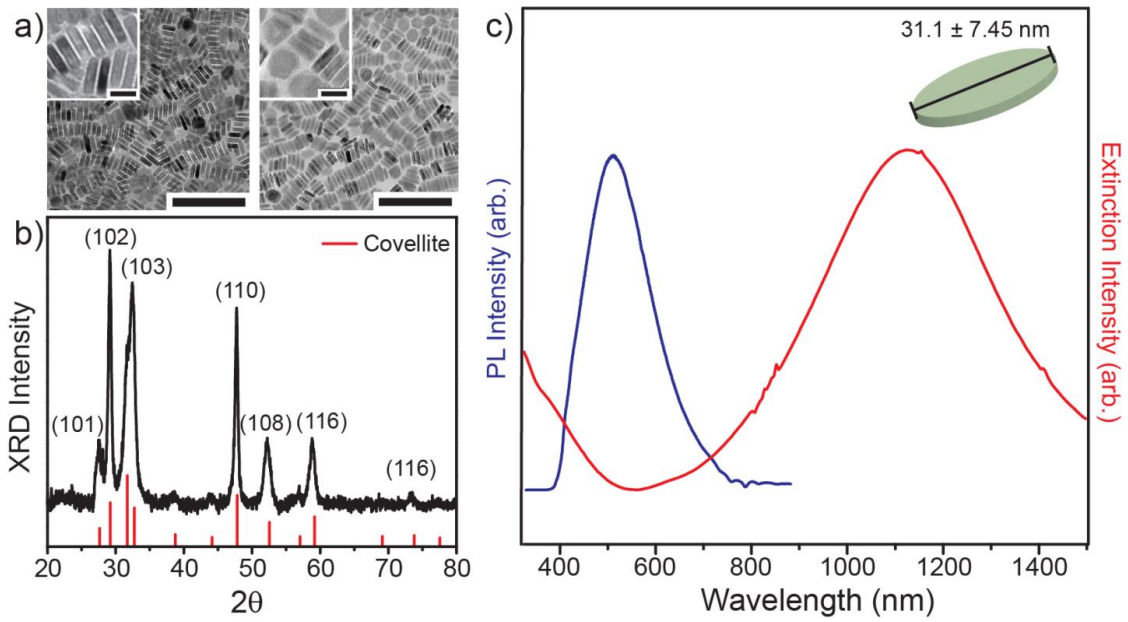

Figure 2.2. CuS optical properties. a) Typical TEM micrographs of CuS nanodisks (left) and Se-doped CuS nanodisks (right), scale bars are 150 nm. Insets are zoomed-in images, inset scale bars are 20 nm. b) Typical XRD spectra of CuS nanodisks with highlighted diffraction pattern. c) The photoluminescence emission spectra and extinction spectra for CuS.

To determine whether these CuS are capable of nonlinear absorption, we carried out 2PE measurements using femtosecond-pulsed laser excitation at λ_{ex}=855 nm. CuS nanodisk samples were prepared by drop-casting and drying the dispersion onto a clean glass slide. These samples exhibit a well-defined emission peak centered at *ca.* λ_F=500 nm (**Figure 2.3a**). The line shape and location of this peak is in close agreement with the single-photon fluorescence measurements in **Figure 2.2c**. In order to demonstrate that

this emission is the result of 2PA, we measured the fluorescence emission intensity with respect to the power of the excitation source. While single-photon absorption is expected to give a linear relationship, multi-photon absorption is expected to give rise to a non-linear relationship between emission intensity and source power. [30] For a perfect 2PA process, the emission intensity varies with the square of the source power. [31] **Figure 2.3b** shows a log-log plot of laser power versus emission intensity. Upon increasing and decreasing laser power we observed a slope of 1.87 and 2.37, respectively. This is in close agreement with the power-squared dependence (slope=2) characteristic of a 2PA process.

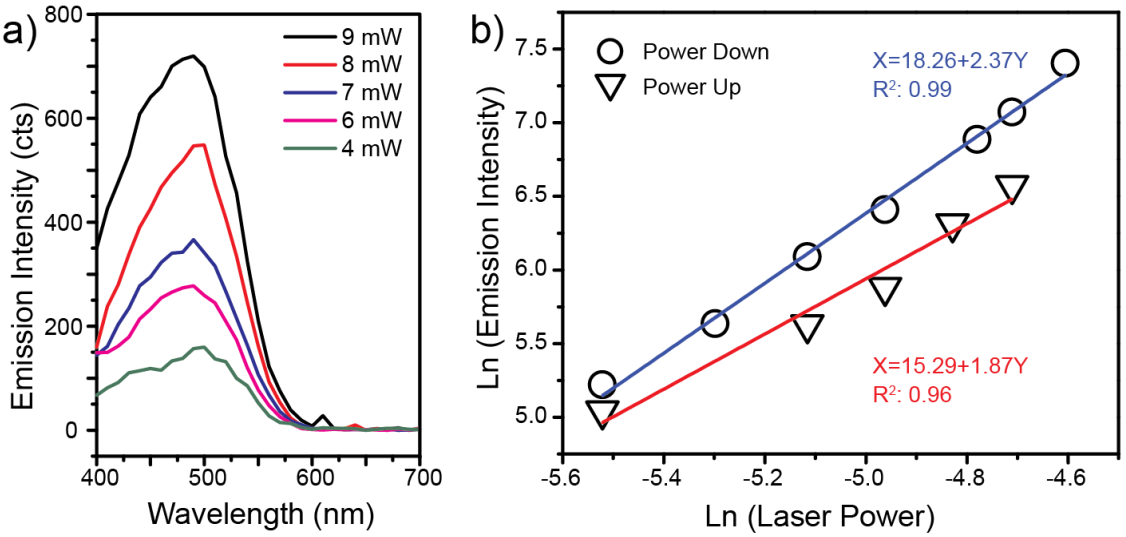

Figure 2.3. Nonlinear CuS emission. a) The 2PE spectra of CuS at various laser powers. b) A log-log plot shows the power-square dependence of emission. Laser power was incrementally increased (Power Up) and decreased (Power Down) to acquire two separate fits for comparison.

To study the effect of λ_{LSPR} on 2PE intensities, we modulated the wavelength of λ_{LSPR} by doping the CuS nanodisks with Se. Doping is achieved by direct substitution of S atoms within the covellite lattice with Se atoms. X-ray diffraction measurements show that the crystal structure remains constant and covellite-like, which suggests a 1:1 ratio of

Cu to total chalcogen (**Figure A3**). The extinction spectra for these samples is plotted in **Figure 2.4a** which shows a λ_{LSPR} value of 945 and 1150 nm for doped and un-doped samples, respectively. Our results show that the λ_{LSPR} of the in-plane dipole mode can be blue-shifted towards lower wavelengths with increasing Se content. The largest blue-shift in λ_{LSPR} that can be achieved gives λ_{LSPR}=945 nm for 2.6 atomic % Se by atomic weight. Increasing the amount of Se content beyond a few percent results in a red-shift in λ_{LSPR}, likely due to poor Se solubility in the CuS lattice (**Figure A2**).

We then determined whether Se doping results in a change in the 2PA wavelength. **Figure 2.4b** shows a plot of the mean 2PE emission intensity with respect to λ_{ex}, with a step size of 5 nm. As described in the Experimental Section, the mean intensity is the integrated emission signal over a specified wavelength range. This range is fixed for all samples from 400-650 nm. This was performed for two samples: (i) an un-doped CuS nanodisk dispersion, and (ii) a Se-doped CuS nanodisk dispersion with 2.6 atomic % Se, as measured by energy dispersive X-ray spectroscopy. The two samples show no difference in the λ_{ex} value that gives the maximum 2PE intensity, with λ_{ex}=855 nm for both the un-doped sample and Se-doped sample. This suggests that Se doping does not affect the absorption edge of the CuS nanodisks.

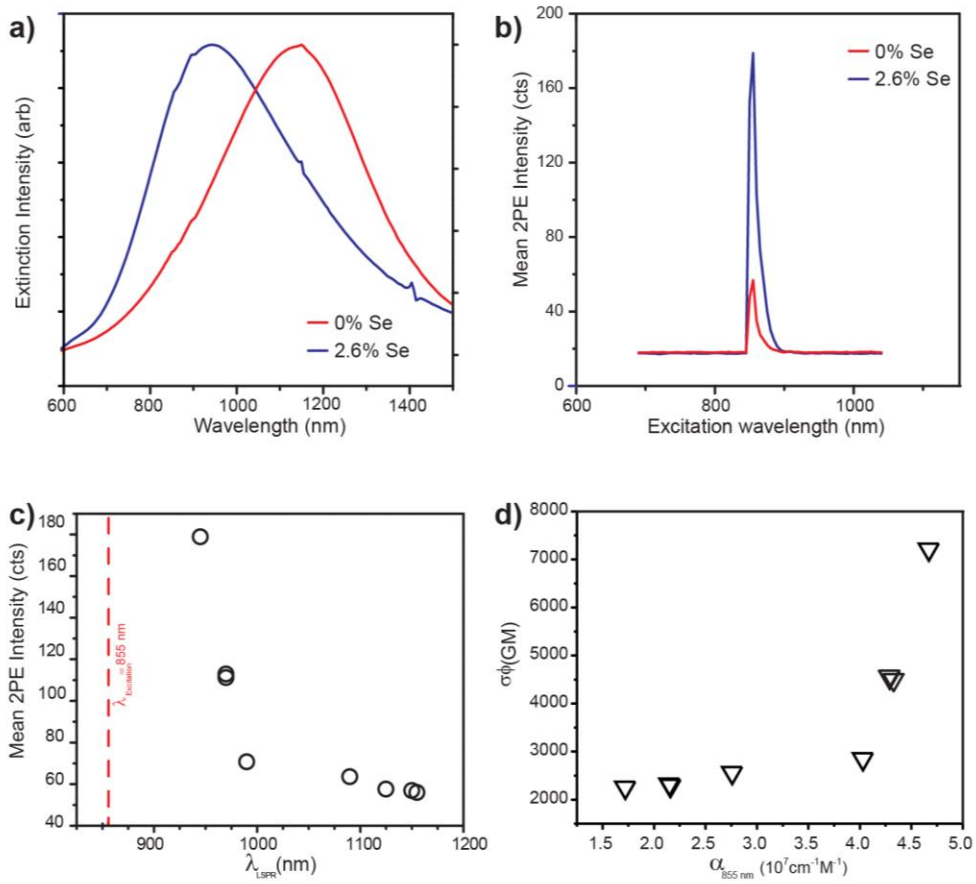

Figure 2.4. CuS 2PE dependence on plasmon resonance. a) Extinction spectra of 2.6% Se-doped CuS (blue) and un-doped CuS (red). b) Mean 2PE intensity as a function of excitation wavelength. c) Dependence of mean 2PE intensity on λ_{LSPR} location. d) Two-photon action cross-section as a function of CuS nanodisk molar absorptivity at the excitation wavelength.

Next, we measured the mean 2PE emission intensity as a function of λ_{LSPR} for eight different CuS nanodisk samples. These CuS nanodisks samples were synthesized with varying Se content and exhibit in-plane LSPR modes with λ_{LSPR} varying between 945-1155 nm. **Figure 2.4c** plots the mean 2PE intensity obtained for λ_{ex}=855 nm. As the value of λ_{LSPR} begins to approach the value of λ_{ex}, we see that the measured 2PE intensity experiences a dramatic increase. 2PE intensity is maximized as λ_{LSPR} approaches the two-photon absorption edge. This indicates that the increase in emission intensity occurs due

to an increase in absorbance, since field-enhancement of the fluorescence emission is not expected at these long wavelengths[32] (**Figure 2.4c**).

To gauge the effect of LSPR excitation on 2PE, we calculated the two-photon action cross-sections ($\sigma\phi$) for these CuS nanodisks. $\sigma\phi$ has been used extensively as an effective measure for the magnitude or brightness of two-photon induced fluorescence emission [33,34], and is the product of the absolute 2PA cross section (σ) and the fluorescence quantum efficiency (ϕ). We calculated $\sigma\phi$ using previously reported methods [34,35] and used Lucifer Yellow as a reference fluorophore. This method is described further in Appendix A (**Section A1**). For our samples, $\sigma\phi$ ranged from 2255.2-7211.5 Goeppert-Mayer (GM) units, depending on the value of λ_{LSPR} **(Table 2.1**). Our results show that higher $\sigma\phi$ values correlate with greater overlap between λ_{LSPR} and λ_{ex}. This range for $\sigma\phi$ is also on the order of previously reported values for solid-state luminescent materials such as CdSe quantum dots and gold nanorods,[1,36] and an order-of-magnitude above those reported for conventional molecular fluorophores such as Bodipy, DAPI, and Rhodamine B.[33]

Table 2.1. Two-photon action cross sections for various CuS samples.

Sample	λ_{LSPR} (nm)	$\sigma\phi$ (GM)
1	945	7211.5
2	970	4551.7
3	970	4481.5
4	990	2849.7
5	1090	2560.9
6	1125	2322.2
7	1150	2293.9
8	1155	2255.2

To indicate the relationship between LSPR excitation and 2PE brightness, we plotted $\sigma\phi$ as a function of CuS nanodisk molar absorptivity at 855 nm (α_{855}) (**Figure 2.4d**). We calculated α_{855} directly from the extinction spectra for various Se-doped CuS nanodisk samples, as described in the Experimental Section. We observe that $\sigma\phi$ is maximum for our highest obtained value of α_{855}. We also observe that the relationship between $\sigma\phi$ and α_{855} is highly nonlinear, and that a critical value of $\alpha_{855} = 4x10^{7}cm^{-1}M^{-1}$ must be reached before the 2PE brightness increases. These higher α_{855} values indicate stronger light absorption, which correlates well with higher 2PE brightness. This is additional evidence that plasmon-assisted absorption plays a role in enhanced absorption, rather than emission.

2.4 Conclusions

This work demonstrates the nonlinear optical properties of plasmonic covellite CuS nanodisks synthesized by colloidal methods. Furthermore, we probe the effect of LSPR excitation on 2PE by utilizing Se doping to tune the LSPR wavelength. While Se doping is unable to achieve full registry of the LSPR peak with the absorption edge of CuS, we observed a strong enhancement of 2PE emission for samples with higher spectral overlap. This 2PE response is unique in that the SNCs serve as both the plasmonic and photoluminescent components, offering an all-in-one platform for engineering plasmon-exciton coupling in the absence of a physicochemical interface. Furthermore, the 2PE action cross-sections indicate that these CuS nanomaterials show great potential for applications that require multi-photon absorbance, such as bioimaging and photodynamic therapy. Future studies will explore alternative dopant materials and SNC shapes that may offer greater flexibility with modulating the LSPR resonance wavelength to match the absorption edge of CuS.

Acknowledgments

This work is funded by a grant from the National Science Foundation (CHE, Award No. 1508755). The authors would like to thank the UCSD School of Medicine Microscopy Core for the use of their facility and acknowledge its supporting grant, NS047101. A.R.T. gratefully acknowledges financial support from the Arthur P. Sloan Foundation.

Chapter 2, in full, is a reprint of the material as it appears in *ACS Photonics*, 2016, 3 (4), 526- 531. The American Chemical Society, 2016. Brandon C. Marin,[†] Su-wen

Hsu,† Li Chen, Ashley Lo, Darwin W. Zwissler, Zhaowei Liu, and Andrea R. Tao. († Equal contribution). The dissertation author was the primary investigator and author of this paper.

References

(1) Larson, D. R.; Zipfel, W. R.; Williams, R. M.; Clark, S. W.; Bruchez, M. P.; Wise, F. W.; Webb, W. W. Water-Soluble Quantum Dots for Multiphoton Fluorescence Imaging in Vivo. *Science* 2003, *300*, 1434–1436.

(2) Michalet, X.; Pinaud, F. F.; Bentolila, L. A.; Tsay, J. M.; Doose, S.; Li, J. J.; Sundaresan, G.; Wu, A. M.; Gambhir, S. S.; Weiss, S. Quantum Dots for Live Cell, in Vivo Imaging and Diagnostics. *Science* 2005, *307*, 538–544.

(3) Gao, X.; Yang, L.; Petros, J. A.; Marshall, F. F.; Simons, J. W.; Nie, S. In Vivo Molecular and Cellular Imaging with Quantum Dots. *Curr. Opin. Biotechnol.* 2005, *16*, 63–72.

(4) Liu, Q.; Guo, B.; Rao, Z.; Zhang, B.; Gong, J. R. Strong Two-Photon-Induced Fluorescence from Photostable, Biocompatible Nitrogen-Doped Graphene Quantum Dots for Cellular and Deep-Tissue Imaging. *Nano Lett.* 2013, *13*, 2436–2441.

(5) Gao, D.; Agayan, R. R.; Xu, H.; Philbert, M. A.; Kopelman, R. Nanoparticles for Two-Photon Photodynamic Therapy in Living Cells. *Nano Lett.* 2006, *6*, 2383–2386.

(6) Resch-Genger, U.; Grabolle, M.; Cavaliere-Jaricot, S.; Nitschke, R.; Nann, T. Quantum Dots versus Organic Dyes as Fluorescent Labels. *Nat. Methods* 2008, *5*, 763–775.

(7) Wang, B.G.; Konig, K.; Halbhuber, K.J. Two-Photon Microscopy of Deep Intravital Tissues and Its Merits in Clinical Research. *J. Microsc.* 2010, *238* (1), 1–20.

(8) Pu, S.C.; Yang, M.J.; Hsu, C.C.; Lai, C.W.; Hsieh, C.C.; Lin, S. H.; Cheng, Y.M.; Chou, P.T. The Empirical Correlation Between Size and Two-Photon Absorption Cross Section of CdSe and CdTe Quantum Dots. *Small* 2006, *2*, 1308–1313.

(9) Padilha, L.; Fu, J.; Hagan, D.; Van Stryland, E.; Cesar, C.; Barbosa, L.; Cruz, C. Two-Photon Absorption in CdTe Quantum Dots. *Opt. Express* 2005, *13*, 6460–6467.

(10) Durr, N. J.; Larson, T.; Smith, D. K.; Korgel, B. A.; Ben-Yakar, A. Two-Photon Luminescence Imaging of Cancer Cells Using Molecularly Targeted Gold Nanorods. *Nano Lett.* 2009, *7*, 941–945.

(11) Wang, H.; Huff, T. B.; Zweifel, D. A; He, W.; Low, P. S.; Wei, A.; Cheng, J.X. In Vitro and in Vivo Two-Photon Luminescence Imaging of Single Gold Nanorods. *Proc. Natl. Acad. Sci.* 2005, *102*, 15752–15756.

(12) Park, J.; Estrada, A.; Sharp, K.; Sang, K.; Schwartz, J. A.; Smith, D. K.; Coleman, C.; Payne, J. D.; Korgel, B. A.; Dunn, A. K.; Tunnell, J. W. Imaging of Tumors Using Near-Infrared Excited Gold Nanoshells. *Opt. Express.* 2008, *16*, 214–221.

(13) Yuan, H.; Khoury, C. G.; Hwang, H.; Wilson, C. M.; Grant, G. A.; Vo-Dinh, T. Gold Nanostars: Surfactant-Free Synthesis, 3D Modelling, and Two-Photon Photoluminescence Imaging. *Nanotechnology* 2012, *23*, 075102.

(14) Medintz, I. L.; Uyeda, H. T.; Goldman, E. R.; Mattoussi, H. Quantum Dot Bioconjugates for Imaging, Labelling and Sensing. *Nat. Mater.* 2005, *4*, 435–446.

(15) Hwang, S.-Y.; Tao, A. R. Biofunctionalization of Gold Nanorods. *Pure Appl. Chem.* 2010, *83*, 233–241.

(16) Ueno, K.; Juodkazis, S.; Shibuya, T.; Yokota, Y.; Mizeikis, V.; Sasaki, K.; Misawa, H. Nanoparticle Plasmon-Assisted Two-Photon Polymerization Induced by Incoherent Excitation Source. *J. Am. Chem. Soc.* 2008, *130*, 6928–6929.

(17) Alkilany, A. M.; Thompson, L. B.; Boulos, S. P.; Sisco, P. N.; Murphy, C. J. Gold Nanorods: Their Potential for Photothermal Therapeutics and Drug Delivery, Tempered by the Complexity of Their Biological Interactions. *Adv. Drug Deliv. Rev.* 2012, *64*, 190–199.

(18) Bouhelier, A.; Bachelot, R.; Lerondel, G.; Kostcheev, S.; Royer, P.; Wiederrecht, G. P. Surface Plasmon Characteristics of Tunable Photoluminescence in Single Gold Nanorods. *Phys. Rev. Lett.* 2005, *95* (26), 267405.

(19) Kano, H.; Kawata, S. Two-Photon-Excited Fluorescence Enhanced by a Surface Plasmon. *Opt. Lett.* 1996, *21*, 1848–1850.

(20) Lakowicz, J. R. Plasmonics in Biology and Plasmon-Controlled Fluorescence. *Plasmonics* 2006, *1*, 5–33.

(21) Zhao, T.; Wu, H.; Yao, S. Q.; Xu, Q.-H.; Xu, G. Q. Nanocomposites Containing Gold Nanorods and Porphyrin-Doped Mesoporous Silica with Dual Capability of Two-Photon Imaging and Photosensitization. *Langmuir* 2010, *26*, 14937–14942.

(22) Luther, J. M.; Jain, P. K.; Ewers, T.; Alivisatos, A. P. Localized Surface Plasmon Resonances Arising from Free Carriers in Doped Quantum Dots. *Nat. Mater.* 2011, *10*, 361–366.

(23) Zhao, Y.; Pan, H.; Lou, Y.; Qiu, X.; Zhu, J.; Burda, C. Plasmonic Cu 2-xS Nanocrystals: Optical and Structural Properties of Copper-Deficient Copper (I) Sulfides. *J. Am. Chem. Soc.* 2009, *131*, 4253–4261.

(24) Hsu, S.W.; On, K.; Tao, A. R. Localized Surface Plasmon Resonances of Anisotropic Semiconductor Nanocrystals. *J. Am. Chem. Soc.* 2011, *133*, 19072–19075.

(25) Hsu, S.-W.; Bryks, W.; Tao, A. R. Effects of Carrier Density and Shape on the Localized Surface Plasmon Resonances of $Cu_{2-x}S$ Nanodisks. *Chem. Mater.* 2012, *24*, 3765–3771.

(26) Hsu, S. W.; Ngo, C.; Tao, A. R. Tunable and Directional Plasmonic Coupling within Semiconductor Nanodisk Assemblies. *Nano Lett.* 2014, *14*, 2372–2380.

(27) Ku, G.; Zhou, M.; Song, S.; Huang, Q.; Hazle, J.; Li, C. Copper Sulfide Nanoparticles as a New Class of Photoacoustic Contrast Agent for Deep Tissue Imaging at 1064 nm. *ACS Nano.* 2013, *6*, 7489–7496.

(28) Liang, W.; Whangbo, M.H. Conductivity Anisotropy and Structural Phase Transition in Covellite CuS. *Solid State Commun.* 1993, *85*, 405–408.

(29) Grozdanov, I.; Najdoski, M. Optical and Electrical Properties of Copper Sulfide Films of Variable Composition. *J. Solid State Chem.* 1995, *114*, 469–475.

(30) Wu, C.; Szymanski, C.; Cain, Z.; McNeill, J. Conjugated Polymer Dots for Multiphoton Fluorescence Imaging. *J. Am. Chem. Soc.* 2007, *129*, 12904–12905.

(31) Denk, W.; Strickler, J. H.; Webb, W. W. Two-Photon Laser Scanning Fluorescence Microscopy. *Science* 1990, *248*, 73–76.

(32) Wang, Y.L.; Mohammadi Estakhri, N.; Johnson, A.; Li, H.Y.; Xu, L.X.; Zhang, Z.; Alù, A.; Wang, Q.Q.; Shih, C.K. Tailoring Plasmonic Enhanced Upconversion in Single NaYF4:Yb3+/Er3+ Nanocrystals. *Sci. Rep.* 2015, *5*, 10196.

(33) Xu, C.; Webb, W. W. Measurement of Two-Photon Excitation Cross Sections of Molecular Fluorophores with Data from 690 to 1050 nm. *J. Opt. Soc. Am. B.* 1996, *13*, 481.

(34) Albota, M. A.; Xu, C.; Webb, W. W. Two-Photon Fluorescence Excitation Cross Sections of Biomolecular Probes from 690 to 960 nm. *Appl. Opt.* 1998, *37*, 7352–7356.

(35) Wang, X.; Tian, X.; Zhang, Q.; Sun, P.; Wu, J.; Zhou, H.; Jin, B.; Yang, J.; Zhang, S.; Wang, C.; Tao, X.; Jiang, M.; Tian, Y. Assembly, Two-Photon Absorption, and Bioimaging of Living Cells of a Cuprous Cluster. *Chem. Mater.* 2012, *24*, 954–961.

(36) Wang, T.; Halaney, D.; Ho, D.; Feldman, M. D.; Milner, T. E. Two-Photon Luminescence Properties of Gold Nanorods. *Biomed. Opt. Express.* 2013, *4*, 584–595.

Chapter 3

Surface-Enhanced Raman Scattering (SERS) – Based Biosensing using Scalable and Templated Fabrication of Gold Nanobulbs

Brandon C. Marin, [†a] Sameer S. Walavalkar, [†b], Chieh-Feng Chang, [†b]Andrea R. Tao,[a]

Axel Shearer,[c] and Scott Fraser[b]

([†] Equal contribution)

[a]*NanoEngineering Department, University of California, San Diego. 9500 Gilman Drive MC 0448, La Jolla, CA 92093-0448*

[b] *University of Southern California, Translational Imaging Center, 401 Irani Hall (RRI),1050 Childs Way, Los Angeles, CA 90089*

[c] *California Institute of Technology, Applied Physics Dept. MC 200-36, Pasadena, CA 91126*

Abstract

This article features a new, scalable fabrication method and experimental characterization of arrays of gold “nanobulbs” for surface enhanced Raman spectroscopy. These structures are fabricated using a “hybrid” top-down/bottom-up approach which retains the uniformity and placement accuracy of lithographic methods while simultaneously exploiting bottom-up energy minimization techniques to obtain enhancement gaps as small as 5nm. Rather than attempting to shape the chemically inert gold directly, silicon nanofabrication techniques are used to create a glass super-structure around which the gold is sculpted in a high-temperature reflow step. As the initial conditions of the reflow are set by top-down parameters, the resulting structures are uniform across extended arrays and from chip to chip. Using thiophenol as a probe molecule these nanobulb substrates featured average enhancement factors in excess of 10^{10} across 19 peaks spanning a wide range of wavenumbers and symmetries. This enhancement factor, as well as spectral properties such as line-width and peak position, were shown to be uniform over extended arrays of nanobulbs with measured variations of less than 10%, 2.5% and 0.01%, respectively. The structures were subsequently used to detect nanomolar concentrations of tracheal cytotoxin, a 1kDa product of certain gram negative bacteria. The detection as well as the structural and conformational analyses were performed under both wet and dry conditions, without the use of specific probes or labels. Based on the scalability as well as the degree and uniformity of Raman enhancement, these manufacturable nanobulb substrates offer a variety of novel future biomedical applications, from binding chemistry analysis to ultra-sensitive disease-marker detection.

3.1 Introduction

Plasmonics has been a field of ardent work for the past decade, greatly aided by the development of various nanofabrication techniques that can create architectures several times smaller than the wavelength of light. Thus, there has been a great deal of work on plasmonic phenomena such as extraordinary transmission through sub-wavelength holes,[1,2,3,] optical filters,[4] epsilon-near-zero metamaterials,[5] broadband visible to NIR absorbers,[6] and enhanced emissive processes.[7] Surface-enhanced Raman spectroscopy (SERS) has been one such area of work with compelling results. Fundamentally, Raman spectroscopy aims to obtain the vibrational spectrum of a molecule through the analysis of photons that have been inelastically scattered by its normal vibrational modes. Unfortunately, this Raman scattering process is an incredibly weak effect, forcing practical applications of this technique to rely on powerful lasers, and limiting their utility to identifying bulk samples.[8] SERS attempts to overcome this limitation by harnessing the ability of metallic nanostructures to confine light in sub-wavelength volumes, enhancing the photon induced local electric field, and amplifying the efficiency of Raman scattering by several orders of magnitude. The incorporation of such "Raman-enhancing" substrates has pushed the relevant range of Raman techniques from bulk to trace molecular analyses,[9] with several groups reporting measurements with single molecule sensitivity.[10,11]

Traditional SERS substrate fabrication relies on various stochastic techniques to create sub-20 nanometer E-field enhancing gaps between colloidal Ag or Au particles,[12]

an approach which has been hindered by difficulties in reproducibility.[13,14,15,16,17] In the past decade, however, there have been significant improvements made to such "bottom-up" methods using surface functionalization on spheres or cubes to induce the formation of ordered arrays of nanoparticles with prescribed gap distances.[18,19] Unfortunately, this surface functionalization must be removed to permit the analyte of interest to enter the regions of field-enhancement. This limits potential analytes to those with a stronger binding affinity to gold and silver, such that they can displace the original functionalization; alternatively, one must find a chemical or physical etching method to remove the functionalization without damaging the particles or their spacing.

SERS substrate fabrication has been tied to such bottom-up methods due to the lack of a gas or plasma phase etchant for gold and silver. This has precluded the direct nanomachining of these metals at the critical 5-25nm length scale required to create SERS nano-gaps. Consequently, there have been a limited number of "top-down" approaches to fabricating SERS substrates, with few notable exceptions.[20] Groups have used top-down techniques such as "lift-off," micro-masked etching, or electromigration to form both controlled[21,22] and stochastic nano-architectures.[9,23] These methods have demonstrated high enhancement factors (EF) and functional utility for biosensing applications.[24]

While the bottom-up approaches to SERS substrate fabrication can access the smallest size regimes, when used alone they offer limited scalability potential. However, if such an approach could be integrated around a top-down method, the combined scheme could provide the necessary precision to reliably and repeatedly fabricate substrates with sub-20 nm enhancement gaps. Such a combined process would be a crucial step towards

manufacturing SERS-based sensors for medical applications that require consistent and reproducible performance in sensitivity, specificity and accuracy.

3.2 Methods

3.2.1 Nanobulb Fabrication

Detailed steps given in **Appendix B1**. Using PMMA as an electron-beam resist a square lattice of circular areas corresponding to the SiNP diameters were exposed and developed away. Stoichiometric aluminum oxide (Al2O3) was reactively sputtered into these holes and lift-off was performed in dichloromethane under sonication. These alumina disks were etched vertically to a depth of 750 nm to form nanopillars (**Figure 3.1(a.i)**) using a mixed-mode ``pseudo-Bosch'' etch[1] and fully oxidized during an 8 hour dry oxidation (**Figure 3.1(a.ii)**). These glass nanopillars were conformally coated with 200 nm of sputtered gold (**Figure 3.1(a.iii),(b)**). In the final step the gold layer was reflowed in a rapid thermal annealer (RTA) in which the temperature was ramped to the peak in 30 seconds, held for 7 minutes and cooled to room temperature in 5 minutes, all in a forming gas (5%H2:95%N2) environment.

3.2.2 Materials

Tracheal cytotoxin (TCT) was obtained from the Goldman lab at the University of North Carolina, Chapel Hill. Extraction and purification of TCT follows the method outlined in Cookson et. al. [2] and is briefly outlined below. *Bordetella Pertussis* bacteria were grown on a solid growth medium for 72 hours at 37 ^{o}C and subsequently used to inoculate a liquid growth medium and allowed to incubate for an additional 24 to 48 hours at 37 ^{o}C. Bacteria from mid to late-log phase of growth were centrifuged and the supernatant was filtered through a 0.2 μm pore-size cellulose-acetate filter and acidified

using trifluoroacetic acid. TCT was separated using a column extraction method [2–4] and characterized using reverse-phase high-pressure liquid chromatography (HPLC).

3.2.3 Simulations

Electric field profiles were simulated with the finite-difference time-domain (FDTD) method, using the freely available MEEP[5] software package. Parameters for the simulations were extracted from SEM images of specific tested substrates. The frequency dependent permittivity of gold was modeled using a Lorentz-Drude model[6] tailored for accuracy in the 1.24-2.48 eV (500 - 1000 nm) range. The use of the simulated field profiles in calculating the reported enhancement factors is described in detail in **Appendix B.2.2**.

3.2.4 Instrumentation

Raman measurements were performed using a Renishaw "inVia" micro-Raman spectrometer coupled to a Leica Microscope. Illumination was provided by a filtered 17mW, CW HeNe laser at 633 nm (FWHM < 1 nm) at 0.01-0.5% laser power, set via internal neutral density filters. Imaging, excitation and collection were done through a 50x objective lens (Leica N-plan), and the collected signal was passed through an edge filter and dispersed onto a spectrometer with a Peltier-cooled (-70 ^{o}C) CCD detector using an 1800 line/mm grating, providing a spectral resolution of 1.2 cm^{-1}. For these measurements, signal was collected between 100 and 3200 cm^{-1} for 10 seconds. Bulk Raman spectra were collected from 65µL of neat thiophenol in a Bio-Rad incubation chamber sealed with a glass cover slip (15x15x0.29 mm), illuminated with 5% laser power using the same objective lens, spectral range, and 10 second acquisition time.

Mapping scans were performed using the same Renishaw in-Via micro-Raman spectrometer. Maps was taken with a step size of approximately 750 nm in both the x and y direction. At each point the SERS spectrum was collected between 600 and 1735 cm^{-1} wavenumbers for 0.5s at 1% laser power, producing a total of 7856 distinct spectra. For each spectrum, a Voight lineshape was fit to the peaks under consideration to account for both homogenous and inhomogenous broadening. The reported overlay images were produced using the Renishaw Wire 4 software package and the data was exported with subsequent statistical analysis performed in Matlab.

3.3 Results and Discussion

Here, we describe the fabrication, characterization and use of a novel SERS substrate created using scalable techniques and featuring unique properties suited for biomedical applications. We present a “hybrid” top-down/bottom-up fabrication method that uses the precision placement of CMOS lithography to create a periodic array of glass nanostructures around which gold spheres are assembled using surface forces to create an array of sub-20 nm periodic, field-enhancing gaps. We characterized the enhancement factor and spectral properties of these “nanobulb” substrates across a broad (>3000 cm-1) wavenumber range, several molecular symmetries, and over extended arrays and found the average enhancement to be greater than 1010 with a coefficient of variation < 10%. We also report the use of these substrates for the label-free detection and detailed study of tracheal-cytotoxin (TCT) and ss-DNA, which are complex bio-molecules.

The SERS substrates in this work were fabricated from bulk silicon wafers onto which silicon nanopillars (SiNP) were patterned and etched using previously published

methods[7,1,8]. To rapidly modify and test new designs, we performed our fabrication with electron beam lithography. However, with the adoption of nano-imprint or modern immersion lithography this fabrication procedure can be immediately translated to wafer-scale production. Crucially, all of these top-down, nano-machining steps are performed on or to silicon rather than directly with glass or gold. Fabrication details are provided in **Appendix B1** and briefly described in the methods section.

This reflow process represents the critical bottom-up step in our fabrication scheme wherein the elevated temperature allows the surface tension forces of the gold to overcome its weak adhesion to glass and flow towards a minimum energy shape- a sphere. We note that there are two distinct regions: For the planar field of glass the gold remains in place, while the gold coating the pillar side-walls and top flows to form a roughly spherical shape atop the pillars to minimize its surface area and maximize its contact angle with the glass(as seen in **Figure 3.1((c)-(e)**). [9,10,11] It is the resulting gaps (highlighted in panel **Figure 3.1 (e)**) between the beads of gold in this periodic lattice of nanobulbs that we exploit for our SERS enhancement. Note that the use of electrically insulating silicon dioxide pillars allows the reflow process, when carried to completion by a sufficiently high temperature, to break any current path between the bulb and planar metal allowing for the maximum field enhancement between each bulb and its nearest neighbors. Such high-temperature processing of gold films has been shown to provide added benefit of improving the crystallinity and conductivity of the beads[12] and planarizing the metal through Ostwald 'ripening'[7,12]. During fabrication development, we investigated the parameter space of pillars with diameters between 40 to 125 nm, lattice spacing of 300 to 700 nm, and reflow temperature from 625 to 725 °C. We found

675 °C to be the optimal reflow temperature and an optimal region of parameter space for pillar diameters and lattice spacing from 40 to 60 nm and 300 to 500 nm respectively.

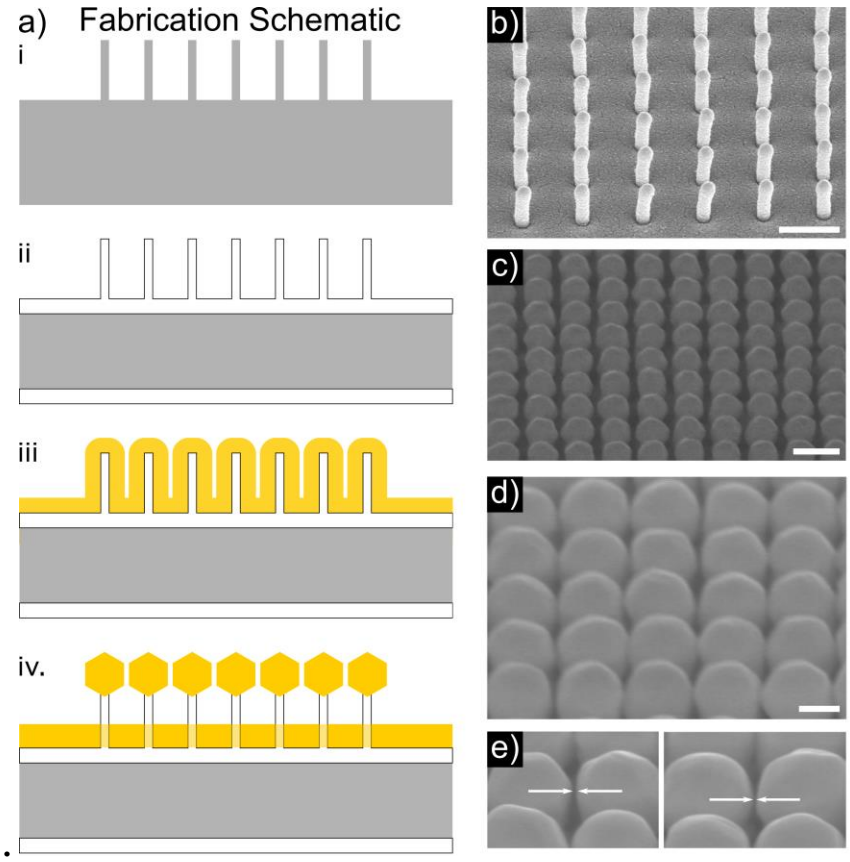

Figure 3.1. Fabrication and reflow of SERS substrates. (a) Fabrication flow: (i) Silicon nanopillars are patterned and plasma etched.(ii) Pillars are thermally oxidized to create silicon dioxide nanopillars. (iii) Sputtering of gold provides conformal coating of the glass pillars. (iv) Gold reflow causes the gold on the side-walls to bead on top of the pillars creating nanoscale gaps. (b) Sputtered gold on glass pillars prior to reflow. Scale bar 500nm (c) Example of gold nanobulbs with 25nm gaps. Scale bar is 300nm. (d) Nanobulbs with sub-10nm gaps. Scale bar is 200nm. (e) Two detailed frames of approximately 10 (left) and 5 (right) nm gaps.

The power of this fabrication method comes from its repeatability and scalability. Every fabrication parameter (e.g. pillar diameter, metal thickness, pillar spacing, etc.) leading up to the reflow step is controlled solely through top-down processing. Given that

we can precisely set the initial conditions and the reflow parameters we can create vast arrays of nanobulbs with nanometer-scale gaps that, as we show below, produce consistent enhancement factors. The gold/glass material system has the added benefit of being chemically inert, especially with respect to biological samples, easily functionalized and can be cleaned and re-used by utilizing an oxygen plasma or an oxidizing acid.

3.3.1 Quantification of SERS Activity in Nanobulbs

We characterized the magnitude and spectral properties of the Raman enhancement provided by the nanobulb substrates using thiophenol ($HS\text{-}C_6H_5$) as our molecular probe. For these measurements, substrates were first cleaned in an oxygen plasma for 5 minutes and immediately immersed in a 1 mM solution of thiophenol in ethanol and allowed to incubate for 6 hours. Upon removal, substrates were thoroughly rinsed with ethanol and deionized water and dried under N_2. Raman measurements were performed as described under the instrumentation heading in the methods section below.

Figure 3.2(a) presents the normalized signal (blue) measured at a single point close to the center of the array of nanobulbs shown in the SEM images of **Figure 3.1(d,e)** and in the microscope image of **Figure 3.3**. Parameters extracted from SEM image analysis were used to create an idealized finite difference time domain (FDTD) simulation of this bulb array at the illumination wavelength as well as at several Stokes photon wavelengths, an example of which is shown in **Figure 3.2(b)**. Using the SERS spectra, bulk Raman spectra and the FDTD simulations we calculated four different enhancement factors at 19 peaks shared between the SERS and bulk spectra. Specifically, at each peak, we calculated the analytic enhancement factor (AEF) and SERS substrate

enhancement factor (SSEF) based on either the maximum peak intensity or the total area of the peak- the goal of which was to be as thorough as possible with quantifying the SERS activity of our substrates. Our calculation methodology followed procedures outlined in Le Ru et. al.[13] A detailed explanation as well as the complete set of calculated enhancement factors is given in **Appendix B.2**.

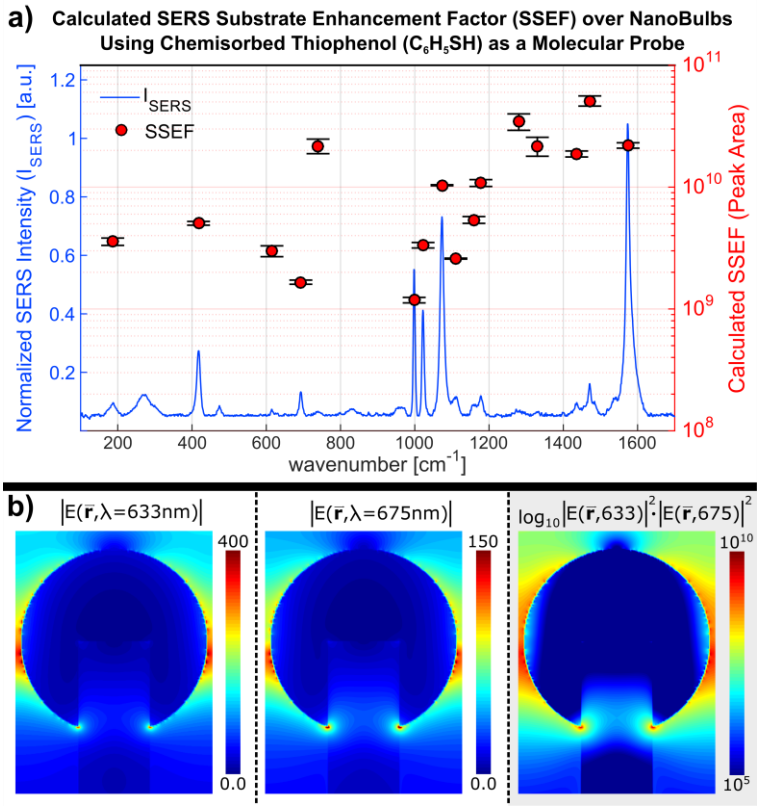

Figure 3.2. Measurement of thiophenol for enhancement factor calculations. (a) SERS signal at a single point on pillar array below (blue) and calculated SSEF at the peak locations shown (red). Note error bars indicate the uncertainty the calculation of the area under the peak. (b) FDTD simulation of local field enhancement at the 633 nm excitation, 675 nm emission, and the log of the total intensity enhancement from a point by point convolution of the above two plots.

The 19 shared peaks span an approximately 3000cm^{-1} range and correspond to vibrational modes from four unique benzene symmetry groups. Establishing the performance of the substrates over a large spectral range and under both optimal and non-

optimal alignment of the enhanced field with molecular symmetry is intended to produce a more representative set of enhancement factors. The SSEF values calculated based on area of the peak ($SSEF_{PK\ AREA}$) are plotted as red circles for the 16 shared peaks seen in the wavenumber range of **Figure 3.2(a)** with the error bars representing the uncertainty in the calculated area under the peak. When averaged over the entire set of peaks/symmetries we find a mean $SSEF_{PK\ AREA}$ of $1.3x10^{10}$ measured close to the center of the nanobulb array. The FDTD simulation results indicate that the large magnitude of this average enhancement factor stems from the local amplification of the electric field between adjacent nanobulbs. Previous theoretical studies[14–16] into the origin of this field enhancement for particles with sizes much larger than the Rayleigh limit suggest the importance of multi-polar terms, increased near-field scattering and resonance based minima in radiation damping. In compliment to the experimental results and specific simulations presented in this paper detailed FDTD and Mie-theory based analysis of the nanobulb substrates is underway.

We then expanded our investigation to determine the enhancement factor uniformity and variation in spectral properties of the SERS signal across an entire periodic array of nanobulbs. This was done by performing a 2D mapping scan over a 66.5 micron by 66.5 micron area which included a 40 micron by 40 micron square lattice of nanobulbs. Details of the mapping scan parameters are given under the instrumentation heading in the methods section below. As a representative example, **Figure 3.3** shows the 2D map (750 nm x 750 nm pixel size) and frequency histogram of the SSEF, linewidth and peak position of the $1073cm^{-1}$ mode. We can see from the maps and histogram data that the measured enhancement factor for this mode consistently fell into a narrow range

over the entire nanobulb area. Similarly, the measured linewidth and position of this mode showed little variation over the same map. We have compiled the average SSEF, linewidth and peak position for five frequently compared modes (700, 1000, 1023, 1073, 1574 cm^{-1}) into the table at the bottom of **Figure 3.3**. Our measured average linewidths over the entire nanobulb array are comparable to previously published data[17] and we additionally report a variation in SSEF of less than 10%, in linewidth of less than 2.5%, and in peak position of less than 0.01%. We attribute this uniformity to use of precision top-down lithography as well as the periodic nature of our arrays. Since the lattice exhibits periodicity in polarization direction of the incident optical field it is likely that we are exciting an extended mode across several bulbs. This effect, combined with the increased polarizability afforded by larger diameter spheres, explains the wide nanobulb array fabrication parameter space over which we recorded similar enhancement performance. As a result, the inter-particle gap seems to play a less critical role in our arrays than its influence on the enhancement properties of nanoparticle dimers. The uniformity in SERS of our nanobulb arrays permits such mapping scans to be used for not only detection but also the quantification of wide-ranging concentrations of biomolecules.

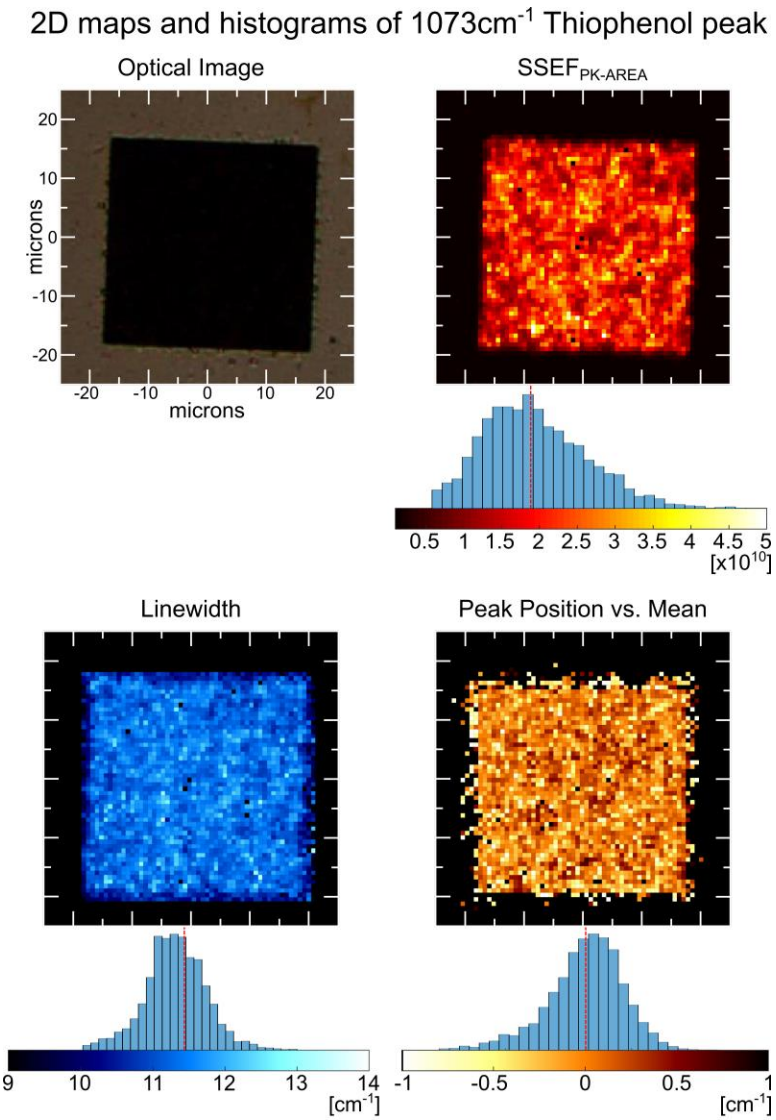

Mode [cm^{-1}]	SSEF [$x10^{10}$]	Γ_o [cm^{-1}]	ν_o [cm^{-1}]
700	0.264±0.022	9.11±0.145	694.0±0.056
1000	0.177±0.014	6.04±0.075	998.6±0.024
1023	0.476±0.042	7.73±0.085	1022.9±0.033
1073	1.911±0.155	11.42±0.127	1073.6±0.085
1574	1.491±0.128	9.28±0.215	1573.4±0.095

Figure 3.3. Mapping scans of 1073 cm-1 thiophenol mode over an array of nanobulbs. Scan step size was 750nm. Bottom table shows summary of mapping scan results for SSEF, linewidth and peak position for five frequently compared modes of thiophenol.

3.3.2 SERS analysis of a complex bioanalyte: tracheal cytotoxin

Unlike simple molecules such as the thiophenol studied above, biological molecules tend to be more complex and can form intricate secondary, tertiary, and quaternary structures. Fortunately, the uniformity and magnitude of nanobulb mediated enhancement allows for the resolution of detailed spectral features through rapid acquisitions. These substrates can therefore be used to not only detect complex biomolecules but probe their structure and conformation as well. To demonstrate this capability, we detected and analyzed the structure of tracheal cytotoxin (TCT) under two disparate environmental conditions. TCT is an approximately 1kDa glycopeptide released by some gram negative bacteria.[18] It is made up of a β (1-4') disaccharide head and a dipeptide tail. In its polymeric form, it is a constituent of the cell wall of gram-negative bacteria[3]. In this form, Raman spectra of TCT have been obtained through SERS measurements done on bacteria coated with colloidal silver.[19] In its monomeric form, TCT can serve as the agent of epithelial cell destruction in *B. pertussis* and *N. gonorrhoeae* infections[3,20] or as an important cellular messenger in the symbiotic interaction between the *V. fischeri* bacteria and its Bobtail Squid host.[18,20] TCT is not typically found in its monomeric form in the human body, unless there is an active infection involving the above mentioned bacteria. Thus the detection of trace amounts of TCT in patient samples collected via a variety of possible methods (e.g. throat swab, urine or saliva sample, etc.) is of paramount interest. As a first step in responding to this need we used the nanobulb substrates to detect and analyze TCT at nanomolar concentrations under two possible sample conditions: in a saliva or “serum-like” buffer, and dried as if taken from a swab. This represents the first Raman detection of free

monomeric TCT, and can serve as an initial step towards creating a "culture-free" test for Gonorrhea or Whooping Cough.

In the first scheme, the TCT was simply dried onto the substrate without targeted functionalization or binding. Samples were prepared by drying a 2µL droplet of 100nM TCT solution in buffer directly onto the nanobulbs. The collected spectrum is shown as the red curve in **Figure 3.4.** In the second scheme the 100nM TCT was measured while still in solution, relying on polar components such as deprotonated carboxylate ions to form coordinated complexes with the gold to enrich the concentration of molecule at the bulbs. This spectrum is shown as the blue curve in **Figure 3.4** (For comparison, both spectra are normalized by the magnitude of their respective anti-symmetric glycosidic bond stretching mode (label G)). As can be seen from both curves in **Figure 3.4,** the complexity of the molecule and the spectral resolution provided by the nanobulbs results in a densely populated Raman spectrum. We can roughly subdivide the spectra into three regions, Region 1 (100-800 cm^{-1}) contains the 3 "heavy-atom" bending modes and torsional modes[21–25]. Region 2 (800-1800 cm^{-1}) contains endo- and exocyclic single bond stretching modes that provide information about size of heteroatom rings and alpha/beta character of glycosidic linkages.[21–23,25–27] This region also contains peaks corresponding to the amide vibrations of peptide linkages and modes associated with carboxylic acid groups, both of which can provide information on the type and location of amino acids within the molecule. [21,22,24,27–31] This second section is significantly altered between the dry and wet ambient conditions and is the focus of **Figure 3.5**. Region 3 (1800-3200 cm^{-1}) contains sum-tone modes and heavy-light atom vibrational modes such as C-H or O-H bonds. In **Figure 3.4** we have highlighted some of the key peaks from regions 1 and 2

that can be used to identify this molecule (an exhaustive list of identified peaks for both the wet and dry cases is given in **Appendix B.3**). Specifically, in the 100-250 cm^{-1} range we have peaks associated with torsional and bending modes of the N-acetyl groups found in disaccharide head of TCT. The width of the mixed bending/torsion mode centered near 250 cm^{-1} can be ascribed to separated but overlapping signals from the two similar N-acetyl groups found on the glucosamine and muramyl sugars, split by local sterics or intramolecular hydrogen bonding. At 500 cm^{-1} we can see a broad peak associated with the three atom COC bending of the β(1-4') glycoside link which narrows and brightens based on the hydrogen bonding in the wet spectrum. A similar narrowing and brightening effect is seen with the endocyclic COC bending centered at 595 cm^{-1}. In both of these cases conformational limitations imposed by the hydrogen bonding force the molecule to be in a preferred, fixed ``ring-pucker'' and/or glycosidic bond angle and therefore the spectral contributions to this mode are collapsed into a narrower range, brightening the signal. The opposite effect is seen with the torsional modes (centered at 700 cm^{-1}) around the glycosidic bond as hydrogen bonding effectively suppresses these vibrations. The symmetric COC stretching mode associated with the glycosidic link (c.a. 845 cm^{-1}) is blue-shifted in the wet spectrum due to the movement of both carbon atoms against the symmetric, hydrogen bonding induced polarization of the COC bond. The antisymmetric COC stretching mode (c.a. 1160 cm^{-1}), on the other hand, experiences no net force from this induced polarization but is still blue-shifted by the conformational constraints on the ring imposed by the hydrogen bonding, as mentioned above.

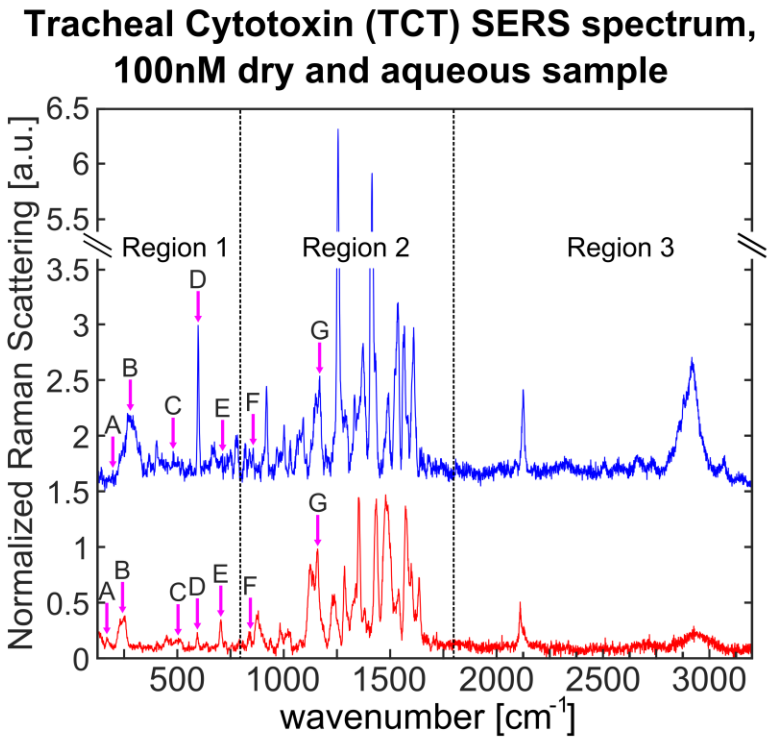

	Dry wavenumber	Wet wavenumber	Key Structure	Vibrational Mode
A	168cm^{-1}	143cm^{-1}	N-ACETYL	Acetyl torsion (N)
B	250cm^{-1}	270cm^{-1}	N-ACETYL	Acetyl torsion and deformation
C	500cm^{-1}	512cm^{-1}	β(1-4′) GLY	Glycosidic link deformation
D	593cm^{-1}	598cm^{-1}	NAG/NAM	Endocyclic COC deformation
E	704cm^{-1}	707cm^{-1}	β(1-4′) GLY	Glycosidic link torsion
F	842cm^{-1}	856cm^{-1}	β(1-4′) GLY	Glycosidic link symmetric stretching
G	1159cm^{-1}	1169cm^{-1}	β(1-4′) GLY	Glycosidic link asymmetric stretching

Figure 3.4. SERS spectra for 100nM tracheal cytotoxin (TCT). TCT SERS spectra under wet (blue) and dry (red) conditions is depicted. The data is divided into four major regions as outlined in the text. Letters correspond to the peaks identified in the inset table.

The mode at 836 cm^{-1} is associated with the CH_3 stretch found in both the alanine and alanyl components of the peptide.[26] The prominent peak at 1479 cm^{-1} is associated with CH_2 bending/scissoring and has been shown to be indicative of residues with CH_2 chains - in our case along the backbones of glutamyl and diaminopimelic acid (DAP).[28,31] An interesting and unexpected structure found in both the wet and dry spectra is that of a

ketene[32] C=C=O type bond at 2150 cm^{-1}. While this molecule does not normally feature this structure, it is likely that the surface attachment of the molecule combined with the high SERS fields can liberate electrons from the gold bulbs allowing a dehydration type reaction converting carboxylic acid groups to this ketene structure.

Region 2 contains vibrations from a set of structures that were distinctively affected by the transition from wet to dry measurement. These are highlighted in **Figure 3.5**. In particular, there are two chemical structures that are uniquely affected by the presence of water: peptide bonds and carboxylic acid groups. The peptide bond (diagrammed in **Figure 3.5**) produces four easily distinguishable "amide" modes[27]: mode I is primarily a carbonyl stretching mode, II is an out of phase and III is an in phase mix of the in-plane N-H bending and the central C-N stretching mode, and the fourth "backbone" mode is a coupled stretching along the C-N-C backbone of the peptide bond. In the peptide diagram in **Figure 3.5** the two locations of possible water based hydrogen bonding are colored, either on the carbonyl oxygen (red) or the nitrogen bound hydrogen (blue) and both cases can have different effects on each of the four amide vibrations[33]. In the case of bonding to the oxygen, water induced conjugation effects lower the order of the carbonyl bond and strengthen the central C-N bond. In the case of bonding to the hydrogen, water molecules induce a strong polarization of the N-H bond while also lowering the carbonyl bond order and increasing the strength of the C-N bond. The combination of these perturbations has the overall effect of red-shifting the amide I bond, splitting the amide II band into separate red and blue shifted components and blue-shifting the amide III and backbone bands[33]. The amide II case is particularly interesting as this mode is primarily composed of the N-H bending vibration and in both hydrogen

bonding cases conjugation effects lengthen the N-H bond which would seem to push this vibration to lower energies. However when water is complexed to the hydrogen itself, this bond lengthening is accompanied by a strong electronic polarization effect which serves to induce a large (>20 cm^{-1}) blue shift in the vibration[33]. Amide III and the backbone vibrations are strongly dependent on the C-N bond strength and are thus blue-shifted based on the effects of hydrogen bonding in both cases.

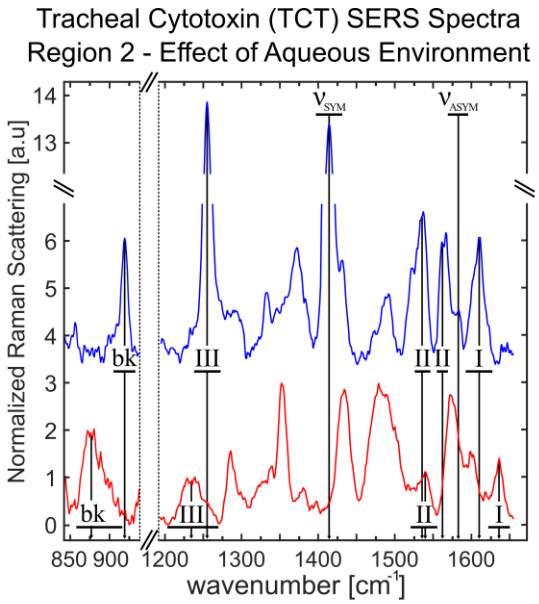

Structure	Mode	Dry	Wet	Key Bond(s)
N-Acetyl Amide	Amide I	1635cm^{-1}	1611cm^{-1}	ν(C=O)
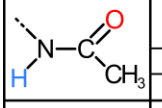	Amide II	1539cm^{-1}	1535cm^{-1}	β(NH)-ν(CN)
			1565cm^{-1}	β(NH)-ν(CN)
	Amide III	1326cm^{-1}	1346cm^{-1}	ν(CN)+β(NH)
	Amide bk	880cm^{-1}	919cm^{-1}	ν(R'C-NR)
Carboxylate Ion	Symmetric	--	1415cm^{-1}	ν_s(O-C-O)
	Asymmetric	--	1583cm^{-1}	ν_a(O-C-O)

Figure 3.5. Detail of spectral region 3 from the SERS spectra for Tracheal Cytotoxin (TCT). TCT spectra under 100 nM wet (blue) and dry (red) conditions is depicted. Roman numerals correspond to specific amide vibrational modes.

In solution, the resonance structure of the deprotonated carboxylate ion causes the once distinct C=O and C-OH stretching modes to be mixed into an asymmetric and

symmetric stretching mode. These are highlighted in purple in **Figure 3.5** and present as new peaks not seen in the dry spectrum[34]. As the carboxylic acid groups are not sufficiently potent to form a strong acid the population is only partially deprotonated and consequently the peaks associated with the C=O stretching of the protonated carboxylic acid mode are still present in the wet spectrum, although they are split through the water mediated formation of carboxylic acid dimers.[34–36]

The peaks mentioned above were highlighted as those which could play a role in identifying TCT or those which exhibited unique spectral changes between the wet and dry measurements. However, they only represent a fraction of the total number of peaks that were seen and identified. The enormous enhancement over the entire laser illumination area and minimal inhomogeneous broadening afforded by the nanobulb substrate, along with the spectral resolution of the Raman instrument, resulted in densely peaked SERS spectra. By studying the similarities and differences between TCT spectra under different conditions we can isolate a set of invariant peaks that can constitute a first step towards creating a culture-free test for certain gram negative bacterial infections.

3.2.3 Use of nanobulbs for 2D spectroscopic techniques: single-strand DNA

Single stranded DNA (ssDNA) can play a multitude of critical roles in biological processes, both in vitro and in vivo, including: targeted binding of specific molecules, strand capping functions in telomeres, and preventing or allowing transcription of certain regions of nucleic acids. These actions are typically mediated by the secondary folded structure of the strand rather than by the primary sequence itself. However, as noted in previous studies, ssDNA without a high degree of being “self-complementary” does not tend to have a fixed secondary structure.[37] This makes the Raman analysis of ssDNA

significantly harder for two reasons: (1) The strand is flexible and free to move, allowing portions of the strand to drift in and out of the sensing region, forcing long signal acquisitions in an attempt to ensure sufficient sampling "time-averaged" Raman spectrum. (2) The majority of Raman analysis has been carried out on double stranded DNA or hybridized DNA-RNA pairs where the sterics snap the molecule into a well defined A or B-type configuration. An ssDNA molecule without a well-defined secondary structure is free to thermally gyrate in the measurement buffer and therefore the well-defined group frequencies associated with structural elements such as sugar pucker, glycosidic bond angle and dihedral phosphodiester angle no longer apply.

These combined effects would seem to make it nearly impossible to use ssDNA strands as SERS-based label-free hybridization probes for micro RNA (μRNA) and messenger RNA (mRNA) quantification. These measurements require a set of peaks characteristic of the ssDNA probe as well as a distinct set corresponding to the target molecule such that one can compare their relative intensities in a single collection to estimate the number of bound targets. The lack of a robust ssDNA spectrum would rule out its use in early disease screening (μRNA) and single cell transcriptomics (mRNA) where detection of trace amounts of RNA (copy number < 100) is crucial.[38,39,40] Attempts at solving this problem by taking long-acquisition spectra tend to smear out the data, hiding characteristic peaks in the midst of wide overlapping signals. However, the amplification afforded by the nanobulb substrates allows us to take short, snapshots of the ssDNA during a controlled perturbative experiment. From a series of spectra taken while perturbing a variable such as temperature, pH, or ion concentration we can extract distinct peaks that were previously unapparent using well-studied two-dimensional

correlated spectroscopic (2DCS) techniques;[41,42,43,44] both this method and the peaks found as a result of it can be applied when using ssDNA as a low copy number hybridization probe in future experiments.

Briefly stated the series of spectra obtained while controllably changing an experimental variable can be decomposed into "synchronous" and "asynchronous" spectra. The synchronous spectrum relates whether the change in signal intensity measured at two different wavenumbers is positively, negatively or uncorrelated. The main diagonal of the synchronous spectrum is referred to as the "autopeak correlation," and describes the extent of the intensity change at a given wavenumber during the course of the perturbation. The asynchronous spectrum describes the order in which uncorrelated spectral variables change intensity. In the work presented below we conduct a 2DCS analysis on a representative strand of ssDNA with temperature as the perturbed variable.

The sequence investigated was the complement of miR-10b, a μRNA that when found in the brain/spinal fluid that is a unique marker for glioblastoma.[45,38] The synthesized complement to miR10b (HS-$(CH_2)_6$-[5'-CACAAA TTCGGT TCTACA GGGTA-3'], IDT Technologies) had a hexane linked thiol group for attachment to the gold bulbs at the 5' end. Au nanobulb substrates were rigorously cleaned by O_2 plasma, washed with isopropanol, deionized water and then incubated with a prepared 1 μM solution of ssDNA in phosphate buffer for 30 minutes. After incubation, substrates were rinsed thoroughly with isopropanol and buffer to remove any excess ligand and finally immersed in 0.1 M Sodium Phosphate Buffer (Na_2HPO_4, pH = 8) for measurement. Just prior to measurement, these substrates were heated to 80 ^{o}C and allowed to cool to room temperature to eliminate any artifacts or secondary structure induced during

functionalization. Measurements were taken in the same Raman microscope with use of a heating stage (Instec Inc.) to vary the temperature.

The temperature series data is shown in **Figure 3.6**. Applying the 2DCS method described above we calculated the synchronous spectrum, shown in **Figure 3.6(b)** with the intensity normalized by setting the highest positive correlation to 1 (plot limited to the 1000 to 1700 cm^{-1} region for clarity). This plot is dominated by the 1572 cm^{-1} autopeak; indicating the change in temperature had a significant effect on the portion of the ssDNA that provided this signal, specifically the signal at 1572 cm^{-1} decreased with increasing temperature. Tracking along the x or y direction (corresponding to cross-correlations to this wavenumber), we can identify the set of peaks that are strongly positively correlated with this feature, indicating that their physical origin is related to that of the 1572 cm^{-1} feature. However, not all the peaks seen on the main diagonal are cross-correlated with this feature (notably at 1528 and 1650 cm^{-1}). This indicates that there are at least two portions of the ssDNA which contribute to the total SERS signal, but experience the change in temperature differently.

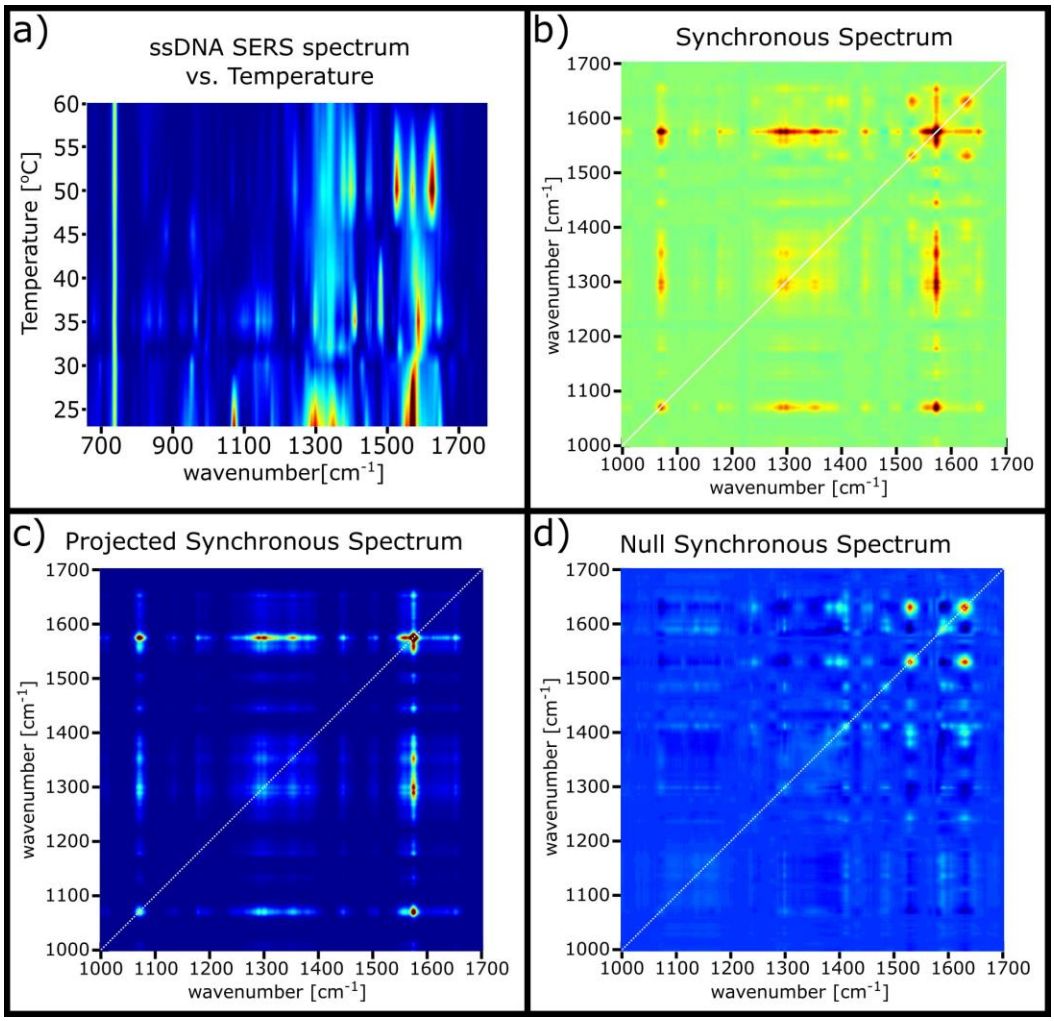

Figure 3.6. Analysis of 23bp ssDNA strand attached to nanobulbs via hexanethiol linker. (a) Two-dimensional data set of Raman spectra collected at temperatures between 23 ºC and 60ºC. (b) Synchronous spectrum of temperature series data. (c) Synchronous spectrum of data projected onto 1572 cm^{-1} peak. (d) Synchronous spectrum of the null-set of the projected data showing greater detail in the 1300-1700 cm^{-1} region.

To examine this behavior in greater detail we utilized a positive projection 2DCS technique.[43] This method allowed us to split the data into two sets with either similar or dissimilar temperature dependence compared to the peak at 1572 cm^{-1}. Peaks with behavior positively correlated with this peak make up the projected set and those anti or uncorrelated make up the null set. The normalized synchronous spectra of the projected

and null sets are given in **Figure 3.6(c)** and **Figure 3.6(d)**, respectively. Using these two plots we proceeded to develop vibrational assignments for significant autopeaks as depicted in **Figure 3.7**.

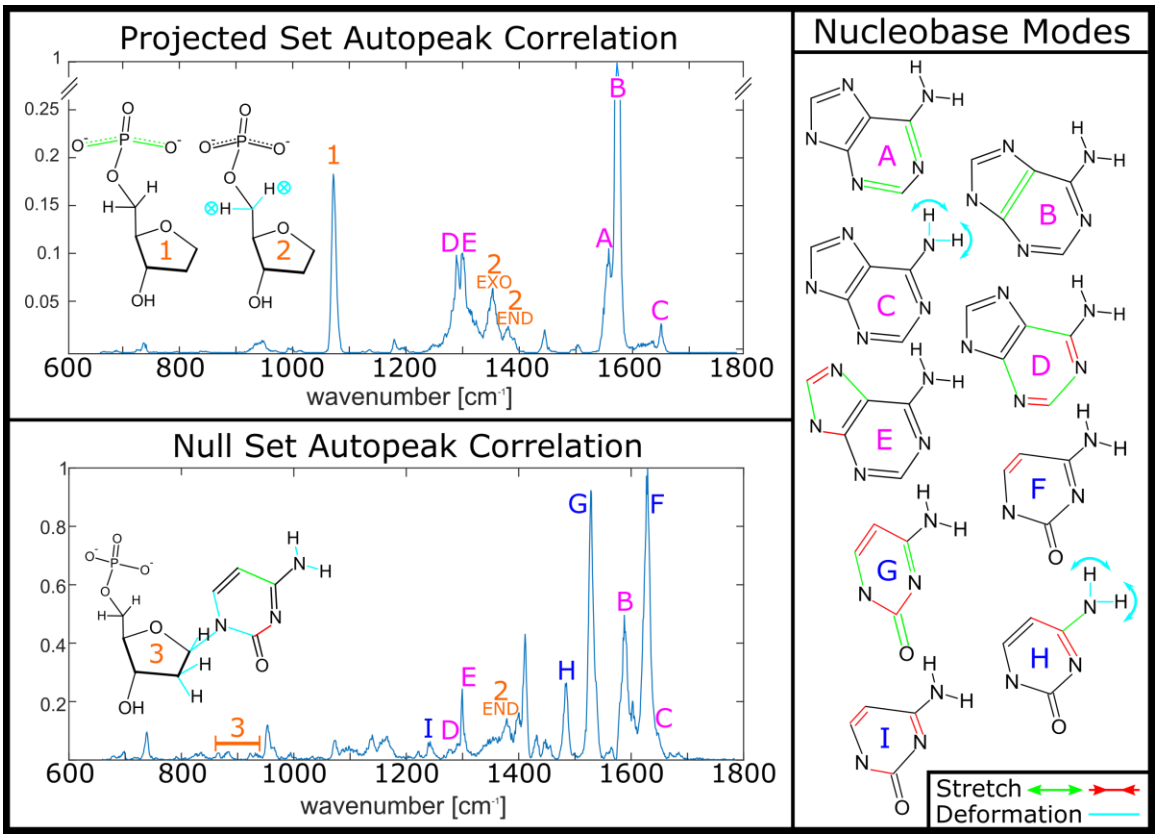

Figure 3.7. Autopeak correlation spectra of ss-DNA. The autopeak correlation spectra of the projected (top) and null (bottom) data sets. Vibrations A-E correspond to adenine and F-I correspond to cytosine. Vibration 1 is the symmetric νs(OPO) stretch of the phosphodiester bond; vibration 2 is out of plane CH2 wagging, where EXO are the CH2 along the backbone and END are those in the ring; vibration 3 is a complex coupled mode of two spectrally close peaks, a ring bend/amine deformation coupled across the glycosidic sugar bond to a CH out of plane bending mode. Note that only adenine related peaks are seen in the projected spectra while both adenine and cytosine peaks are seen in the null spectra. Nucleobase modes are as identified as follows: A: adenosine C=N stretch (1558 cm-1), B: adenosine. central C=C stretch (1572 cm-1) C: adenosine NH2 scissor, (1650 cm-1), 1: backbone PO2- symmetric stretch (1071 cm-1), 2: Sugar, C5'H2 wagging for exo (1271 cm-1) and endo (1285 cm-1) conformations, 3: band of coupled sugar deformation and cytosine ring stretch mode #15, D: adenosine (1289 cm-1) 6 member kekule, E: adenosine (1300 cm-1) 5 member kekule F: cytosine, 1629 cm-1, C5=C6 ring stretch, G: cytosine, 1528 cm-1 ring stretch mode #v9, H: cytosine NH2 scissor combined with C4-NH2 stretch, an C4-C5/C4=N3 stretch, I: cytosine 1267 cm-1, ring stretch mode #14. Mode numbers are from a Nishimura et Al. 46 All atom numbering is standard for nucleobases.

From **Figure 3.7** we can see two unique effects. First, although the ssDNA contained all four nucleobases it is clear that cytosine and adenine modes dominate the spectra. This may be due to rapid decay in local E-field magnitude (and subsequent SERS signal) as a function of distance from the metal surface as illustrated by the mode patterns in figure 2. This distance dependence causes the more proximal nucleobases (5'-CACAAA...) to contribute most to the SERS signal. Second, we observed that the projected spectrum only contained contributions from adenine; indicating that as the temperature was increased the relative contribution of adenine to the total signal decreased. This second effect can be related to the increased radius of gyration of the ssDNA strand with increased temperature. The additional thermal energy provided by higher temperatures allows the strand to spend a greater proportion of its time in an extended state, ensuring that for a sample of ssDNA strands the three adenine nucleobases at positions 4-6 are on average further from the nanobulb surface, and therefore contribute less to the total signa than they would at a lower temperature. The peaks found in the projected set, by definition, all exhibit behavior that is positively correlated with each other and with this trend and therefore can be thought of as arising from the same portion of the ssDNA strand (bases 4-6).[43] The peaks found in the null set have behavior anti-/uncorrelated with those in the projected set and must therefore come from a different portion of the ssDNA strand, and can be thought of as peaks with increasing relative contribution to the total SERS signal with increasing temperature. Our peak assignments indicate that the contributions to the null set autopeak spectrum come primarily from cytosine with some of the brighter adenine peaks seen at 1300, 1588, 1602, and 1650 cm^{-1}. When we examine the off-diagonal correlation coefficients of these

peaks in the synchronous spectrum of the null set (**Figure 3.6(d)**), we note that these adenine peaks are anti-correlated with the cytosine peaks, making it likely that these peaks correspond to the more proximal adenine second from the 5' end and the cytosine peaks can be assigned to the nucleobases at positions1 and 3 from the 5' end.

Using a temperature based 2DCS analysis with the rapid collection afforded by the nanobulb substrates we were able to pinpoint the structural origins of peaks found in the overall SERS signal. These peaks can be used a basis set to decompose a highly overlapping spectrum or to create set of characteristic peaks that are unique to the ssDNA molecule for use in a hybridization based quantification scheme. This method, combined with the nanobulb substrate, opens the door to performing low copy number, hybridization based RNA quantification for disease screening or single cell transcriptomics.

This paper outlines the hybrid top-down/bottom-up fabrication and testing of a SERS substrate that provides a consistent high enhancement factor and narrow spectral linewidth over extended length scales and across a multitude of molecular symmetries. Fabrication of the nanobulb substrates was performed using only standard silicon CMOS methods to seed a critical bottom-up assembly technique resulting in consistent fabrication and substrate performance. The enhancement factor provided by the substrate was measured using thiophenol as a probe molecule and compared to neat thiophenol measurements, yielding an average SSEF in excess of 10^{10} across a >3000 cm^{-1} wavenumber range and set of four unique molecular symmetries. Mapping scans were used to characterize the spatial variation in Raman spectral properties across extended nanobulb arrays and we report a less than 10% variation in SSEF, 2.5% variation in

linewidth and 0.01% variation in measured peak position for a set of thiophenol vibrational modes. Subsequently the nanobulb arrays were used to identify the presence of TCT, without the use of targeted binding, via the identification of peaks specific to the disaccharide head, amide vibrations in the peptide tail and predictable shifts between wet and dry measurement conditions. The nanobulbs arrays were also used for the 2D spectroscopic analysis of heating ss-DNA. The magnitude and consistency of the enhancement factor of these substrates uniquely positions them to be used in the future for ultra-low concentration sensing and quantification applications. The scalability ensured by the incorporation of top-down fabrication techniques ensures that such future applications could extend past the lab and foster the creation of a novel medical devices aimed at detecting and quantifying low-copy number analytes. Together these experiments indicate that the readily manufacturable gold nanobulb substrates can serve as a promising new platform for sensitive optical biosensing applications. Future work aims to use these substrates as sensors with targeted functionalization to directly analyze complex bio-solutions without the need for sample preparation. Specifically, functionalizing the gold bulbs with a thiolated binding aptamer[47] will yield both specificity and the ability to make both selected and sensitive measurements. By combining the spectral detail afforded the nanobulb substrate with two-dimensional correlated spectroscopic techniques or electrochemical methods, it would be possible to analyze the changing behavior of systems with previously unprecedented detail. Additionally, the substrates used in this letter can play an integral part in analyzing chemical and physical changes at the cellular surface of both gram negative and gram positive bacteria with high sensitivity. This can grant further insight into inter-cellular

transport mechanisms in these organisms and provide a basis for study for alternative antibacterial treatment techniques.

Acknowledgements

This work was supported by the Gordon and Betty Moore Foundation under the MSN156910 grant. The authors would like to thank the Goldman research group at the University of North Carolina for the supply of purified TCT and also the staff of the Kavli Nanoscience Institute for their continued help. B.C.M. and A.R.T. acknowledge support from the Office of Naval Research (Award No. N000141210574) and a DURIP grant (Award No. N000141310655).

Chapter 3, in part, is currently being prepared for submission for publication of the material by Brandon C. Marin, † Sameer S. Walavalkar, † Chieh-feng Chang, † Andrea R. Tao, Axel Shearer, and Scott Fraser. (†Equal contribution) The dissertation author was the primary investigator and author of this material.

References

(1) Henry, M. D.; Walavalkar, S.; Homyk, A.; Scherer, A. Alumina Etch Masks for Fabrication of High-Aspect-Ratio Silicon Micropillars and Nanopillars. *Nanotechnology* 2009, *20* (25), 255305.

(2) Cookson, B. T.; Cho, H.; Herwaldt, L. A.; Goldman, W. E. Biological Activities and Chemical Composition of Purified Tracheal Cytotoxin of Bordetella Biological Activities and Chemical Composition of Purified Tracheal Cytotoxin of Bordetella Pertussis. 1989, *57* (7), 2223–2229.

(3) Goldman, W. E.; Cookson, B. T. Structure and Functions of the Bordetella Tracheal Cytotoxin. *Tokai J. Exp. Clin. Med.* 1988, *13 Suppl*, 187–191.

(4) Rosenthal, R. S.; Nogami, W.; Cookson, B. T.; Goldman, W. E.; Folkening, W. J. Major Fragment of Soluble Peptidoglycan Released from Growing Bordetella Pertussis Is Tracheal Cytotoxin. *Infect. Immun.* 1987, *55* (9), 2117–2120.

(5) Oskooi, A. F.; Roundy, D.; Ibanescu, M.; Bermel, P.; Joannopoulos, J. D.; Johnson, S. G. Meep: A Flexible Free-Software Package for Electromagnetic Simulations by the FDTD Method. *Comput. Phys. Commun.* 2010, *181* (3), 687–702.

(6) Vial, A.; Grimault, A.-S.; Macías, D.; Barchiesi, D.; de la Chapelle, M. L. Improved Analytical Fit of Gold Dispersion: Application to the Modeling of Extinction Spectra with a Finite-Difference Time-Domain Method. *Phys. Rev. B* 2005, *71* (8), 85416.

(7) Walavalkar, S. S.; Latawiec, P.; Homyk, A. P.; Scherer, A. A. Scalable Method for the Fabrication and Testing of Glass-Filled, Three-Dimensionally Sculpted Extraordinary Transmission Apertures. *Nano Lett.* 2014, *14* (1), 311–317.

(8) Walavalkar, S. S.; Hofmann, C. E.; Homyk, A. P.; Henry, M. D.; Atwater, H. A.; Scherer, A. Tunable Visible and Near-IR Emission from Sub-10 Nm Etched Single-Crystal Si Nanopillars. *Nano Lett.* 2010, *10* (11), 101004110737018.

(9) Ricci, E.; Novakovic, R. Wetting and Surface Tension Measurements on Gold Alloys. *Gold Bull.* 2001, *34* (2), 41–49.

(10) Švorčík, V.; Siegel, J.; Šutta, P.; Mistrík, J.; Janíček, P.; Worsch, P.; Kolská, Z. Annealing of Gold Nanostructures Sputtered on Glass Substrate. *Appl. Phys. A* 2010, *102* (3), 605–610.

(11) Paulson, G. G.; a.L. Friedberg. Coalescence and Agglomeration of Gold Films. *Thin Solid Films* 1970, *5* (1), 47–52.

(12) De Los Santos, V. L.; Lee, D.; Seo, J.; Leon, F. L.; Bustamante, D. A.; Suzuki, S.; Majima, Y.; Mitrelias, T.; Ionescu, A.; Barnes, C. H. W. Crystallization and Surface Morphology of Au/SiO2 Thin Films Following Furnace and Flame Annealing. *Surf. Sci.* 2009, *603* (19), 2978–2985.

(13) Le Ru, E. C.; Blackie, E.; Meyer, M.; Etchegoin, P. G. Surface Enhanced Raman Scattering Enhancement Factors: A Comprehensive Study. *J. Phys. Chem. C* 2007, *111* (37), 13794–13803.

(14) Kolwas, K.; Derkachova, a.; Shopa, M. Size Characteristics of Surface Plasmons and Their Manifestation in Scattering Properties of Metal Particles. *J. Quant. Spectrosc. Radiat. Transf.* 2009, *110* (14–16), 1490–1501.

(15) Meier, M.; Wokaun, A. Enhanced Fields on Large Metal Particles: Dynamic Depolarization. *Opt. Lett.* 1983, *8* (11), 581–583.

(16) Messinger, B. J.; Von Raben, K. U.; Chang, R. K.; Barber, P. W. Local Fields at the Surface of Noble-Metal Microspheres. *Phys. Rev. B* 1981, *24* (2), 649–657.

(17) Aggarwal, R. L.; Farrar, L. W.; Greeneltch, N. G.; Duyne, R. P. Van; Polla, D. L. Measurement of the Raman Line Widths of Neat Benzenethiol and a Self-Assembled Monolayer (SAM) of Benzenethiol on a Silver-Coated Surface-Enhanced Raman Scattering (SERS) Substrate. *Appl. Spectrosc. Vol. 66, Issue 7, pp. 740-743* 2012, *66* (7), 740–743.

(18) Dworkin, J. The Medium Is the Message: Interspecies and Interkingdom Signaling by Peptidoglycan and Related Bacterial Glycans. *Annu. Rev. Microbiol.* 2014, *68*, 137–154.

(19) Jarvis, R. M.; Goodacre, R.; Box, P. O.; Street, S.; Manchester, M. Discrimination of Bacteria Using Surface-Enhanced Raman Spectroscopy. *Anal. Chem.* 2004, *76* (1), 40–47.

(20) Goldman, W. E.; Klapper, D. G.; Baseman, J. B. Detection, Isolation, and Analysis of a Released Bordetella Pertussis Product Toxic to Cultured Tracheal Cells. *Infect. Immun.* 1982, *36* (2), 782–794.

(21) Kouach-Alix, I.; Huvenne, J. P.; Legrand, P.; Vergoten, G. A Vibrational Molecular Force Field of Model Compounds with Biological Interest. VII. Harmonic Dynamics of N-Acetyl-α-D-Muramic Acid and N-Acetyl-β-D-Neuraminic Acid in the Crystalline State. *J. Mol. Struct.* 1994, *327* (1), 1–21.

(22) Kouach-Alix, I.; Vergoten, G. A Vibrational Molecular Force Field of Model Compounds with Biological Interest. V. Harmonic Dynamic of N-Acetyl-α-D-Glucosamine in the Crystalline State. *J. Mol. Struct.* 1994, *323*, 39–51.

(23) Carlson, K. P. An Investigation of the Vibrational Spectra of Cellodextrins, Lawrence University - Appleton, Wisconsin, 1979.

(24) Edwards, H. G. M.; Farwell, D. W.; Williams, A. C. FT-Raman Spectrum of Cotton : A Polymeric Biomolecular Analysis. *Spectrochim. Acta* 1994, *50A* (4), 807–811.

(25) Dauchez, M.; Lagant, P.; Derreumaux, P.; Vergoten, G.; Sekkal, M.; Sombret, B. Force Field and Vibrational Spectra of Oligosaccharides with Different Glycosidic linkages—Part II. Maltose Monohydrate, Cellobiose and Gentiobiose. *Spectrochim. Acta Part A Mol. Spectrosc.* 1994, *50* (1), 105–118.

(26) Suh, J. S.; Moskovits, M. Surface-Enhanced Raman Spectroscopy of Amino Acids and Nucleotide Bases Adsorbed on Silver. 1986, No. 21.

(27) Barth, A.; Zscherp, C. What Vibrations Tell about Proteins. *Q. Rev. Biophys.* 2002, *35* (4), 369–430.

(28) Ivleva, N. P.; Wagner, M.; Horn, H.; Niessner, R.; Haisch, C. Towards a Nondestructive Chemical Characterization of Biofilm Matrix by Raman Microscopy. *Anal. Bioanal. Chem.* 2009, *393* (1), 197–206.

(29) Sekkal, M.; Dincq, V.; Legrand, P.; Huvenne, J. P. Investigation of the Glycosidic Linkages in Several Oligosaccharides Using FT-IR and FT Raman Spectroscopies. *J. Mol. Struct.* 1995, *349*, 349–352.

(30) Song, S.; Asher, S. A. UV Resonance Raman Studies of Peptide Conformations in Poly(L-Lysine), Poly(L-Glutamic Acid), and Model Complexes: The Bases for Protein Secondary Structure Determinations. *J. Am. Chem. Soc.* 1989, *111*, 4295–4305.

(31) Ramirez, F. J.; Tunon, I.; Silla, E. Amino Acid Chemistry in Solution : Structural Study and Vibrational Dynamics of Glutamine in Solution . An Ab Initio Reaction Field Model. *J. Phys. Chem.* 1998, *5647* (98), 6290–6298.

(32) Colthup, N. *Introduction to Infrared and Raman Spectroscopy*, E-Book.; Elsevier/Academic Press, 2012.

(33) Myshakina, N. S.; Ahmed, Z.; Asher, S. A. Dependence of Amide Vibrations on Hydrogen Bonding. *J. Phys. Chem. B* 2008, *112* (38), 11873–11877.

(34) Suh, J. S.; Kim, J. Three Distinct Geometries of Surface-Adsorbed Carboxylate Groups. *J. Raman Spectrosc.* 1998, *29* (2), 143–148.

(35) Sutton, C. C. R.; Franks, G. V; Da Silva, G. Modeling the Antisymmetric and Symmetric Stretching Vibrational Modes of Aqueous Carboxylate Anions. *Spectrochim. Acta - Part A Mol. Biomol. Spectrosc.* 2015, *134*, 535–542.

(36) Stewart, S.; Fredericks, P. . Surface-Enhanced Raman Spectroscopy of Amino Acids Adsorbed on an Electrochemically Prepared Silver Surface. *Spectrochim. Acta Part A Mol. Biomol. Spectrosc.* 1999, *55* (7–8), 1641–1660.

(37) Liang, X.; Kuhn, H.; Frank-Kamenetskii, M. D. Monitoring Single-Stranded DNA Secondary Structure Formation by Determining the Topological State of DNA Catenanes. *Biophys. J.* 2006, *90* (8), 2877–2889.

(38) Gaur, A.; Jewell, D. A.; Liang, Y.; Ridzon, D.; Moore, J. H.; Chen, C.; Ambros, V. R.; Israel, M. A. Characterization of microRNA Expression Levels and Their Biological Correlates in Human Cancer Cell Lines. *Cancer Res.* 2007, *67* (6), 2456–2468.

(39) Panta, P.; Venna, V. R. Salivary RNA Signatures in Oral Cancer Detection. 2014, *2014* (1).

(40) Yakob, M.; Fuentes, L.; Wang, M. B.; Abemayor, E.; Wong, D. T. W. Salivary Biomarkers for Detection of Oral Squamous Cell Carcinoma: Current State and Recent Advances. *Curr. Oral Heal. Reports* 2014, *1* (2), 133–141.

(41) Noda, I. Generalized Two-Dimensional Correlation Method Applicable to Infrared, Raman, and Other Types of Spectroscopy. *Appl. Spectrosc.* 1993, *47* (9), 1329–1336.

(42) Noda, I. Two-Dimensional Correlation Analysis of Unevenly Spaced Spectral Data. *Appl. Spectrosc.* 2003, *57* (8), 1049–1051.

(43) Noda, I. Double Two-Dimensional Correlation Analysis – 2D Correlation of 2D Spectra. *J. Mol. Struct.* 2010, *974* (1–3), 108–115.

(44) Noda, I.; Ozaki, Y. *Two- Dimensional Correlation Spectroscopy*; Wiley, 2004; .

(45) Gabriely, G.; Yi, M.; Narayan, R. S.; Niers, J. M.; Wurdinger, T.; Imitola, J.; Ligon, K. L.; Kesari, S.; Esau, C.; Stephens, R. M.; Tannous, B. A.; Krichevsky, A. M. Human Glioma Growth Is Controlled by microRNA-10b. *Cancer Res.* 2011, *71* (10), 3563–3572.

(46) Nishimura, Y.; Tsuboi, M.; Sato, T.; Aoki, K. Conformation-Sensitive Raman Lines of Mononucleotides and Their Use in a Structure Analysis of Polynucleotides: Guanine and Cytosine Nucleotides. *J. Mol. Struct.* 1986, *146*, 123–153.

(47) Ferreira, I. M.; de Souza Lacerda, C. M.; de Faria, L. S.; Corrêa, C. R.; de Andrade, A. S. R. Selection of Peptidoglycan-Specific Aptamers for Bacterial Cells Identification. *Appl. Biochem. Biotechnol.* 2014.

Chapter 4

Metal-Graphene Composites: Current Applications and Trends in Chemical, Mechanical, and Optical Sensing

Brandon C. Marin,[a] Julian Ramirez, [a] Eden Aklile,[a]

and Darren J. Lipomi[a]

[a]*NanoEngineering Department, University of California, San Diego. 9500 Gilman Drive MC 0448, La Jolla, CA 92093-0448*

Abstract

Graphene decorated with metal nanoparticles exhibits emergent electronic, optical, and mechanical properties that neither the graphene nor the metal possess alone. That is, these nanoisland films on graphene can be treated as a kind of metamaterial that can be responsive to a wide range of physical, chemical, and biological stimuli. By controlling the shape, size, and pattern of noble metal nanoparticles on graphene, a wide range of devices have been developed. This minireview presents multiple methods to deposit metal nanoparticles on graphene, while addressing their respecitve strenghts and drawbacks when it comes to cost, film morphology, and controllability. More importantly, this minireview highlights the multiple applications in which these nanocomposite films have been used. The need to decouple the multiple stimuli that gives rise to its multifunctionality is also discussed.

4.1 Introduction

Graphene, when decorated with noble metal nanoparticles ("metallic nanoislands"), exhibits interesting electronic, mechanical, and optical properties that are not found in either material separately. For example, the deposition of metal particles onto graphene can change its band gap,[1,2] optical properties,[3,4] and give rise to strain-sensitive properties such as piezoresistant[5] and "piezoplasmonic" effects.[6] Such metal nanoisland-graphene composite films can thus be treated as a type of metamaterial, prompting a considerable amount of research in recent years.[7,8,9] In many cases, the addition of graphene as a thin support to nanoislands allows for easy transfer and manipulation of the composite material.[10,11,12,13] New phenomena have emerged as a

result of interfacing metal with graphene such as enhancements in optical and electronic gauge factors, photocurrent generation, and catalytic behavior. These phenomena, along with ease of manipulability, have made metal nanoisland-graphene composites a competitive alternative to other functional thin-film platforms like solid-state semiconductors, functional polymers, and nanoparticle assemblies.

Thin film materials based on solid-state semiconductors, such as III-V materials, offer a variety of electronic and photonic applications but lack flexibility, require lengthy top-down fabrication, and are often incompatible with biology.[14] Functional polymers, such as semiconducting polymers, are often mechanically versatile and cheap but lack easy tunability in terms of surface chemistry. In contrast, recent work has demonstrated that metal nanoisland-graphene composites can be fabricated easily, with high fidelity, and with versatile mechanical properties for applications in biological and chemical sensing.[15] Additionally, the emergent electronic, optical, and chemical properties that arise from a physicochemical interface between metal and graphene present a versatility that is unmatched with any other thin film platform.

This minireview examines the methods of fabrication and properties of metal nanoisland-graphene composites, along with applications in the broad topics of chemistry, energy storage and transport, mechanical sensing, optics, and biological sensing (**Figure 4.1**). We begin by describing the methodologies used to deposit metal nanoparticles on graphene. Several prominent examples in chemical sensing, catalysis, energy conversion, cellular biophysics, and optoelectronic devices will then be discussed.

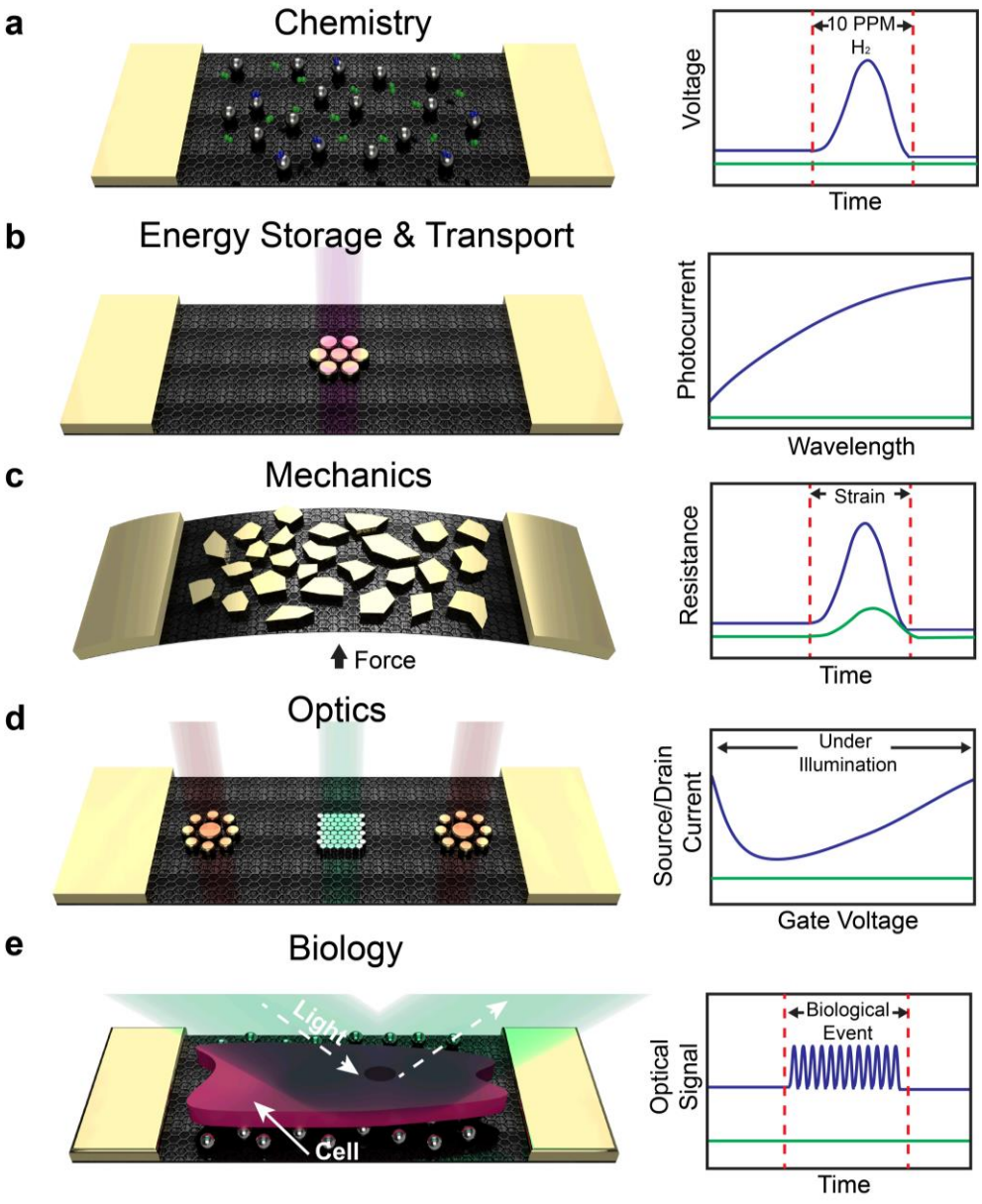

Figure 4.1. Overview of applications for metal nanoislands on graphene. Applications are shown for nanoisland-graphene composites with various types of metals and morphologies on graphene. A graphical comparison of bare graphene (green line) versus nanoisland-graphene composites (blue) in the respective application is shown on the right. (a) Chemical applications include sensing of hydrogen gas using palladium nanoisland-graphene composites. Hydrogen gas dimers are shown in green and chemisorbed dimers are shown in blue. (b) Applications in energy conversion and storage include lithographically patterned gold on graphene for photocurrent generation. (c) Mechanical applications include the detection of strain using changes in the resistivity in gold nanoislands supported by graphene. In this application, sensitivity is augmented by mediation of current between adjacent nanoparticles by quantum tunneling. (d) Optical applications include the use of precisely patterned gold nanoislands supported by graphene for optically doping graphene, e.g., to make light-activated p-n junctions. (e) Applications in biology include the optical detection of biological events, such as cell contractions, using silver nanoislands on graphene.

4.2 Fabrication Strategies

4.2.1 Chemical Synthesis

Wet chemical methods, such as colloidal synthesis, can be used to grow metal nanoislands on graphene.[16,17,18,19,20] Wet chemical methods involve the direct synthesis of particles on a graphene substrate, where the graphene substrate then serves as a nucleation site for crystallites of metal to form and grow. The result is highly crystalline single crystal of metal and the controlled growth of complex geometries such as spheres,[21] rods,[22,23] or even flower-like nanoparticles (**Figure 4.2a**).[17] While a wet chemical method allows control of the shapes of nanoparticles, along with the crystalline quality (**Figure 4.2b**), it also results in a random distribution of metal on the surface of graphene. A random distribution of particles may not have deleterious effects on applications such as catalysis, but limits other applications, such as photonics, that require deterministic placement of nanoparticles. In summary, wet chemistry methods offer a simple way to grow high quality metal crystallites randomly on graphene.

4.2.2 Physical Vapor Deposition

Physical vapor deposition (PVD), such as electron-beam or thermal evaporation, of metal produces disconnected nanoislands at low nominal thicknesses (**Figure 4.2c**). While the shapes of the nanoparticles produced by this method are not deterministic, some degree of control can be achieved by tuning the parameters of deposition. In particular, the unique surface properties of graphene can be used to control the morphology and interconnectivity of the nanoislands during PVD. Rafiee and coworkers first observed that the surface energy of the underlying substrate supporting the graphene

can penetrate through the graphene and interact with the material above it.[24,25] This extraordinary penetration is a phenomenon known as "wetting transparency" and influences the morphology of the metal evaporant as it forms a solid film during PVD. This interaction between the metals—through the graphene film—leads to morphological rearrangement into polycrystalline nanoparticles (**Figure 4.2d**) and thus allows some control over the morphology of the nanoisland-graphene composite.[5] Deposition parameters in PVD systems also offer controllable, simple, and practical ways to influence the morphologies of the nanoislands. For example, modifying the evaporation rate can influence the size and crystallinity of the nanoislands. Changing the substrate temperature during deposition can also influence the size, as the metal particles are kinetically labile, free to move, and agglomerate into larger particles. Similarly, Xiang et Al. reported that thermal annealing of the nanoislands after deposition can also influence nanoisland morphology to assemble into quasi-ordered arrays.[26] While limited in precision, tuning parameters in PVD and post-processing provides a simple, minimalist method to control the morphology of and pattern metal nanoislands on graphene.

4.2.3 Lithography

Electron-beam lithography (EBL) and photolithography, offer high precision in the fabrication of impressively complex patterns of metal on single-layer graphene.[27,28] These methods form patterns with controllable periodicity and geometry, which are critical parameters in plasmonics,[29] light scattering,[30] and quantum tunneling.[31,32] EBL has been used for fabrication of radially symmetric metal nanostructures on graphene, with sub-micron features (**Figure 4.2e, f**). Lithographic methods, however, achieve high control of patterning by sacrificing experimental simplicity.

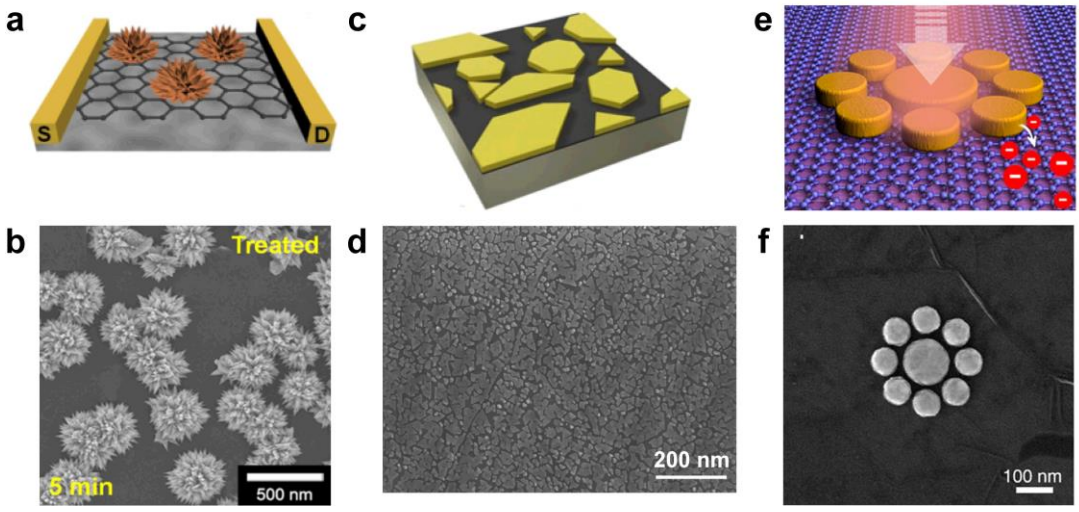

Figure 4.2. Fabrication strategies for metal nanoisland-graphene composites. Methods of fabrication for nanoisland-graphene composites include wet chemical synthesis of metal nanoparticles by immersion of a graphene substrate in a precursor solution. (a) A diagram shows a nanoisland-graphene composite made of palladium nanoflowers on graphene fabricated using a wet chemical method, and an SEM micrograph (b) depicts the final product. Reprinted with permission from reference [17]. Copyright © 2015, Nature Publishing Group. Wet chemical synthesis usually results in stochastically-distributed, shape-controlled, and crystalline metal nanoparticles on the graphene layer. Evaporation of metal directly onto a graphene substrate is a simple, alternative strategy. (c) A diagram shows a nanoisland-graphene composite comprising gold nanoislands on graphene fabricated using PVD, and an SEM micrograph (d) depicts the final product. Reprinted with permission from reference [5]. Copyright © 2016, American Chemical Society. PVD methods offer moderate control over metal morphology and crystallinity. Lithographic methods result in well-controlled patterns of metal. (e) A diagram shows a nanoisland-graphene composite comprised of radially symmetric gold discs patterned on graphene for photonic applications, and an SEM micrograph (f) depicts the final product. Reprinted with permission from reference [28]. Copyright © 2012, American Chemical Society.

4.3 Chemical Applications

4.3.1 Gas Sensing

Metal nanoislands on graphene have been used for as sensors for a variety of gases such as hydrogen,[33,34] NO_x species,[23] and ethanol vapor.[35] In these applications, the graphene acts as an inert, flexible, and conductive substrate for the metal, which undergoes a physicochemical interaction with the gas species of interest. Changes in the resistivity in the nanoisland-graphene composite as the gas interacts with the metal can be

measured. Shin and coworkers demonstrated the use of palladium flower-like nanoparticles supported by graphene for hydrogen sensing as shown in **Figure 4.3a**. In this figure, the shapes of the nanoparticles and sensitivities to gases were determined by the growth time of the nanoparticles.[17] The sensitivity of these nanoisland-graphene composites is controlled by nanoparticle surface area, which limits the chemical kinetics. Longer reaction times lead to larger particles with higher interfacial areas, which increases the rate of by which hydrogen chemisorbs to the surface, and thus increases the sensitivity. This trend with particle size and sensitivity has also been observed for simpler geometries such as palladium spheres on graphene (**Figure 4.3b**).[36] In addition to metals, semiconductor nanoparticles, such as oxides of tin, copper, and zinc, supported by graphene, have been also been used for hydrogen sensors with lower detection limits at higher temperatures than their metal counterparts.[37]

4.3.2 Catalysis

The high ratio of surface area to volume of metal nanoislands on graphene makes them useful substrates in catalysis.[38,39] In these cases, the graphene acts as an inert support for the metal, which serves as the catalyst site. The flexible nature of graphene allows it to bend conformably to a surface of interest, or fold and wrinkle which causes an increase in active-catalytic area per unit volume. While this is a common technique for designing catalyst supports, most supports are rigid ceramics whereas graphene is flexible.[40] Examples of metal nanoislands for liquid-phase catalyst applications includes the use of silver, platinum, palladium, and gold nanoislands supported on graphene for the catalysis of redox reactions (**Figure 4.3c**).[41] Examples of catalysis applications in gaseous phase systems includes the use of graphene-supported platinum nanoislands for

carbon monoxide conversion and liquid-phase high temperature catalysis (**Figure 4.3d**).[42] Catalytic applications are described in detail in the review by Huang and coworkers.[43]

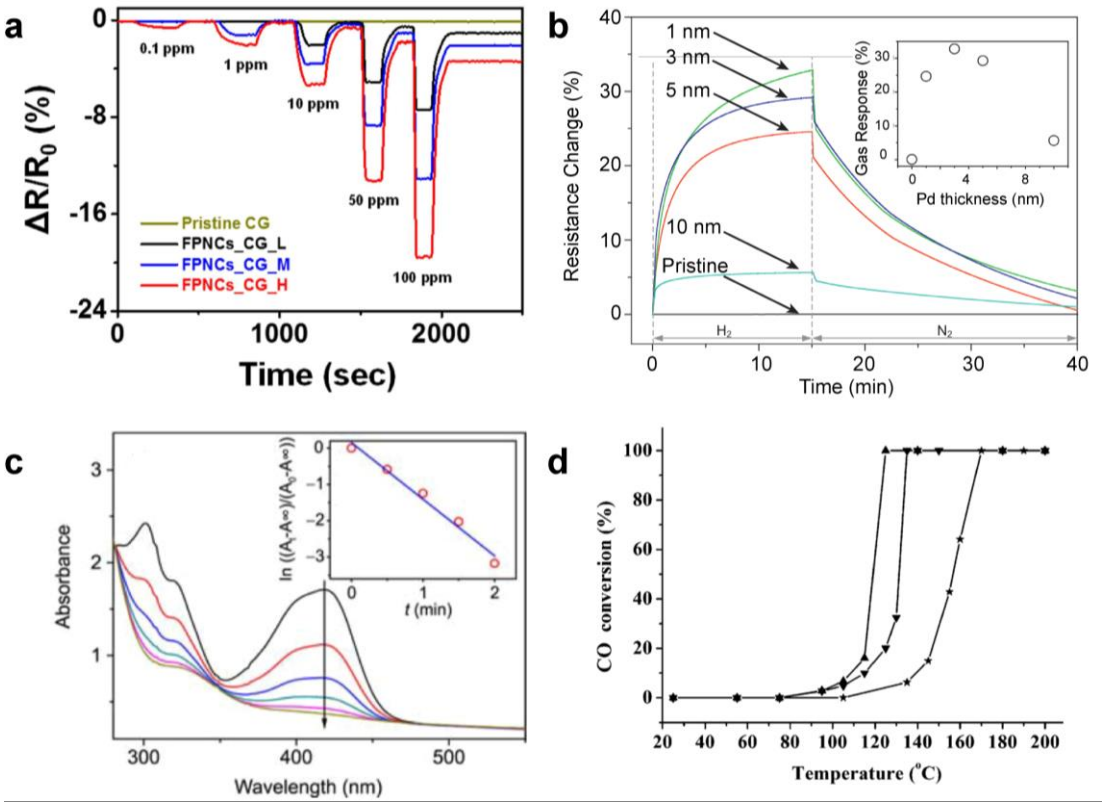

Figure 4.3. Chemical applications for metal nanoisland-graphene composites. Hydrogen gas sensing performance is depicted for palladium nanoflowers (a)(Reprinted with permission from reference [17]. Copyright © 2015, Nature Publishing Group) and nanoislands (b)(Reprinted with permission from reference[36]. Copyright © 2012, Elsevier B.V.) supported by graphene. (c) Time-dependent UV-vis spectra of a solution containing silver nanoislands supported by graphene shows the performance as a catalyst for reduction of hexacyanoferrate (III) by sodium borohydride (Reprinted with permission from reference [41]. Copyright © 2011, Science China Press and Springer-Verlag Berlin Heidelberg. The arrow in (c) points in the direction of increasing time. (d) Catalytic performance (by CO conversion percentage) of platinum nanoparticles supported by reduced-graphene oxide (Pt-rGO) at various temperatures is shown. Reprinted with permission from reference [42]. Copyright © 2014, John Wiley and Sons Inc. The effect of calcination at 500 °C (▼) and 700 °C (▲) on Pt-rGO substrates is also shown in (d) as well as a sample without calcination (★) as a control.

4.4 Mechanical Applications

Mechanical applications for nanoisland-graphene composites generally sense strain piezoresistively. That is, the detection of strain is quantified by changes in electrical resistance. Graphene[44,45,46] and metal[47] are both intrinsically piezoresistive in that both materials undergo a change in resistance when strained. Structurally, the graphene acts as a conductive, stretchable, flexible and strengthening support in metal nanoisland-graphene composites, ensuring the electrical continuity is maintained while undergoing mechanical strain.[48,49] Under smaller strains (<1%), gaps between the metal nanoparticles play a more important role by mediating the transport of electrons by electron tunneling, an effect that causes exponential changes in resistivity in response to strain, which allows amplified sensitivity.[50] Metal-graphene composites, such as gold nanoislands on graphene, have proven to be compatible with cellular biology such as mammalian cardiomyocytes (**Figure 4.4a**). The increased sensitivity by electron-tunneling in gold nanoisland substrates permits the detection of microscale deformations induced by the contractions of mammalian cardiomyocytes (**Figure 4.4b**).[5] Additionally, larger strains are detectable (>1%) owing to the stretchable, underlying graphene which permits sensing of larger-scale deformations such as radial artery contraction for wearable pulse monitoring using gold nanoislands (**Figure 4.4c**). Silver nanoisland-graphene composites have been used for other wearable applications, including speech detection (**Figure 4.4d**) and finger contractions (**Figure 4.4e**).[51]

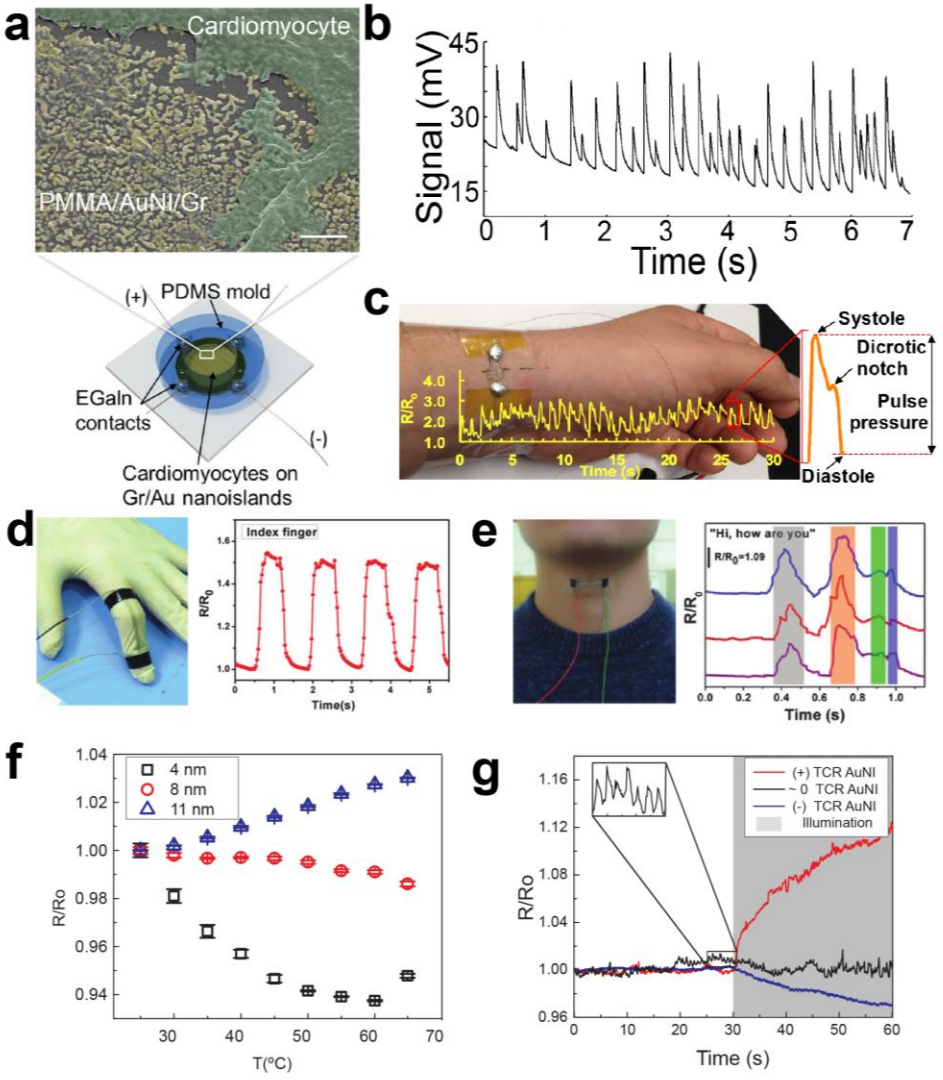

Figure 4.4. Mechanical sensing with metal nanoisland-graphene composites. Metal nanoisland-graphene composites have been used for a variety of strain sensors based on piezoresistivity.(a) Gold nanoislands on graphene (AuNI-Gr) have been shown to be biocompatible substrates for mammalian cardiomyocytes as shown by false-colored SEM micrographs (scale bar 200 nm). A schematic of the sensing platform is also shown in (a). (b) Additionally, AuNI-Gr substrates have been used for the piezoresistive detection of mammalian cardiomyocyte cell contractions through voltage measurements. (c) Wearable strain sensors such as palladium nanoislands supported on graphene have been used for pulse measurements using resistivity changes. (a-c) reprinted with permission from reference [5]. Copyright © 2016, American Chemical Society. Other wearable applications using resistivity changes include the use of graphene-silver nanoparticle networks for the detection of throat contractions induced by speech (d) and detection of finger contractions (e). (d) and (e) reprinted with permission from reference [51] and the Royal Society of Chemistry. The resistance of a AuNI-Gr substrates can vary with temperature, leading to thermal drift. (f) The dependence of resistance on temperature, or the thermal coefficient of resistance (TCR), can be controlled by varying the amount of gold deposited on graphene. Controlling the TCR minimizes thermal drift in wearable sensors as depicted in (g) which shows the thermal drift for three sensors after being heated by a solar simulator lamp. (f) and (g) reprinted with permission from [52]. Copyright © 2017, American Chemical Society.

In all of the examples discussed, detection of mechanical deformation relies on a piezoresistive effect, which is a change in resistivity due to a strain. However, if the thermal coefficient of resistance (TCR) is large then temperature fluctuations will also cause changes in the resistivity that are on the order of changes due to strain, a phenomenon called thermal drift.[53] The minimization of thermal drift in metal nanoisland-graphene composites has been addressed by our group by controlling the content of metal in the composite, which causes a change in the TCR (**Figure 4.4f**).[52] Minimizing the TCR results in a wearable sensor that exhibits minimal thermal drift during abrupt and large temperature fluctuations such as exposure to simulated sunlight (**Figure 4.4g**).

4.5 Energy Transport and Storage

A wide variety of metals have been explored in metal nanoisland-graphene composites for fuel cell applications.[2,54,55,56,57,58,59,60] This topic is reviewed in great detail by Liu and coworkers.[61] Additionally, other two-dimensional materials, such as tungsten disulfide and molybdenum disulfide, have been used for hydrogen evolution in fuel cells.[62] In all these cases, the role of the graphene is functional material and flexible substrate. The choice of metal and its offset in work function from graphene can significantly improve fuel cell efficiency.[63] Other energy conversion applications include the use of symmetric patterns of gold on graphene for the generation of photocurrent by Halas and others. [3,28,64,65,66,67,68] In these applications, the gold is used to enhance light absorption by localized surface plasmon resonance, and hot carriers are shuttled into the underlying graphene which generates a photocurrent. The symmetry of the gold

structures is crucial in this application, as it mitigates phonon scattering, which impedes electron transport. In work by Fang et al., polarization dependent photocurrent was demonstrated using dimer and heptamer gold structures on graphene (**Figure 4.5a, b**). Similar work exploiting surface plasmon resonance was demonstrated by Etchermeyer and coworkers who showed significant polarization-dependent enhancement of photocurrent with simple patterned gold traces (**Figure 4.5c, d**).[66] Radially symmetric structures, such as gold bow-tie antennas fabricated by nanosphere lithography fabricated by Chen and coworkers,[64] have been used to enhance light absorption in the NIR and enhanced photoresponse (**Figure 4.5e**, **f**). The strong wavelength dependence of surface plasmon resonance on geometry allows researchers to lithographically adjust parameters, such as the spacing of nanodisks by Liu and coworkers (**Figure 4.5g**), and subsequently control the wavelength of light absorbed (**Figure 4.5h**).[3] Nam and coworkers have exploited buckling as a method to tune the dispersion and sensitivity of nanoisland-graphene photodetectors.[69] In all of these cases, the graphene plays a crucial role in electronic transport while the metal nanostructures aid in enhancing light absorption and subsequent photocarrier generation

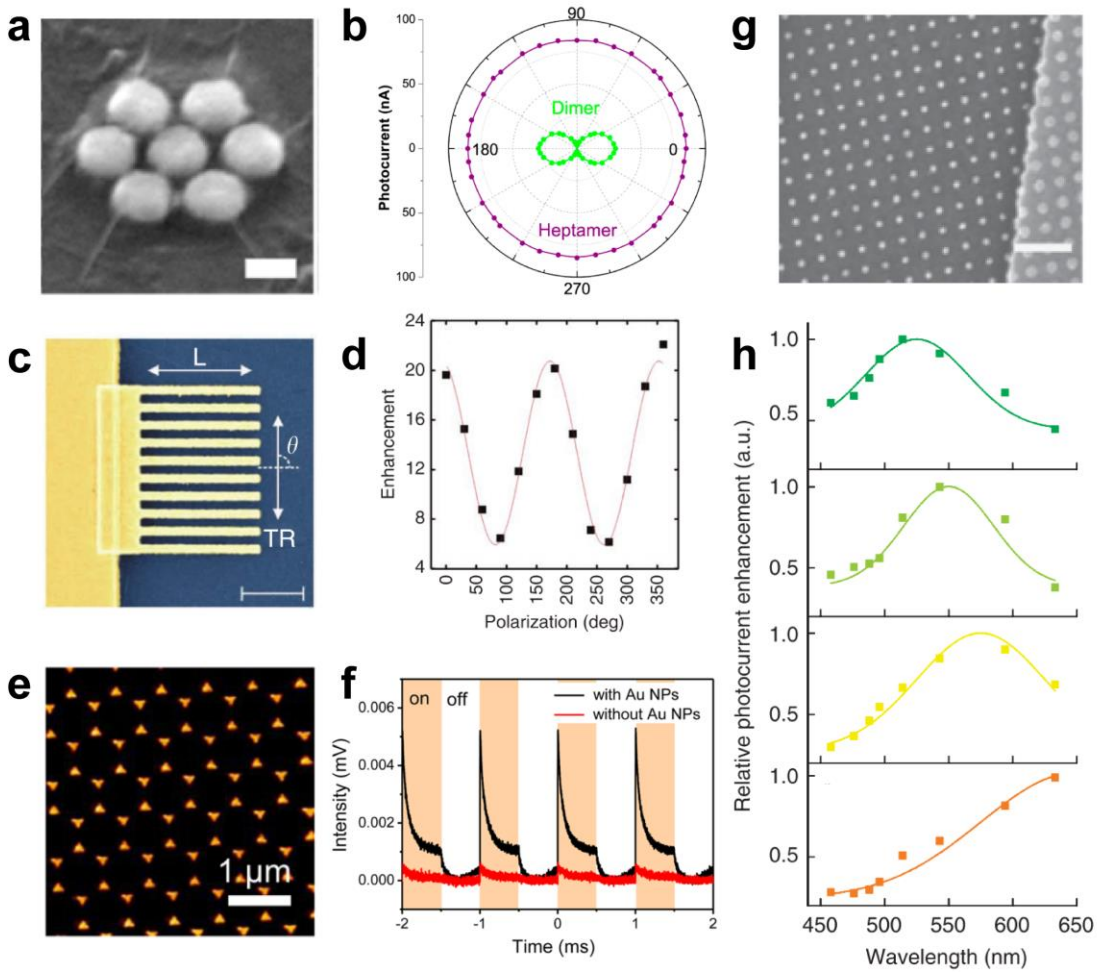

Figure 4.5. Applications for metal nanoisland-graphene composites in energy storage and transport. (a) An SEM micrograph shows gold-graphene sandwiches used for polarization-dependent photocurrent generation (scale bar 40 nm). (b) The photocurrent of graphene is controlled using the geometry of the gold nanoparticle patterns and polarization is depicted. (a) and (b) reprinted with permission from reference [28]. Copyright © 2012, American Chemical Society. (c) SEM micrographs of lithographically patterned gold nanowires (AuNW) on graphene are shown (scale bar 1μm). (d) The polarization dependent plasmon enhancement of photocurrent in graphene due to AuNWs is shown. (c) and (d) reprinted with permission from reference [66]. Copyright © 2011, Nature Publishing Group. (e) Nanosphere lithography has been used to fabricate gold bow-tie antennae on graphene (AuBT-Gr) as shown by SEM micrographs. (f) AuBT-Gr substrates have exhibited a highly sensitive time response for photocurrent as shown in (f), which shows great promise in photodetector applications. (e) and (f) reprinted with permission from reference [64]. Copyright © 2017, American Chemical Society. (g) SEM micrographs show cubic lattices of gold nanoislands can patterned on graphene with superlative control of spacing (scale bar 400 nm). (h) Control of the spacing in gold nanoparticle patterns allows for the tuning of photocurrent enhancement over a wide variety of wavelengths, as depicted by the absorption spectra in (h). (g) and (h) reprinted with permission from reference [3]. Copyright © 2011, Nature Publishing Group. The nanoparticle spacing in (h) is 18 nm (green), 50 nm (orange), 100 nm (yellow) and 400 nm (red).

4.6 Optical Applications

The usage of graphene in optical applications for metal nanoisland-graphene composites has varied from substrate to functional material. Fang and coworkers have used precisely patterned gold nanostructures on graphene (**Figure 4.6a**) for optically doped p-n junctions, where the spacing of particles determines both the wavelength of light absorbed and nature of the photocarrier injected into the underlying graphene.[27] The result is a composite material that exhibits changing semiconducting behavior based on the wavelength of illuminating light (**Figure 4.6b**). Interestingly, the graphene assumes a role of semiconductor and substrate, analogous to silicon in traditional p-n junctions. Another optical application that has seen considerable attention is the use of metal nanoisland-graphene composites as substrates for surface-enhanced Raman scattering (SERS).[5,70,71,26,72,73,74] The role of graphene in the majority of these applications is substrate, allowing easy transfer onto arbitrary substrates for specific applications such as optical strain sensing using SERS which was accomplished by Marin and coworkers using silver nanoislands supported by graphene (**Figure 4.6c, d**).[6] The work by our group also expanded upon the role of graphene, exploiting its electrical conductivity for the actuation of musculoskeletal cells (**Figure 4.6e**, **f**). This permitted the use of silver nanoislands for simultaneous electrical stimulation and optical detection (**Figure 4.6g**) of musculoskeletal contractions, which diversifies the use of the composite by providing orthogonal modes of interrogation and sensing.

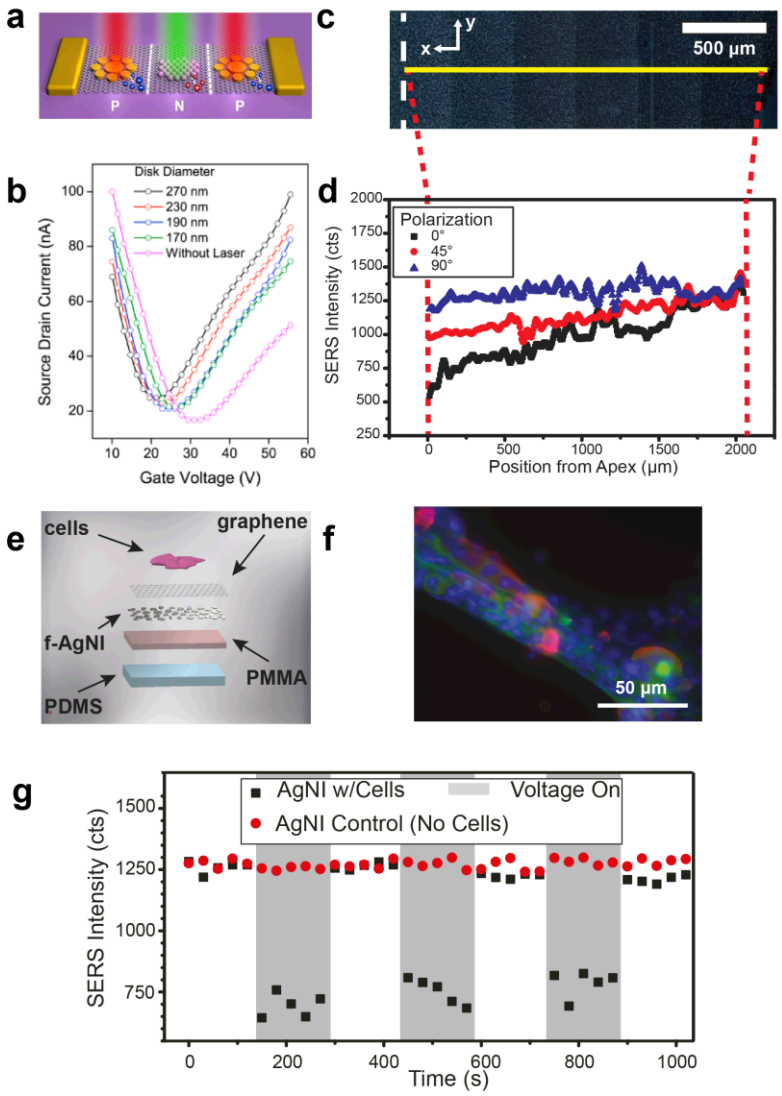

Figure 4.6. Optical applications of metal nanoisland-graphene composites. (a) Use of the composition and geometric pattern of metal to selectively dope the underlying graphene with incident light using localized surface plasmons. Further modification of individual nanoparticle geometries allows additional control over the electron transport properties (b). (a) and (b) reprinted with permission from reference [27]. Copyright © 2012, American Chemical Society. Metal nanoislands on graphene have been used extensively as surface-enhanced Raman scattering (SERS) substrates with numerous applications such as structural strain mapping and time-dependent biological strain detection (c-g). (c-g) reprinted and adapted with permission from reference [6] and the Royal Society of Chemistry. A silver nanoisland on graphene substrate on bent glass is depicted (c) with the SERS mapped area marked by the narrow yellow box and the apex of the bent glass marked by the white dashed line. The strain gradient of the bent glass is detectable by SERS intensity attenuation (d), which results from nanoislands being pulled apart; polarization angle provides additional data on the direction of strain. Silver nanoisland on graphene substrates have been used for the simultaneous stimulation and detection of musculoskeletal cell (C2C12 myoblast) contractions through SERS (e). A fluorescence image of C2C12 cells on the silver nanoisland substrate is depicted (f) with nuclei (blue), actin (green), and myosin heavy chain (red) shown. Cell contractions were stimulated by applying a voltage across the conductive silver nanoisland substrate and detected using attenuations in the SERS signal (g)

4.7 Conclusions

We described the synthesis, properties, and applications of metallic nanoislands supported by graphene. The unique properties of such a metamaterial have bolstered application-intensive work in the development of transducers, sensors, energy-transport devices, catalysts, and wearable devices for health monitoring. Despite the fervor for the utility of metal nanoisland-graphene composites, the numerous phenomena that give rise to this multifunctionality need to be uncoupled and understood in isolated studies in order to effectively engineer future applications. The specific ways in which fabrication methods (such as CVD and lithography) affect morphology and functionality need to be meticulously investigated to enhance the reliability of low strain regime sensing devices. Thin-film science has received accelerated inspiration from versatility of graphene as a composite with metal. Moreover, this work has stimulated new applications to enhance their modalities, sensitivities, and range of reach in their utility.

Acknowledgements

This work was supported by the National Institutes of Health Director's New Innovator Award, grant 1DP2EB022358-01 to D. J. L., and by a Diversity Supplement (for B. C. M.) under the same award number.

Chapter 4, in part, is currently being prepared for submission for publication of the material by Brandon C. Marin, Julian Ramirez, Eden Aklile, and Darren J. Lipomi. The dissertation author was the primary investigator and author of this material.

References

(1) Choi, S. M.; Jhi, S. H.; Son, Y. W. Controlling Energy Gap of Bilayer Graphene by Strain. *Nano Lett.* 2010, *10* (9), 3486–3489.

(2) Xu, C.; Wang, X.; Zhu, J. Graphene−Metal Particle Nanocomposites. *J. Phys. Chem. C* 2008, *112* (50), 19841–19845.

(3) Liu, Y.; Cheng, R.; Liao, L.; Zhou, H.; Bai, J.; Liu, G.; Liu, L.; Huang, Y.; Duan, X. Plasmon Resonance Enhanced Multicolour Photodetection by Graphene. *Nat. Commun.* 2011, *2*, 579.

(4) Kang, P.; Wang, M. C.; Knapp, P. M.; Nam, S. W. Photodetectors: Crumpled Graphene Photodetector with Enhanced, Strain-Tunable, and Wavelength-Selective Photoresponsivity. *Adv. Mater.* 2016, *28* (23), 4565.

(5) Zaretski, A. V.; Root, S. E.; Savchenko, A.; Molokanova, E.; Printz, A. D.; Jibril, L.; Arya, G.; Mercola, M.; Lipomi, D. J. Metallic Nanoislands on Graphene as Highly Sensitive Transducers of Mechanical, Biological, and Optical Signals. *Nano Lett.* 2016, *16* (2), 1375–1380.

(6) Marin, B. C.; Liu, J.; Aklile, E.; Urbina, A. D.; Chiang, A. S.; Lawrence, N.; Chen, S.; Lipomi, D. J. SERS-Enhanced Piezoplasmonic Graphene Composite for Biological and Structural Strain Mapping. *Nanoscale* 2016, *9*, 1292–1298.

(7) Huang, X.; Qi, X.; Boey, F.; Zhang, H. Graphene-Based Composites. *Chem. Soc. Rev.* 2012, *41* (2), 666–686.

(8) Kamat, P. V. Graphene-Based Nanoarchitectures. Anchoring Semiconductor and Metal Nanoparticles on a Two-Dimensional Carbon Support. *J. Phys. Chem. Lett.* 2010, *1* (2), 520–527.

(9) Georgakilas, V.; Otyepka, M.; Bourlinos, A. B.; Chandra, V.; Kim, N.; Kemp, K. C.; Hobza, P.; Zboril, R.; Kim, K. S. Functionalization of Graphene: Covalent and Non-Covalent Approaches, Derivatives and Applications. *Chem. Rev.* 2012, *112* (11), 6156–6214.

(10) Reina, A.; Son, H.; Jiao, L.; Fan, B.; Dresselhaus, M. S.; Liu, Z.; Kong, J. Transferring and Identification of Single- and Few-Layer Graphene on Arbitrary Substrates. *J. Phys. Chem. C* 2008, *112* (46), 17741–17744.

(11) Bae, S.; Kim, H.; Lee, Y.; Xu, X.; Park, J.-S.; Zheng, Y.; Balakrishnan, J.; Lei, T.; Ri Kim, H.; Song, Y. Il; Kim, Y.-J.; Kim, K. S.; Özyilmaz, B.; Ahn, J.-H.; Hong, B. H.; Iijima, S. Roll-to-Roll Production of 30-Inch Graphene Films for Transparent Electrodes. *Nat. Nanotechnol.* 2010, *5* (8), 574–578.

(12) Reina, A.; Jia, X.; Ho, J.; Nezich, D.; Son, H.; Bulovic, V.; Dresselhaus, M. S.; Kong, J.; Kim, K. S. K. S.; Zhao, Y.; Jang, H.; Lee, S. Y.; Kim, J. M.; Ahn, J.-H.; Kim, P.; Choi, J.-Y.; Hong, B. H. Large-Scale Pattern Growth of Graphene Films for Stretchable Transparent Electrodes. *Nano Lett.* 2009, *9* (1), 30–35.

(13) Arco, L. G. De; Zhang, Y.; Schlenker, C. Continuous, Highly Flexible, and Transparent Graphene Films by Chemical Vapor Deposition for Organic Photovoltaics. *ACS Nano* 2010, *4* (5), 2865–2873.

(14) Park, J. S.; Maeng, W. J.; Kim, H. S.; Park, J. S. Review of Recent Developments in Amorphous Oxide Semiconductor Thin-Film Transistor Devices. *Thin Solid Films* 2012, *520* (6), 1679–1693.

(15) Liu, Y.; Dong, X.; Chen, P. Biological and Chemical Sensors Based on Graphene Materials. *Chem Soc Rev* 2012, *41* (6), 2283–2307.

(16) Hong, W.; Bai, H.; Xu, Y.; Yao, Z.; Gu, Z.; Shi, G. Preparation of Gold Nanoparticle/graphene Composites with Controlled Weight Contents and Their Application in Biosensors. *J. Phys. Chem. C* 2010, *114* (4), 1822–1826.

(17) Shin, D. H.; Lee, J. S.; Jun, J.; An, J. H.; Kim, S. G.; Cho, K. H.; Jang, J. Flower-like Palladium Nanoclusters Decorated Graphene Electrodes for Ultrasensitive and Flexible Hydrogen Gas Sensing. *Sci. Rep.* 2015, *5* (12294), 1–11.

(18) Zhou, X.; Huang, X.; Qi, X.; Wu, S.; Xue, C.; Boey, F. Y. C.; Yan, Q.; Chen, P.; Zhang, H. In Situ Synthesis of Metal Nanoparticles on Single-Layer Graphene

Oxide and Reduced Graphene Oxide Surfaces. *J. Phys. Chem. C* 2009, *113* (25), 10842–10846.

(19) Chen, X.; Wu, G.; Chen, J.; Chen, X.; Xie, Z.; Wang, X. Synthesis Of "clean" and Well-Dispersive Pd Nanoparticles with Excellent Electrocatalytic Property on Graphene Oxide. *J. Am. Chem. Soc.* 2011, *133* (11), 3693–3695.

(20) Wan, Y. C.; Teoh, H. F.; Tok, E. S.; Sow, C. H. Spontaneous Decoration of Au Nanoparticles on Micro-Patterned Reduced Graphene Oxide Shaped by Focused Laser Beam. *J. Appl. Phys.* 2015, *117* (5).

(21) Muszynski, R.; Seger, B.; Kamat, P. V. Decorating Graphene Sheets with Gold Nanoparticles Decorating Graphene Sheets with Gold Nanoparticles. *J. Phys. Chem. C* 2008, *112* (March), 5263–5266.

(22) Lee, J. W.; Hall, A. S.; Kim, J. D.; Mallouk, T. E. A Facile and Template-Free Hydrothermal Synthesis of Mn 3O 4 Nanorods on Graphene Sheets for Supercapacitor Electrodes with Long Cycle Stability. *Chem. Mater.* 2012, *24* (6), 1158–1164.

(23) An, X.; Yu, J. C.; Wang, Y.; Hu, Y.; Yu, X.; Zhang, G. WO3 Nanorods/graphene Nanocomposites for High-Efficiency Visible-Light-Driven Photocatalysis and NO2 Gas Sensing. *J. Mater. Chem.* 2012, *22* (17), 8525.

(24) Rafiee, J.; Mi, X.; Gullapalli, H.; Thomas, A. V.; Yavari, F.; Shi, Y.; Ajayan, P. M.; Koratkar, N. a. Wetting Transparency of Graphene. *Nat. Mater.* 2012, *11* (3), 217–222.

(25) Chae, S.; Jang, S.; Choi, W. J.; Kim, Y. S.; Chang, H.; Lee, T. Il; Lee, J.-O. Lattice Transparency of Graphene. *Nano Lett.* 2017, acs.nanolett.6b04989.

(26) Xiang, Q.; Zhu, X.; Chen, Y.; Duan, H. Surface Enhanced Raman Scattering of Gold Nanoparticles Supported on Copper Foil with Graphene as a Nanometer Gap. *Nanotechnology* 2016, *27* (7), 75201.

(27) Fang, Z.; Wang, Y.; Liu, Z.; Schlather, A.; Ajayan, P. M.; Koppens, F. H. L.; Nordlander, P.; Halas, N. J. Plasmon-Induced Doping of Graphene. *ACS Nano* 2012, *6* (11), 10222–10228.

(28) Fang, Z.; Liu, Z.; Wang, Y.; Ajayan, P. M.; Nordlander, P.; Halas, N. J. Graphene-Antenna Sandwich Photodetector. *Nano Lett.* 2012, *12*, 3808–3813.

(29) Ghosh, S. K.; Pal, T. Interparticle Coupling Effect on the Surface Plasmon Resonance of Gold Nanoparticles: From Theory to Applications. *Chem. Rev.* 2007, *107* (11), 4797–4862.

(30) Fromm, D. P.; Sundaramurthy, A.; James Schuck, P.; Kino, G.; Moerner, W. E. Gap-Dependent Optical Coupling of Single "bowtie" nanoantennas Resonant in the Visible. *Nano Lett.* 2004, *4* (5), 957–961.

(31) Scholl, J. A.; García-Etxarri, A.; Koh, A. L.; Dionne, J. A. Observation of Quantum Tunneling between Two Plasmonic Nanoparticles. *Nano Lett.* 2013, *13* (2), 564–569.

(32) Laughlin, R. B. Quantized Hall Conductivity in Two Dimensions. *Phys. Rev. B* 1981, *23* (10), 5632–5633.

(33) Yi, J.; Kim, S. H.; Lee, W. W.; Kwon, S. S.; Nam, S. W.; Park, W. Il. Graphene Meshes Decorated with Palladium Nanoparticles for Hydrogen Detection. *J. Phys. D. Appl. Phys.* 2015, *48* (47), 475103.

(34) Wu, W.; Liu, Z.; Jauregui, L. A.; Yu, Q.; Pillai, R.; Cao, H.; Bao, J.; Chen, Y. P.; Pei, S. S. Wafer-Scale Synthesis of Graphene by Chemical Vapor Deposition and Its Application in Hydrogen Sensing. *Sensors Actuators, B Chem.* 2010, *150* (1), 296–300.

(35) Yi, J.; Lee, J. M.; Park, W. Il. Vertically Aligned ZnO Nanorods and Graphene Hybrid Architectures for High-Sensitive Flexible Gas Sensors. *Sensors Actuators, B Chem.* 2011, *155* (1), 264–269.

(36) Chung, M. G.; Kim, D. H.; Seo, D. K.; Kim, T.; Im, H. U.; Lee, H. M.; Yoo, J. B.; Hong, S. H.; Kang, T. J.; Kim, Y. H. Flexible Hydrogen Sensors Using Graphene with Palladium Nanoparticle Decoration. *Sensors Actuators, B Chem.* 2012, *169* (13382), 387–392.

(37) Zhangyuan Zhanga, Xuming Zoua, Lei Xua, Lei Liao*a, Wei Liua, Johnny Hob, Xiangheng Xiao*a, Changzhong Jianga, J. L. Hydrogen Gas Sensor Based on Metal Oxide Nanoparticles Decorated Graphene Transistor. *Nanoscale* 2010, *4* (8), 1166–1169.

(38) Navalon, S.; Dhakshinamoorthy, A.; Alvaro, M.; Garcia, H. Metal Nanoparticles Supported on Two-Dimensional Graphenes as Heterogeneous Catalysts. *Coord. Chem. Rev.* 2016, *312*, 99–148.

(39) Hang, L.; Zhao, Y.; Zhang, H.; Liu, G.; Cai, W.; Li, Y.; Qu, L. Copper Nanoparticle@graphene Composite Arrays and Their Enhanced Catalytic Performance. *Acta Mater.* 2016, *105*, 59–67.

(40) Julkapli, N. M.; Bagheri, S. Graphene Supported Heterogeneous Catalysts: An Overview. *Int. J. Hydrogen Energy* 2015, *40* (2), 948–979.

(41) He, H.; Gao, C. Graphene Nanosheets Decorated with Pd, Pt, Au, and Ag Nanoparticles: Synthesis, Characterization, and Catalysis Applications. *Sci. China Chem.* 2011, *54* (2), 397–404.

(42) Shang, L.; Bian, T.; Zhang, B.; Zhang, D.; Wu, L. Z.; Tung, C. H.; Yin, Y.; Zhang, T. Graphene-Supported Ultrafine Metal Nanoparticles Encapsulated by Mesoporous Silica: Robust Catalysts for Oxidation and Reduction Reactions. *Angew. Chemie - Int. Ed.* 2014, *53* (1), 250–254.

(43) Huang, C.; Li, C.; Shi, G. Graphene Based Catalysts. *Energy Environ. Sci.* 2012, *5* (10), 8848.

(44) Yan, C.; Wang, J.; Kang, W.; Cui, M.; Wang, X.; Foo, C. Y.; Chee, K. J.; Lee, P. S. Highly Stretchable Piezoresistive Graphene-Nanocellulose Nanopaper for Strain Sensors. *Adv. Mater.* 2014, *26* (13), 2022–2027.

(45) Kumar, M.; Bhaskaran, H. Ultrasensitive Room-Temperature Piezoresistive Transduction in Graphene-Based Nanoelectromechanical Systems. *Nano Lett.* 2015, *15* (4), 2562–2567.

(46) Tsui, M.; Islam, M. F. Creep- and Fatigue-Resistant, Rapid Piezoresistive Responses of Elastomeric Graphene-Coated Carbon Nanotube Aerogels over Wide Pressure Range. *Nanoscale* 2016, 1128–1135.

(47) Li, M.; Tang, H. X.; Roukes, M. L. Ultra-Sensitive NEMS-Based Cantilevers for Sensing, Scanned Probe and Very High-Frequency Applications. *Nat. Nanotechnol.* 2007, *2* (2), 114–120.

(48) Smith, A. D.; Niklaus, F.; Paussa, A.; Schroder, S.; Fischer, A. C.; Sterner, M.; Wagner, S.; Vaziri, S.; Forsberg, F.; Esseni, D.; Ostling, M.; Lemme, M. C. Piezoresistive Properties of Suspended Graphene Membranes under Uniaxial and Biaxial Strain in Nanoelectromechanical Pressure Sensors. *ACS Nano* 2016, *10* (11), 9879–9886.

(49) Kim, Y.; Lee, J.; Yeom, M. S.; Shin, J. W.; Kim, H.; Cui, Y.; Kysar, J. W.; Hone, J.; Jung, Y.; Jeon, S.; Han, S. M. Strengthening Effect of Single-Atomic-Layer Graphene in Metal-Graphene Nanolayered Composites. *Nat. Commun.* 2013, *4*, 2114.

(50) Yi, L.; Jiao, W.; Wu, K.; Qian, L.; Yu, X.; Xia, Q.; Mao, K.; Yuan, S.; Wang, S.; Jiang, Y. Nanoparticle Monolayer-Based Flexible Strain Gauge with Ultrafast Dynamic Response for Acoustic Vibration Detection. *Nano Res.* 2015, *8* (9), 2978–2987.

(51) Chen, S.; Wei, Y.; Yuan, X.; Lin, Y.; Liu, L. A Highly Stretchable Strain Sensor Based on a Graphene/silver Nanoparticle Synergic Conductive Network and a Sandwich Structure. *J. Mater. Chem. C* 2016, *4*, 4304–4311.

(52) Marin, B. C.; Root, S. E.; Urbina, A. D.; Aklile, E.; Miller, R.; Zaretski, A. V.; Lipomi, D. J. Graphene–Metal Composite Sensors with Near-Zero Temperature Coefficient of Resistance. *ACS Omega* 2017, *2* (2), 626–630.

(53) Sun, P.; Zhu, M.; Wang, K.; Zhong, M.; Wei, J.; Wu, D.; Zhu, H. Small Temperature Coefficient of Resistivity of Graphene/graphene Oxide Hybrid Membranes. *ACS Appl. Mater. Interfaces* 2013, *5* (19), 9563–9571.

(54) Liang, Y.; Wang, H.; Zhou, J.; Li, Y.; Wang, J.; Regier, T.; Dai, H. Covalent Hybrid of Spinel Manganese-Cobalt Oxide and Graphene as Advanced Oxygen Reduction Electrocatalysts. *J. Am. Chem. Soc.* 2012, *134* (7), 3517–3523.

(55) Qian, Y.; Wang, C.; Le, Z.-G. Decorating Graphene Sheets with Pt Nanoparticles Using Sodium Citrate as Reductant. *Appl. Surf. Sci.* 2011, *257* (24), 10758–10762.

(56) Li, Y.; Gao, W.; Ci, L.; Wang, C.; Ajayan, P. M. Catalytic Performance of Pt Nanoparticles on Reduced Graphene Oxide for Methanol Electro-Oxidation. *Carbon N. Y.* 2010, *48* (4), 1124–1130.

(57) Liang, Y.; Li, Y.; Wang, H.; Zhou, J.; Wang, J.; Regier, T.; Dai, H. Co3O4 Nanocrystals on Graphene as a Synergistic Catalyst for Oxygen Reduction Reaction. *Nat. Mater.* 2011, *10* (10), 780–786.

(58) Wu, Z. S.; Sun, Y.; Tan, Y. Z.; Yang, S.; Feng, X.; Mullen, K. Three-Dimensional Graphene-Based Macro- and Mesoporous Frameworks for High-Performance Electrochemical Capacitive Energy Storage. *J. Am. Chem. Soc.* 2012, *134* (48), 19532–19535.

(59) Wang, H.; Liang, Y.; Li, Y.; Dai, H. Co1-xS-Graphene Hybrid: A High-Performance Metal Chalcogenide Electrocatalyst for Oxygen Reduction. *Angew. Chemie - Int. Ed.* 2011, *50* (46), 10969–10972.

(60) Jiang, M.; He, H.; Huang, C.; Liu, B.; Yi, W.-J.; Chao, Z.-S. α-MnO2 Nanowires/Graphene Composites with High Electrocatalytic Activity for Mg-Air Fuel Cell. *Electrochim. Acta* 2016, *219*, 492–501.

(61) Liu, M.; Zhang, R.; Chen, W. Graphene-Supported Nanoelectrocatalysts for Fuel Cells: Synthesis, Properties, and Applications. *Chem. Rev.* 2014, *114* (10), 5117–5160.

(62) Kim, J.; Byun, S.; Smith, A. J.; Yu, J.; Huang, J. Enhanced Electrocatalytic Properties of Transition Metal Dichalcogenides Sheets by Spontaneous Gold Nanoparticle Decoration. *J. Phys. Chem. Lett.* 2013, *4*.

(63) Dong, L.; Gari, R. R. S.; Li, Z.; Craig, M. M.; Hou, S. Graphene-Supported Platinum and Platinum-Ruthenium Nanoparticles with High Electrocatalytic Activity for Methanol and Ethanol Oxidation. *Carbon N. Y.* 2010, *48* (3), 781–787.

(64) Chen, Z.; Li, X.; Wang, J.; Tao, L.; Long, M.; Liang, S.-J.; Ang, L. K.; Shu, C.; Tsang, H. K.; Xu, J.-B. Synergistic Effects of Plasmonics and Electron Trapping in Graphene Short-Wave Infrared Photodetectors with Ultrahigh Responsivity. *ACS Nano* 2017, acsnano.6b06172.

(65) Echtermeyer, T. J.; Milana, S.; Sassi, U.; Eiden, A.; Wu, M.; Lidorikis, E.; Ferrari, A. C. Surface Plasmon Polariton Graphene Photodetectors. *Nano Lett.* 2016, *16* (1), 8–20.

(66) Echtermeyer, T. J.; Britnell, L.; Jasnos, P. K.; Lombardo, A.; Gorbachev, R. V.; Grigorenko, A. N.; Geim, A. K.; Ferrari, A. C.; Novoselov, K. S. Strong Plasmonic Enhancement of Photovoltage in Graphene. *Nat. Commun.* 2011, *2*, 458.

(67) Liu, Y. L.; Yu, C. C.; Lin, K. Te; Yang, T. C.; Wang, E. Y.; Chen, H. L.; Chen, L. C.; Chen, K. H. Transparent, Broadband, Flexible, and Bifacial-Operable Photodetectors Containing a Large-Area Graphene-Gold Oxide Heterojunction. *ACS Nano* 2015, *9* (5), 5093–5103.

(68) Maiti, R.; Sinha, T. K.; Mukherjee, S.; Adhikari, B.; Ray, S. K. Enhanced and Selective Photodetection Using Graphene-Stabilized Hybrid Plasmonic Silver Nanoparticles. *Plasmonics* 2016, *11* (5), 1297–1304.

(69) Kim, M.; Kang, P.; Leem, J.; Nam, S. A Stretchable Crumpled Graphene Photodetector with Plasmonically Enhanced Photoresponsivity. *Nanoscale* 2017, 23–27.

(70) Nien, L.-W.; Chien, M.-H.; Chao, B.-K.; Chen, M.-J.; Li, J.-H.; Hsueh, C.-H. 3D Nanostructures of Silver Nanoparticle-Decorated Suspended Graphene for SERS Detection. *J. Phys. Chem. C* 2016, acs.jpcc.5b11940.

(71) Leem, J.; Wang, M. C.; Kang, P.; Nam, S. Mechanically Self-Assembled, Three-Dimensional Graphene-Gold Hybrid Nanostructures for Advanced Nanoplasmonic Sensors. *Nano Lett.* 2015, *15* (11), 7684–7690.

(72) Khalil, I.; Julkapli, N. M.; Yehye, W. A.; Basirun, W. J.; Bhargava, S. K. Graphene-Gold Nanoparticles Hybrid-Synthesis, Functionalization, and

Application in a Electrochemical and Surface-Enhanced Raman Scattering Biosensor. *Materials (Basel).* 2016, *9* (6).

(73) Hu, W.; Huang, Z.; Zhou, Y.; Cai, W.; Kang, J. Enhanced Raman Scattering of Graphene on Ag Nanoislands. *Sci. China Physics, Mech. Astron.* 2014, *57* (11), 2021–2023.

(74) Yang, C.; Zhang, C.; Huo, Y.; Jiang, S.; Qiu, H.; Xu, Y.; Li, X.; Man, B. Shell-Isolated graphene@Cu Nanoparticles on graphene@Cu Substrates for the Application in SERS. *Carbon N. Y.* 2016, *98*, 526–533.

Chapter 5

SERS-Enhanced Piezoplasmonic Graphene Composite for Biological and Structural Strain Mapping

Brandon C. Marin,[a] Justin Liu,[a] Eden Aklile,[a] Armando D. Urbina,[a] Andrew S-C. Chiang,[a] Natalie Lawrence,[a] Shaochen Chen,[a] and Darren J. Lipomi[a]

[a]*NanoEngineering Department, University of California, San Diego.*

9500 Gilman Drive MC 0448, La Jolla, CA 92093-0448

Abstract

Thin-film optical strain sensors have the ability to map small deformations with spatial and temporal resolution and do not require electrical interrogation. This paper describes the use of graphene decorated with metallic nanoislands for sensing of tensile deformations of less than 0.04% with a resolution of less than 0.002%. The nanoisland-graphene composite films contain gaps between the nanoislands, which when functionalized with benzenethiolate behave as hot spots for surface-enhanced Raman scattering (SERS). Mechanical strain increases the sizes of the gaps; this increase attenuates the electric field, and thus attenuates the SERS signal. This compounded, SERS-enhanced “piezoplasmonic" effect can be quantified using a plasmonic gauge factor, and is among the most sensitive mechanical sensors of any type. Since the graphene-nanoisland films are both conductive and optically active, they permit simultaneous electrical stimulation of myoblast cells and optical detection of the strains produced by the cellular contractions.

5.1 Introduction

Piezoresistive sensors undergo a reversible change in resistance with mechanical strain and are ubiquitous in microelectromechanical systems (MEMS), wearable sensors, and structural health monitors.[1,2,3] Most conductive objects exhibit increased electrical resistance (R) along a strained axis simply because stretching increases the length and reduces the cross sectional area normal to the strain. The sensitivity of this modality—expressed as the gauge factor ($GF = \Delta R/\Delta\varepsilon$, where ε is the engineering strain)—for conductors with uniform composition is limited at small strains to $GF = 1 + 2\nu$, where ν

is the Poisson ratio.[4] Structured materials, such as thin films that rely in part on controlled fracture or quantum tunneling to mediate the resistivity, can exhibit much higher sensitivity.[5,6,7,8] Resistive sensors, however, require electrical contacts for interrogation, and can thus interfere with measurements of biophysical events that may be sensitive to small electrical potentials (e.g., cell contractions).[9] In contrast, optical modes of sensing provide a route of interrogation that is in principal orthogonal to electrophysiological signals, and can do so without physical contact. The use of metallic nanoparticles on a deformable substrate offers the potential for high sensitivity for detection based on optics because of localized surface plasmons.[10,11] These surface plasmons, in turn, greatly amplify near-field signals, especially between adjacent nanoparticles that are separated by small dimensions (≤10 nm).

Our group has recently demonstrated the ability to form metallic nanoislands by physical vapor deposition on graphene using low nominal thicknesses of deposition. The morphology of the nanoisland films was controlled by exploiting the wetting transparency of graphene. That is, the surface energy of the substrate supporting the graphene influenced the morphology of the nanoisland films, and thus a wide range of morphologies could be produced, from isolated islands to percolated networks. These graphene-nanoisland composite films exhibited tunable morphologies and small gaps between adjacent nanoislands, and could be transferred to flexible substrates. In one example, we detected the contractions of mammalian cardiomyocytes using the piezoresistance of the composite films.[12] In this paper, we show that the nanoscale spacing between metallic islands permit a form of mechanical sensing based on optics. In particular, mechanical force produced by cells or other objects change the spacing

between metallic nanoislands and thus modulate the electric field between them through plasmonic coupling. This effect can be augmented by adding an adsorbant to the metallic nanoislands, and measuring the surface-enhanced Raman scattering (SERS) signal of the adsorbant as a function of strain (**Figure 5.1**). This method of sensing—a SERS-enhanced piezoplasmonic effect—provides a two-component enhancement of the signal produced by mechanical strain: first, by the strong dependence of the SERS signal on electric field, and second, by the strong dependence of the electric field on the distance of separation between the particles. The SERS-enhanced piezoplasmonic effect in principle would permit mechanical sensing that is significantly more sensitive than piezoresistive sensors.

Previous work in the area of strain-tunable optical devices, which have exploited far-field phenomena, include strain-tunable filters,[13] reflectors,[14] and gratings,[15] and dynamic color tuning.[16] Work involving near-field phenomena has included strain-tunable surface plasmon resonance,[17,18,19,20] fano resonance,[21] and strain-controlled SERS activity.[10,11,22] Although this work encompasses a wide breadth of interesting applications, strain-sensitive optical phenomena have not been used for the sensing of microscale mechanical deformations in biological systems. The use of metallic nanoislands on graphene offers a unique platform to address this challenge. These composite films permit electrical stimulation of myoblast cells with simultaneous non-contact detection of the strain produced by the cells, using a SERS-enhanced "piezoplasmonic" effect.

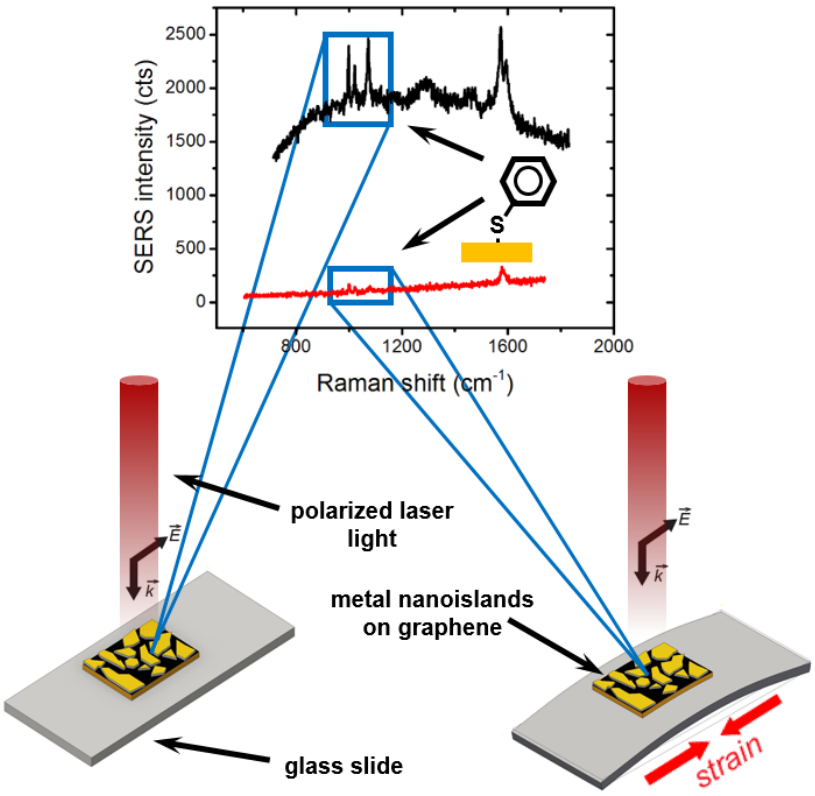

Figure 5.1. Schematic diagram for strain sensing using metallic nanoislands on graphene. The metallic nanoislands have a self-assembled monolayer of benzenethiolate chemisorbed on the surface, which produced the SERS spectra shown in the diagram. The peaks in the SERS spectra corresponding to the vibrational modes of the benzenethiolate are highlighted in blue boxes. The polarization of incident laser light was in the direction of the long axis of the substrates. The substrate on the right was subjected to a bending strain, with the graphene/nanoisland film on the top surface of the bend. The tensile strain produced by bending increased the distance between the nanoislands; increased separation decreased the plasmonic coupling and thus attenuated the SERS signal.

5.2 Methods

5.2.1 Graphene Synthesis

Graphene was synthesized using an MTI OTF-1200X-HVC-UL quartz tube furnace. Briefly, electropolished copper foil was annealed in the tube furnace at 1050 °C, 1 atm, for 30 min under flow of ultra-high purity (UHP) argon (700 SCCM) and hydrogen (60 SCCM). Following this step, graphene growth was initiated by flowing

methane (0.3 SCCM), UHP argon (700 SCCM), and hydrogen (60 SCCM) into the furnace for 40 min. The methane flow was increased to 0.7 SCCM for an additional 20 min while keeping UHP argon and hydrogen flow rates constant. Hydrogen and methane flows were then terminated, which ends the synthesis. The furnace was then slow cooled to ambient temperature under UHP argon flow only.

5.2.2 Metal Nanoisland Fabrication

Metal nanoislands were fabricated by physical vapor deposition using an AJA International thermal evaporator (Orion-class). Approximately 6 nm of gold or silver was deposited onto graphene supported on copper foil at a rate of 0.05 Å/s. Chamber pressure during deposition was 2.0 x 10^{-7} torr. The product of this procedure was a copper foil substrate bearing a layer of graphene, and decorated with metallic nanoislands (NI/Gr/Cu). Thin films of gold and silver (100 nm) were prepared by thermal evaporation at a rate of 1 Å/s and a chamber pressure of 2.0 x 10^{-7} torr.

5.2.3 Nanoisland Functionalization for SERS, Substrate Transfer, and Testing

Benzenethiol (Sigma-Aldrich) was used as our SERS analyte. To functionalize the metal islands, a 1 mM benzenethiol ethanolic solution was prepared and drop casted onto the nanoisland side of a NI/Gr/Cu sample. Samples were allowed to incubate for 6 hours then cleaned thoroughly with ethanol and deionized water. To transfer nanoislands onto a substrate of interest, a water transfer method was used. The graphene was essential for this method, as it provides mechanical support for ease of transferring. To summarize for polarization studies, 200 nm of 1 kDa molecular weight poly-methylmethacrylate (PMMA) was spun (4 kRPM for 60 s) onto the functionalized nanoisland side of the NI_{func}/Gr/Cu sample, adding another layer to the sample (PMMA/NI_{func}/Gr/Cu). The

backing copper foil was etched off by floating the PMMA/NI_{func}/Gr/Cu sample copper-side down on an aqueous ammonium persulfate solution (50 mg/mL). The floating island samples (now PMMA/NI_{func}/Gr) were then transferred onto a 200 μm thick glass slide for polarization studies, PMMA side up. Glass was used as a substrate to minimize the mixing of Raman signal from the substrate with the analyte (glass has a relatively low Raman signal). As a result of the substrate selection, bending strains were used to analyze the piezo response since glass cannot be effectively stretched for strain measurements. Substrates were bent and held in tension using 3D printed supports. Based on the dimensions of these supports, finite-element analysis simulations were performed to calculate the strain at the apex. The PMMA was stripped before Raman measurements to minimize signal cross talk. Stripping was done by immersion in warm acetone (40 °C) for 30 min, followed by rinsing with isopropanol and deionized water (ambient temperature).

For cell studies, floating island samples (PMMA/NI_{func}/Gr) on water were transferred onto polymethyldisiloxane (PDMS) slabs, with the graphene side up. A diagram in **Figure C5** depicts substrate orientation in detail and the transfer process. The samples (Gr/NI_{func}/PMMA/PDMS) were then washed thoroughly with DI water, then PBS buffer solution before cell seeding.

5.2.4 Electron Microscopy

An FEI Tecnai G2 Sphera running a LaB_6 filament at 200 kV was used for transmission electron (TEM) micrographs and electron diffraction. A Gatan Ultrascan 1000 UHS CCD camera running Gatan Digital Micrograph was used for image collection. TEM samples were prepared by transferring graphene-supported nanoislands (by water-transfer method) onto unsupported 200-mesh copper TEM grids. An FEI XL30

SFEG was used for scanning-electron microscopy (SEM). Images were acquired at 15 kV accelerating voltage with a 50-µm spot and a through lens-detector. SEM samples were prepared by transferring graphene-supported nanoislands (by water-transfer method) onto silicon chips. A Hitachi HD2000 was used for combination scanning-transmission electron microscopy (STEM) running a tungsten filament at 200 kV. STEM samples were prepared by transferring graphene-supported nanoislands (by water-transfer method) onto unsupported 200-mesh copper TEM grids

5.2.5 Reflectance Spectroscopy

Reflectance spectra were taken using a Perkin Elmer Lambda-1050 UV-vis-NIR spectrophotometer with a universal reflectance accessory (URA) module. The spectrometer acquired signal from 250-900 nm using a silicon detector with a tungsten (visible) and deuterium lamp (ultraviolet) as a source. A 1400 lines/mm holographic monochromator was used to grate the signal.

5.2.6 Raman Spectroscopy and Microscopy

All Raman spectra were collected on a Renishaw inVia Raman microscope. A 633 nm HeNe laser polarized by half-wave plates was used with an excitation power of ca. 1 mW. 633 nm laser light was selected due to its lower phototoxicity and higher SERS enhancement, when compared to UV-vis lasers. A 5x, 0.12 NA Leica N-Plan objective was used for both excitation and collection of Raman data. A 1800 l/mm grating was used for the dispersion of sample signal. For SERS measurements, samples were functionalized with benzenethiolate by immersion in a 1mM ethanolic solution for 6 h, followed by rigorous cleaning in IPA and DI water. Spatially static spectra, such as those used for polar plots were collected using a 1 s acquisition at 1% laser power.

Raman maps were acquired using a 3 s acquisition under 5% laser power. Map dimensions were 2100 μm × 6 μm and consisted of 1360 individual spectra. A 5-point center cumulative average was used for analysis of the SERS intensities as a function of distance from the apex. All SERS intensities for all measurements compared the intensity of the 999 cm^{-1} peak of benzenethiolate (which corresponds to vibrational mode 12 in Wilson notation).[23] This vibrational mode was particularly chosen due to the isotropic nature of its Raman tensor, which prevented any bias in polarization measurements.[24]

5.2.7 Finite-Difference Time Domain (FDTD) Simulations

2D FDTD electromagnetic simulations were performed using Lumerical FDTD solutions with a mesh size of 2Å. Palik dielectric data was used for silver and gold. Falkovsky dielectric data was used for graphene. Geometries for metal nanoislands were based on TEM images (**Figure C3**). Simulations were performed at an incident wavelength of 633 nm, the excitation wavelength of the laser used for Raman spectroscopy. The incident light was polarized and coherent.

5.2.8 Finite-Element Simulations of Glass

Autodesk Inventor was used to simulate bent glass (50.8mm x 19.05mm x 0.20mm) through finite-element analysis. The strain along the length of the slide as a function of distance from apex was calculated after applying 54 N, 124 N, and 203 N of force to the center, with the maximal strain occurring at the apex with values of 0.032, 0.074, and 0.12 percent strain, respectively. Force was applied from the bottom with the two end of the glass held by immobile contacts. Deformation analysis using FEA assumes linear, static stress that is proportional to load applied, linear material properties and neglects yielding and buckling.

5.2.9 Myoblast Cell (C2C12) Culture, Maintenance and Characterization

C3H/C2C12 murine myoblast cells were purchased from ATCC and cultured according to protocol provided by ATCC. C2C12 cells were cultured in Dulbecco's Modified Eagle Medium (DMEM, Gibco) supplemented with 10% fetal bovine serum, heat inactivated (Hyclone), and 1% penicillin/streptomycin (Gibco). Cells were maintained in a 37 °C incubator with 5% CO_2. C2C12 cells were differentiated by culturing in DMEM with 5% horse serum and 1% penicillin/streptomycin for 3 days. Cells were treated with 0.25% trypsin EDTA (Gibco) and were then seeded onto the graphene side of the silver nanoisland substrate (**Figure C5**) at a density of 3,000 cells/mm^2. Cells were cultured for at least 3 days before analysis.

Cells were fixed with 4% paraformaldehyde (PFA, Life Technologies) in phosphate buffered saline for 15 min, washed 3 times for 5 min in phosphate buffer solution (PBS, 100 mM NaCl, 8.0 pH). Cells were permeabilized using and blocked using 2% (wt/vol) bovine serum albumin and 0.1% (wt/vol) Triton-X100 (Sigma-Aldrich) in PBS for 1 h. Samples were washed 3 times in PBS for 5 minutes. Cells were counterstained with myosin heavy chain (rabbit) primary antibody (1:100, Sigma) in PBS with 2% BSA overnight. Samples were washed 3 times with PBS for 5 min and following primary incubation, they were incubated with FITC-Phallodin (1:100, Life Technologies), donkey anti-rabbit 543 (1:200, Biotium) and Hoescht 33258 for nuclei (1:2000, Invitrogen). Finally, samples were imaged at 40x using a Leica DMI6000 inverted fluorescence microscope.

For SEM micrographs, cells were fixed with 4% PFA for 15 minutes and dehydrated using a gradient of 20%, 50%, 60%, 70%, 80%, 90%, 95%, and 100% ethanol

incubations at room temperature. Samples were incubated in 20% ethanol for 20 min and subsequent dehydration steps were 5 minutes each. Samples were dried using a Touisimis Critical Point Drier and were then coated with iridium by DC sputtering. SEM micrographs were acquired using an FEI XL30 SFEG, as previously described.

For electrical cell stimulation, nanoisland samples were electrically addressed with eutectic gallium indium (EGaIn). Samples were then pulsed with 5-volts, at 2 Hz, with a square wave profile, using a Siglent SDG2042X function/arbitrary waveform generator.

5.3 Results and Discussion

In order to determine usefulness as a SERS substrate, we characterized the morphologies and optical properties of silver and gold nanoislands. The transmission electron microscope (TEM) images for gold (**Figure 5.2a**) and silver (**Figure 5.2b**) nanoislands suspended on single-layer graphene show small gaps between the nanostructures, which appear as lighter regions. These gaps are highly active for SERS, due to the strong electric fields present in plasmonic coupling of noble metal interfaces.[25,26,27] The optical response of the nanoislands lies in the visible range (**Figure 5.2c,d**). Plasmon resonance contributes to stronger absorption of light for nanoislands relative to their thin-film counterparts as compared for gold and silver in and **Figure 5.2c** and **Figure 5.2d**, respectively. This plasmon resonance and its associated electric field (***E***) are crucial to the sensitivity of an optical strain gauge. The magnitude of ***E*** in coupled plasmonic modes over small length scales is believed to vary between d^{-3} and d^{-6}, where d is the separation between plasmonic nanoparticles.[28,29] The electromagnetic SERS

effect of chemical species located in the gaps between metallic nanoparticles, in turn, varies with $\boldsymbol{E^4}$. The compounding nonlinear effects of (1) the dependence of the gap size on electric field and (2) the dependence of SERS effect on the magnitude of the electric field resulted in a piezoplasmonic effect that exhibited remarkable sensitivity in the low strain regime.

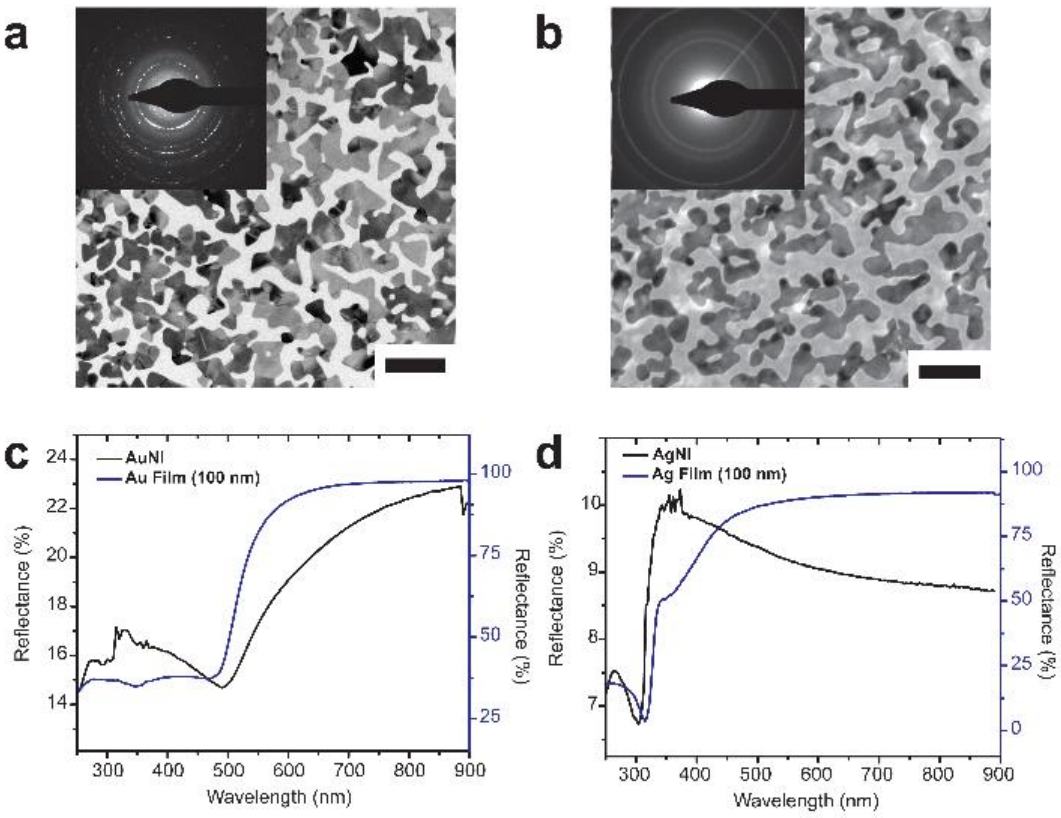

Figure 5.2. Morphology and optical spectra of nanoislands on graphene. Transmission electron micrographs (TEM) and electron diffraction patterns (insets) of gold nanoislands (AuNI, a) and silver nanoislands (AgNI, b) to provide a comparison on crystallinity. Scale bars, 100 nm. Reflectance spectra of gold (c) and silver (d) nanoislands with spectra of unstructured, continuous 100 nm metal films for comparison. The dips in reflectance of gold are lower in energy than those of silver because of unequal relativistic contractions between the two metals.

To quantify the effect of strain on the SERS intensity, we functionalized metal nanoislands on graphene films with a self-assembled monolayer (SAM) of benzenethiolate. We then transferred the films bearing nanoislands to thin (200 μm) glass slides. These slides could be deformed easily by loading them into brackets fabricated by 3D printing. The tensile strains on the top surfaces of the slides were calculated by finite-element modeling (**Figure C1**). Large bending radii produced small tensile strains. In this small-strain regime (<0.2%), the nanoislands exhibited an anisotropic response in the SERS signal based on the polarization of incident light (**Figure 5.3a**). That is, the SERS signal of the benzenthiolate SAM was diminished when light was polarized parallel to the direction of strain. This result was consistent with increased spacing between the gaps along the strained axis, i.e., that nanoislands were being pulled apart.

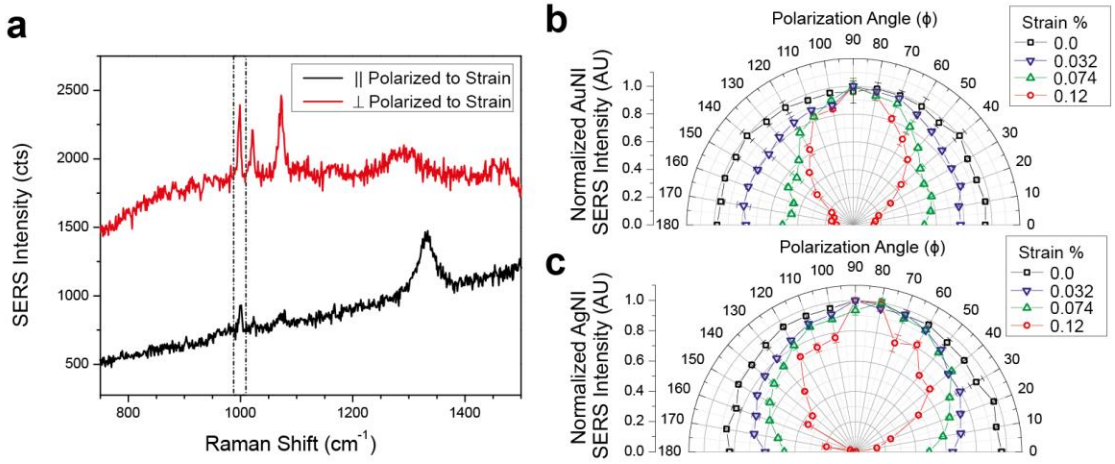

Figure 5.3. Polarization response of nanoislands under strain. (a) SERS spectra of gold nanoislands under 0.074% strain with incident laser light polarized parallel and perpendicular to strain. The peak of interest in chemisorbed benzenethiol is highlighted between the dashed lines (999 cm-1 peak). Radial plots of gold (b) and silver (c) nanoislands, which reveal the polarization response of the SERS signal with the graphene-nanoisland film under strain. The radial plots are normalized to maximum SERS intensity of the peak indicated in panel (a).

We observed that the difference between the SERS signal of a benzenethiolate SAM in response to polarization between the strained and unstrained axis increased with increasing strain. This increased anisotropy in the signal was consistent with strain-induced separation between nanoislands supporting the SAM; increased separation produced a larger contrast in SERS intensity between light polarized in the direction of strain and orthogonally (**Figure 5.3a**). (We note that the anisotropy in response to polarization was greater for silver nanoislands than it was for gold, as see in **Figure 5.3b** and **5.3c**.) Essentially, strain changes the size of gaps between nanoislands and the nature of surface plasmons confined between them. Non-linear decay of the SERS signal with respect to separation is consistent with the results of others. [29,30,31]

In analogy to the gauge factor (GF) used for piezoresistive sensors to quantify the response to strain,[4] we propose a plasmonic gauge factor ($GF_{plasmonic}$), which quantifies the SERS response of films of metallic nanoparticles to strain,

$$GF_{plasmonic} = \frac{\frac{I_{unstrained} - I_{strained}}{I_{strained}}}{\varepsilon}$$

where $I_{unstrained}$ and $I_{strained}$ are defined as the SERS intensities of unstrained and strained films, respectively, with the incident polarization held constant (in the direction of the long axis of the slide). A high sensitivity is indicated by large contrasts between $I_{strained}$ (which should decrease as nanoislands are pulled apart) and $I_{unstrained}$, which yields a high $GF_{plasmonic}$. **Figure 5.4** plots $GF_{plasmonic}$ as a function of strain for silver and gold nanoislands. Silver nanoislands demonstrated a more sensitive piezoplasmonic response based on $GF_{plasmonic}$ values, especially at the lowest strains tested (~0.03%). Compared to gold, silver has the ability to confine stronger electric fields in nanostructures.32,33 To

reinforce this observation, we performed finite-difference time domain (FDTD) simulations of gaps between silver nanoislands and gold nanoislands to determine the electric field profile at the Raman laser wavelength (633 nm). Our FDTD results (**Figure C2**) confirm that gaps between silver nanoislands have a higher magnitude of ***E*** than do gaps between gold nanoislands. A comparison of $GF_{plasmonic}$ between the responses of gold and silver nanoislands is shown in **Figure 5.4**.

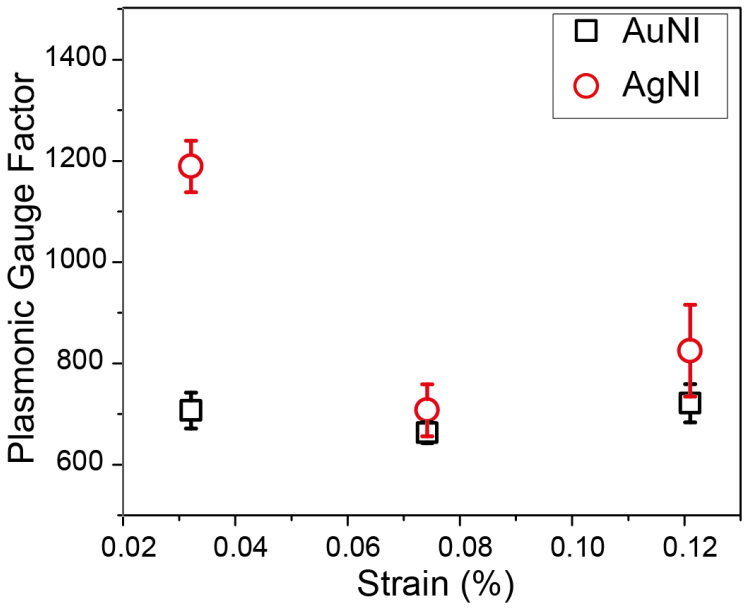

Figure 5.4. Piezoplasmonic characterization of noble metal nanoislands. Plasmonic gauge factors of gold nanoislands (AuNI) and silver nanoislands (AgNI) are plotted as a function of strain.

One of the advantages of detecting strain using a contiguous optically active film is the ability to measure gradients of deformation. To demonstrate this ability, we obtained polarization-dependent maps of the SERS intensity of a graphene/silver nanoisland film located near the apex of a rectangular glass slide under a small bending radius. The bending deformation produced a strain gradient along the long axis, with the greatest strain (0.032%) located at the apex (**Figure C1**, **Table C1**). **Figure 5.5a** shows a

bright field image comprising 12 individual micrographs of the gradient, with the apex of the bent substrate indicated by the dotted line. The dimensions of the long and narrow rectangular region were 2100 μm × 6 μm (the raw 2D spectral images are shown in **Figure C4**), which is marked by the yellow line in **Figure 5.5a**. When incident light was polarized in the direction of the strain gradient (0° with respect to the x-axis), a clear decrease in SERS signal could be detected (**Figure 5.5b**). The SERS signal was lowest at the area of highest strain (the apex). As the polarization was increased to 45° (**Figure 5.5b**), the gradient in SERS signal was diminished, as the nanoislands were separated along the long axis. With polarization 90° to the axis of the strain gradient (**Figure 5.5b**), we observed little variation in the SERS signal. According to finite-element simulations (**Table C1**), the gradient in SERS intensity in the narrow rectangular region corresponded to a total range in strain of 0.0017%.

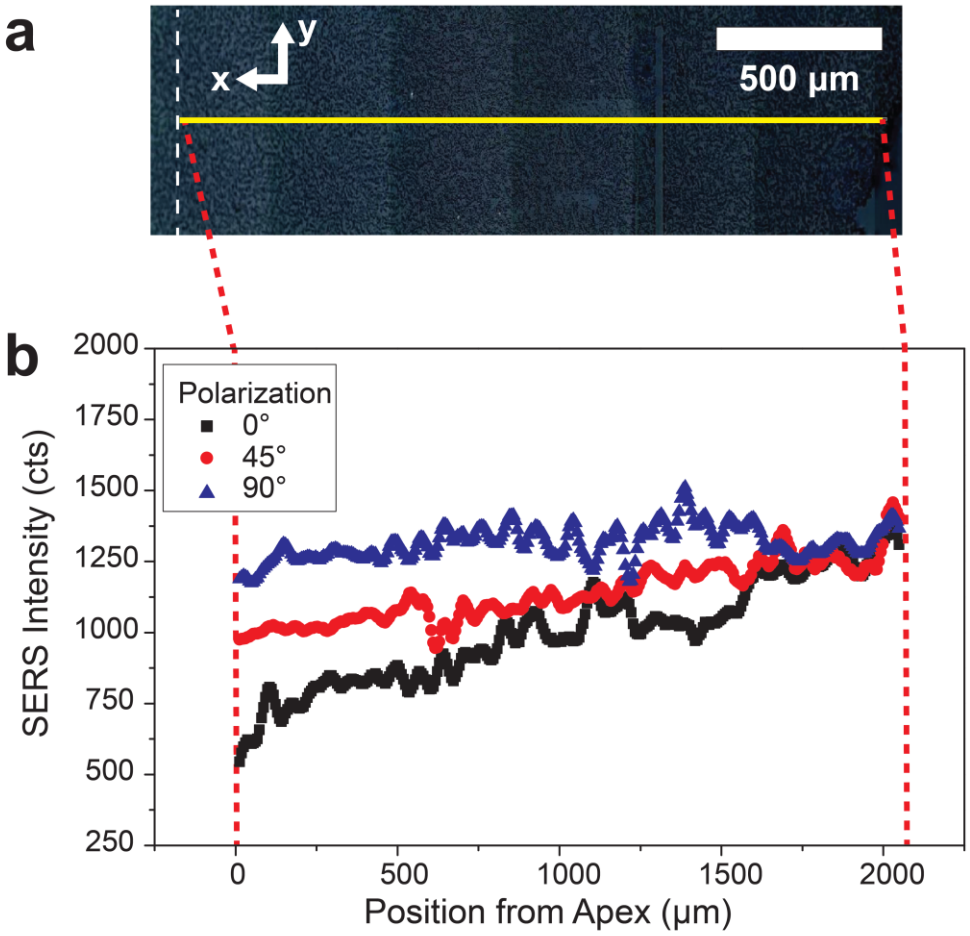

Figure 5.5. SERS mapping of strain gradients using a bent glass substrate bearing silver nanoislands on graphene. (a) Bright-field image of silver nanoislands on a bent glass substrate (scale bar, 500 µm). The yellow line near the center of the image is the selected area (2100 µm × 6 µm) that was mapped using a Raman microscope. The apex of the bent substrate is marked by the dotted white lines and has a strain of 0.032%. (b) A moving average of the SERS intensity along the x-axis in the selected area under three different polarizations (0°, 45°, and 90° in respect to the x-axis). Note that the signal decreases as the polarization aligns with the principle direction of deformation (x-direction).

Since the graphene-nanoisland films are both electrically conductive and optically active, we tested their ability to be used in an optoelectronic biosensing platform. That is, the electrical conductivity of graphene could be used for stimulation of a strain-producing biophysical event and strain-dependent SERS could be used for detection of the deformation. To test this hypothesis, we measured the SERS spectrum of the electrically induced strain response of myoblast (C2C12) cells grown on silver nanoisland substrates

to determine if the stimulated contraction could be detected optically through changes in the SERS signal. Silver nanoislands supported by graphene functionalized with benzenethiolate were transferred onto PDMS with the graphene-side up to maintain biocompatibility (**Figure C5**). The C2C12 cells were then grown, differentiated, and seeded on the substrates, which were then electrically addressed with droplets of a liquid metal, eutectic gallium-indium (EGaIn). The area on the sample from which the SERS signal was collected is indicated by the black box in **Figure 5.6a**. **Figure 5.6b** shows scanning electron microscope (SEM) images that were taken of C2C12 cells dehydrated using critical point drying (CPD) to demonstrate that the cells were interacting with the substrate. To investigate the structure of the C2C12 cells, fluorescence images of the adherent cells were taken one day after seeding. **Figure 5.6c** clearly shows the individually labeled nuclei (blue), actin (green), and myosin heavy chain (red) in the cells.

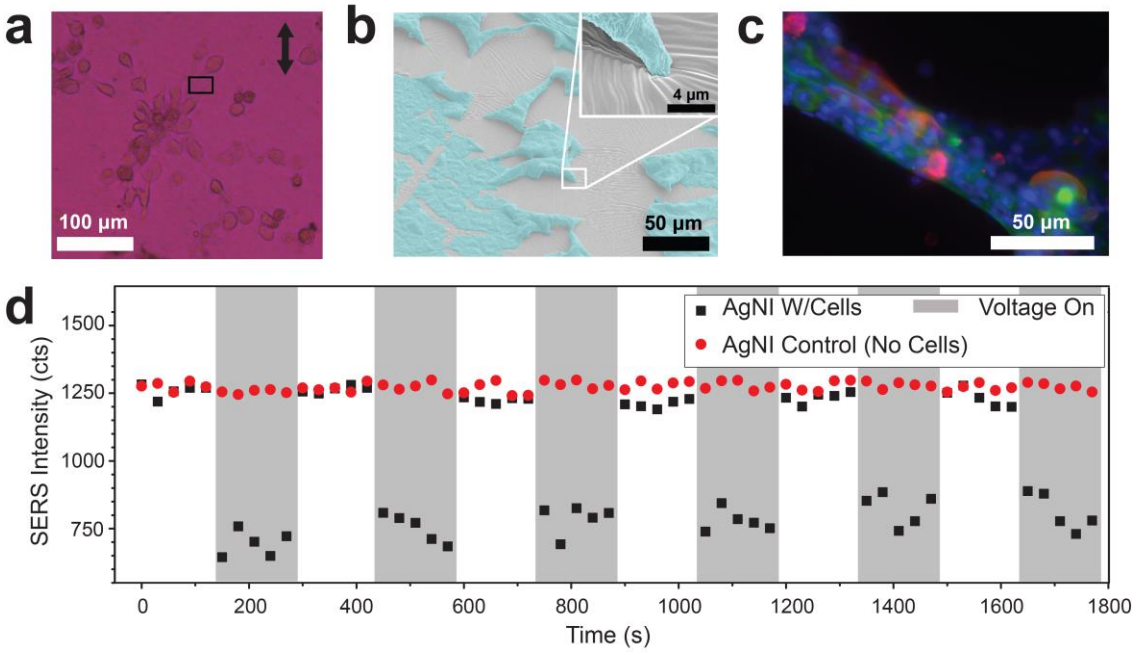

Figure 5.6. Optical detection of strain induced by electrical stimulation of C2C12 myoblast cells supported by a substrate consisting of silver nanoislands on graphene. (a) A bright-field image of C2C12 cells on the substrate, with the incident polarization of the Raman laser indicated by the black arrow. The area of illumination by the Raman laser is indicated by the black box. (b) Scanning electron micrographs of critical-point dried C2C12 cells on the substrate demonstrate the interaction of the cells with the underlying nanoislands substrate. Note the stretch marks on the substrate caused by strain. Cells were false colored blue in the micrograph. (c) A fluorescence image of C2C12 cells on the substrate with nuclei (blue), actin (green), and myosin heavy chain (red) clearly visible. (d) The SERS intensity of benzenethiolate chemisorbed to silver nanoislands in the illumination area is depicted as a function of time. The gray areas indicate time periods when the C2C12 cells were stimulated by a pulsed voltage, causing them to contract and pull silver nanoislands apart which translated to a decreased SERS signal (black squares). As a control, silver nanoislands without cells were also stimulated by pulsed voltage (red circles).

The samples were illuminated with 633 nm laser light to collect the SERS signal. Without any voltage, the SERS signal remained constant, as depicted in **Figure 5.6d**. A pulsed voltage (2 hz, 5 V square-wave) was then applied to induce the differentiated C2C12 cells to contract. The periods of time during which the voltage was applied are indicated by the gray areas in **Figure 5.6d**. A clear decrease in SERS intensity is observed under pulsed voltage, which was repeatable as indicated in **Figure 5.6d**. This decrease in intensity suggested that the separation between the silver nanoislands was

increasing due to the stress transferred to the substrate by contraction of the C2C12 cells. The area selected for illumination was a region that encompassed the border of two C2C12 cells. We hypothesized that as the cells contracted under voltage, the underlying silver nanoislands were pulled apart; this change in geometry caused a decrease in plasmonic coupling, thus leading to a decreased signal. As a control, silver nanoisland substrates without cells were pulsed under voltage to determine if the effect was based on an unknown piezoelectric effect (contraction or expansion under electrical stimulus) in the metal nanoislands. As depicted in **Figure 5.6d**, silver nanoislands without cells exhibited no change in signal when stimulated with a pulsed voltage. The SERS spectra of the substrates was dominated by the benzenethiolate signal (**Figure C6**), which suggested that the majority of the signal came from small volume confined to the gaps between the nanoislands, i.e., hotspots. Considering the myriad of organic species present in the vicinity of the nanoislands—e.g., graphene, cells, PDMS, and media solution—capable of producing unwanted SERS signals (SERS crosstalk), the high signal-to-noise ratio for benzenethiolate was gratifying. (Ordinarily, SERS crosstalk can make it difficult to extract information of interest in complex biological systems.[34,35])

5.4 Conclusions

A SERS-enhanced piezoplasmonic effect can be used to detect small strains, gradients of strain, and a non-contact method of measuring the electrically induced contractions of myoblast cells. By exploiting the fact that the electric field produced by surface plasmons between adjacent metal structures changes dramatically—coupled with the strong dependence of the SERS effect on electric field—we were able to detect strains

as low as 0.032% with a resolution of less than 0.002%. The small strain regime is well suited for a piezoplasmonic sensor, as the most significant responses occur over small length scales. Although piezoresistive sensors offer excellent response over a wide range of strains,[6,36] a piezoplasmonic sensor offers high sensitivity over small strain regimes. Moreover, metallic nanoislands on graphene offer a simple approach to fabricating SERS-based strain sensors that are easily transferrable onto to nearly any substrate. These sensors can be used to measure both the magnitude and spatial distribution of strain. In considering implementation of a technology such as this over large areas, nanoislands can be fabricated without the need for costly lithographic techniques. That is, the SERS-active substrates form automatically on graphene without the need for e-beam lithography or self-assembly. We believe, however, that the most compelling attributes of graphene-supported nanoislands as optical strain sensors is the spatial resolution (for strain mapping) and orthogonality of electrical stimulation and optical interrogation, which holds promise for high-throughput measurement of cellular electrophysiology.

Acknowledgments

This work was supported by the National Institutes of Health Director's New Innovator Award, grant 1DP2EB022358-01 to D.J.L. and by a Diversity Supplement (for B.C.M.) under the same award number. A.S-C.C. was supported by the UC LEADS program, and E.A. received partial support from the CA-NASA/UCSD Space Grant Consortium. J.L. and S.C. are supported in part by California Institute for Regenerative Medicine (RT3-07899) and National Institutes of Health (R01EB021857). This work was performed in part at the San Diego Nanotechnology Infrastructure (SDNI), a member of

the National Nanotechnology Coordinated Infrastructure, which is supported by the National Science Foundation (Grant ECCS-1542148). B.C.M. would like to acknowledge the use of the UCSD Cryo-Electron Microscopy Facility which is supported by NIH grants to Dr. Timothy S. Baker, the tireless efforts of Dr. James Bouwer, and a gift from the Agouron Institute to UCSD. The authors acknowledge Prof. Andrea R. Tao for use of her lab's Renishaw Raman Spectrometer which was purchased with a DURIP Grant (N000141310655).

Chapter 5, in full, is a reprint of the material as it appears in Nanoscale, 2017, 6, 1292-1298. The Royal Society of Chemistry, 2017. Brandon C. Marin, Justin Liu, Eden Aklile, Armando D. Urbina, Andrew S-C. Chiang, Natalie Lawrence, Shaochen Chen, and Darren J. Lipomi. The dissertation author was the primary investigator and author of this paper.

References

(1) Li, M.; Tang, H. X.; Roukes, M. L. Ultra-Sensitive NEMS-Based Cantilevers for Sensing, Scanned Probe and Very High-Frequency Applications. *Nat. Nanotechnol.* 2007, *2* (2), 114–120.

(2) Liu, X.; Mwangi, M.; Li, X.; O'Brien, M.; Whitesides, G. M. Paper-Based Piezoresistive MEMS Sensors. *Lab Chip* 2011, *11* (13), 2189.

(3) Pacelli, M.; Caldani, L.; Paradiso, R. Textile Piezoresistive Sensors for Biomechanical Variables Monitoring. *Annu. Int. Conf. IEEE Eng. Med. Biol. - Proc.* 2006, 5358–5361.

(4) Mason, W. P.; Thurston, R. N. Use of Piezoresistive Materials in the Measurement of Displacement, Force, and Torque. *J. Acoust. Soc. Am.* 1957, *29* (10), 1096.

(5) Segev-Bar, M.; Landman, A.; Nir-Shapira, M.; Shuster, G.; Haick, H. Tunable Touch Sensor and Combined Sensing Platform: Toward Nanoparticle-Based Electronic Skin. *ACS Appl. Mater. Interfaces* 2013, *5* (12), 5531–5541.

(6) Yi, L.; Jiao, W.; Wu, K.; Qian, L.; Yu, X.; Xia, Q.; Mao, K.; Yuan, S.; Wang, S.; Jiang, Y. Nanoparticle Monolayer-Based Flexible Strain Gauge with Ultrafast Dynamic Response for Acoustic Vibration Detection. *Nano Res.* 2015, *8* (9), 2978–2987.

(7) Ho, D. H.; Sun, Q.; Kim, S. Y.; Han, J. T.; Kim, D. H.; Cho, J. H. Stretchable and Multimodal All Graphene Electronic Skin. *Adv. Mater.* 2016, *28*, 2601–2608.

(8) Hu, N.; Karube, Y.; Yan, C.; Masuda, Z.; Fukunaga, H. Tunneling Effect in a Polymer/carbon Nanotube Nanocomposite Strain Sensor. *Acta Mater.* 2008, *56* (13), 2929–2936.

(9) Bayley, H.; Martin, C. R. Resistive-Pulse Sensing-from Microbes to Molecules. *Chem. Rev.* 2000, *100* (7), 2575–2594.

(10) Hossain, M. K.; Willmott, G. R.; Etchegoin, P. G.; Blaikie, R. J.; Tallon, J. L. Tunable SERS Using Gold Nanoaggregates on an Elastomeric Substrate. *Nanoscale* 2013, *5* (64), 8945–8950.

(11) Kang, H.; Heo, C. J.; Jeon, H. C.; Lee, S. Y.; Yang, S. M. Durable Plasmonic Cap Arrays on Flexible Substrate with Real-Time Optical Tunability for High-Fidelity SERS Devices. *ACS Appl. Mater. Interfaces* 2013, *5* (11), 4569–4574.

(12) Zaretski, A. V.; Root, S. E.; Savchenko, A.; Molokanova, E.; Printz, A. D.; Jibril, L.; Arya, G.; Mercola, M.; Lipomi, D. J. Metallic Nanoislands on Graphene as Highly Sensitive Transducers of Mechanical, Biological, and Optical Signals. *Nano Lett.* 2016.

(13) Huang, N. T.; Truxal, S. C.; Tung, Y. C.; Hsiao, A.; Takayama, S.; Kurabayashi, K. High-Speed Tuning of Visible Laser Wavelength Using a Nanoimprinted Grating Optical Tunable Filter. *Appl. Phys. Lett.* 2009, *95* (21), 2–4.

(14) Kim, K.; Seo, J.; Oh, M. Strain Induced Tunable Wavelength Filters Based on Flexible Polymer Waveguide Bragg Reflector. *Opt. Express* 2008, *16* (3), 1423–1430.

(15) Truxal, S. C.; Kurabayashi, K.; Tung, Y.-C. Design of a MEMS Tunable Polymer Grating for Single Detector Spectroscopy. *Int. J. Optomechatronics* 2008, *2* (2), 75–87.

(16) Fudouzi, H.; Sawada, T. Photonic Rubber Sheets with Tunable Color by Elastic Deformation. *Langmuir* 2006, No. 14, 1365–1368.

(17) Olcum, S.; Kocabas, A.; Ertas, G.; Atalar, A.; Aydinli, A. Tunable Surface Plasmon Resonance on an Elastomeric Substrate. *Opt. Express* 2009, *17* (10), 2051–2056.

(18) Huang, F.; Baumberg, J. J. Actively Tuned Plasmons on Elastomerically Driven Au Nanoparticle Dimers. *Nano Lett.* 2010, *10* (5), 1787–1792.

(19) Qian, X.; Park, H. S. The Influence of Mechanical Strain on the Optical Properties of Spherical Gold Nanoparticles. *J. Mech. Phys. Solids* 2010, *58* (3), 330–345.

(20) Wu, W.; Ren, M.; Pi, B.; Wu, Y.; Cai, W.; Xu, J. Scaffold Metamaterial and Its Application as Strain Sensor. *Appl. Phys. Lett.* 2015, *107* (9), 18–21.

(21) Cui, Y.; Zhou, J.; Tamma, V. A.; Park, W. Dynamic Tuning and Symmetry Lowering of Fano Resonance in Plasmonic Nanostructure. *ACS Nano* 2012, *6* (3), 2385–2393.

(22) Wilson, E. B. The Normal Modes and Frequencies of Vibration of the Regular Plane Hexagon Model of the Benzene Molecule. *Phys. Rev.* 1934.

(23) Ru, E. Le; Etchegoin, P. *Principles of Surface-Enhanced Raman Spectroscopy: And Related Plasmonic Effects*; Elsevier, 2008; Vol. 17.

(24) Alexander, K. D.; Skinner, K.; Zhang, S.; Wei, H.; Lopez, R. Tunable SERS in Gold Nanorod Dimers through Strain Control on an Elastomeric Substrate. *Nano Lett.* 2010, *10* (11), 4488–4493.

(25) Eustis, S.; El-Sayed, M. A. Why Gold Nanoparticles Are More Precious than Pretty Gold: Noble Metal Surface Plasmon Resonance and Its Enhancement of the Radiative and Nonradiative Properties of Nanocrystals of Different Shapes. *Chem. Soc. Rev.* 2006, *35* (3), 209–217.

(26) Stiles, P. L.; Dieringer, J. A; Shah, N. C.; Van Duyne, R. P. Surface-Enhanced Raman Spectroscopy. *Annu. Rev. Anal. Chem.* 2008, *1*, 601–626.

(27) Zhao, Y.; Li, X.; Du, Y.; Chen, G.; Qu, Y.; Jiang, J.; Zhu, Y. Strong light–matter interactions in sub-nanometer gaps defined by monolayer graphene: toward highly sensitive SERS substrates. *Nanoscale* **2014**, *6*, 11112–11120.

(28) Maier, S. A.; Kik, P. G.; Atwater, H. A.; Meltzer, S.; Requicha, A. A. G.; Koel, B. E. Observation of Coupled Plasmon-Polariton Modes of Plasmon Waveguides for Electromagnetic Energy Transport below the Diffraction Limit. *Proc. SPIE* 2002, *4810*, 71–81.

(29) Zhang, X.; Zhao, J.; Whitney, A. V; Elam, J. W.; Van Duyne, R. P. Ultrastable Substrates for Surface-Enhanced Raman Spectroscopy: Al2O3 Overlayers Fabricated by Atomic Layer Deposition Yield Improved Anthrax Biomarker Detection. *J. Am. Chem. Soc.* 2006, *128* (31), 10304–10309.

(30) Jain, P. K.; Huang, W.; El-Sayed, M. A. On the Universal Scaling Behavior of the Distance Decay of Plasmon Coupling in Metal Nanoparticle Pairs: A Plasmon Ruler Equation. *Nano Lett.* 2007, *7* (7), 2080–2088.

(31) Willets, K. A; Van Duyne, R. P. Localized Surface Plasmon Resonance Spectroscopy and Sensing. *Annu. Rev. Phys. Chem.* 2007, *58*, 267–297.

(32) Lee, K.-S.; El-Sayed, M. A. Gold and Silver Nanoparticles in Sensing and Imaging: Sensitivity of Plasmon Response to Size, Shape, and Metal Composition. *J. Phys. Chem. B* 2006, *110* (39), 19220–19225.

(33) Orendorff, C. J.; Gearheart, L.; Jana, N. R.; Murphy, C. J. Aspect Ratio Dependence on Surface Enhanced Raman Scattering Using Silver and Gold Nanorod Substrates. *Phys. Chem. Chem. Phys.* 2006, *8* (1), 165–170.

(34) Tripp, R. A.; Dluhy, R. A.; Zhao, Y. Novel Nanostructures for SERS Biosensing. *Nano Today* 2008, *3* (3–4), 31–37.

(35) Porter, M. D.; Lipert, R. J.; Siperko, L. M.; Wang, G.; Narayanan, R. SERS as a Bioassay Platform: Fundamentals, Design, and Applications. *Chem. Soc. Rev.* 2008, *37* (5), 1001–1011.

(36) Sangeetha, N. M.; Decorde, N.; Viallet, B.; Viau, G.; Ressier, L. Nanoparticle-Based Strain Gauges Fabricated by Convective Self Assembly: Strain Sensitivity and Hysteresis with Respect to Nanoparticle Sizes. *J. Phys. Chem. C* 2013, *117*, 1935–1940.

Chapter 6

Graphene-Metal Composite Sensors with Near-Zero Temperature Coefficient of Resistance

Brandon C. Marin, Samuel E. Root, Armando D. Urbina, Eden Aklile, Rachel Miller, Aliaksandr V. Zaretski, Darren J. Lipomi[a]

[a]*NanoEngineering Department, University of California, San Diego.*

9500 Gilman Drive MC 0448, La Jolla, CA 92093-0448

Abstract

This article describes the design of piezoresistive thin-film sensors based on single-layer graphene decorated with metallic nanoislands. The defining characteristic of these composite thin films is that they can be engineered to exhibit a temperature coefficient of resistance (TCR) that is close to zero. A mechanical sensor with this property is stable against temperature fluctuations of the type encountered during operation in the real world—e.g., in a wearable sensor. The metallic nanoislands are grown on graphene using thermal deposition of metal (gold or palladium) at low nominal thickness. Metallic films exhibit an increase in resistance with temperature (positive TCR) while graphene exhibits a decrease in resistance with temperature (negative TCR). By varying the amount of deposition, the morphology of the nanoislands can be tuned such that the TCRs of metal and graphene cancel out. Quantitative analysis of scanning electron microscope images reveals the importance of the surface coverage of the metal (as opposed to the total mass of metal deposited). The stability of the sensor to temperature fluctuations that might be encountered in the outdoors is demonstrated by subjecting a wearable pulse sensor to simulated solar irradiation.

6.1 Introduction

Wearable and implantable sensors can be designed to detect a range of chemical, biophysical, electromagnetic, and thermal stimuli. Few types of sensors, however, are responsive to only one type of stimulus. For example, strain gauges based on metallic thin films are sensitive to mechanical deformation, but also to temperature. Unwanted sensitivity to temperature could arise because of, for example, thermal expansion of the

substrate, or the fact that the conductivity of a metal depends on temperature (i.e., the temperature coefficient of resistance, TCR). Our laboratory has previously shown that metallic nanoislands on graphene are sensitive to a wide range of mechanical, optical, chemical, and electrophysiological signals.[1,2] During the course of these experiments, we noticed that thermal drift—i.e., small changes in the local ambient temperature—produced changes in electrical resistance of the sensors that were comparable to or greater than those produced by the stimuli of interest. The problem of convoluted signals is not unique to this type of sensor, but is rarely reported for experiments on other types of sensors, which are performed in well-controlled environments.

Decoupling the signal of interest from unwanted signals can be addressed in one of at least two ways: (1) by processing the signals using back-end electronics or (2) by the design of the material used for sensing. This paper uses the second approach—in which decoupling of thermal drift is accomplished by the material itself. Since graphene exhibits a TCR that is less than zero,[3] and metals exhibit a TCR that is greater than zero,[4] we fabricated composite thin films consisting of metallic nanoislands supported by single-layer graphene (**Figure 6.1**). (Metallic nanoislands are the disconnected structures that form with low nominal thicknesses when metals are deposited by physical vapor deposition.) By tuning the amount of metal deposited—and thus the interconnectivity and surface coverage of the nanoislands—it was possible to engineer the composite material such that the TCR of the two different materials cancelled to near zero.

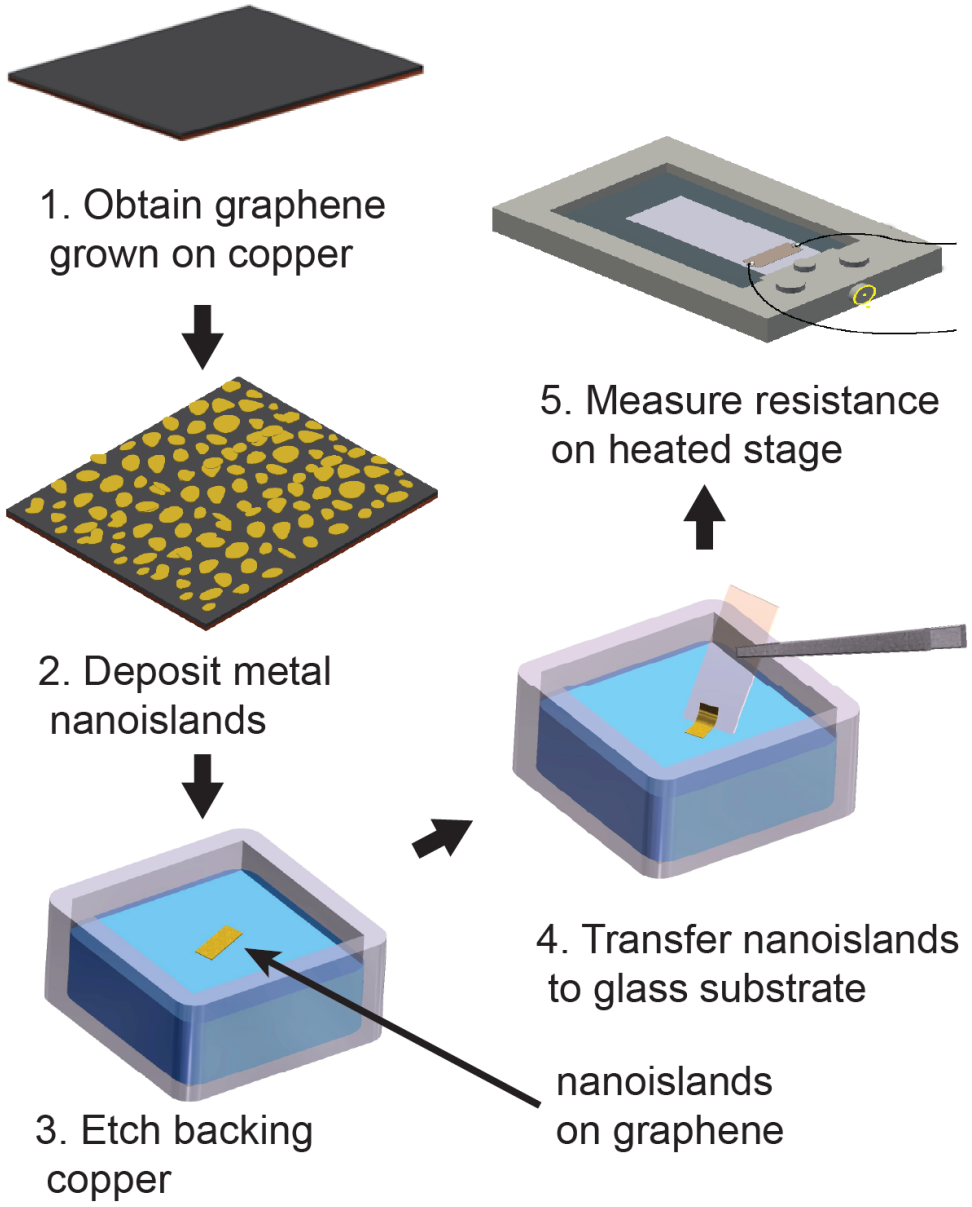

Figure 6.1. Schematic diagram of process used to generate and transfer metallic nanoislands on graphene. Nanoislands are formed by thermal evaporation of metal onto copper-supported graphene. The backing copper is etched using a basic ammonium persulfate solution. The film can then be transferred to a substrate of interest and addressed for electrical measurements.

Previous work on the topic of zero-TCR materials has been primarily concerned with bulk metal alloys and other materials that require complex processing. Metal alloys include manganin and constantin; the latter has been used for over a century in the

components of thermocouples. New alloys[5,6,7] have been developed, along with tunable-TCR materials such as metal-polymer composites,[8,9,10,11] carbon mixtures,[12] and semiconductor composites.[13,14,15] Optical strain sensors that are temperature-independent have also been reported.[16] However, polymer and carbon mixtures involve complex solution processing, and metal alloys reported so far have been bulk materials, as opposed to thin films. For near-zero TCR resistive sensing elements to be useful in flexible and wearable devices, it is desirable to have active materials that are thin, transparent, and mechanically robust.

A single layer of graphene behaves as a zero-gap semiconductor with a negative TCR at room temperature. The resistivity is dominated by the charge-carrier concentration, and decreases with temperature as more hot carriers become available.[17] This phenomenon is in contrast to metals, which typically have a positive TCR due to an increase in both inelastic electron scattering and lattice spacing with temperature.[18] Given our previous experience with metal nanoislands on graphene as a platform for multimodal sensing,[19,2] we hypothesized that a zero-TCR sensor could be fabricated if the right amount of metal was deposited onto the graphene such that the effects of each material cancel each other out. To design this material, we have characterized the effect of deposition thickness and island morphology on the TCR of the graphene-metal composites. Gold and palladium were selected as the metals to test this hypothesis because of their widespread use in thermal and chemical thin film sensing, and disparate morphologies formed when evaporated onto graphene.[1,20]

6.2 Experimental

6.2.1 Metal Nanoisland Sensor Fabrication

Metal nanoislands were fabricated by physical vapor deposition using an AJA International thermal evaporator (Orion-class). A thin-film of palladium or gold was deposited onto graphene supported on copper foil at a rate of 0.05 Å/s. Chamber pressure during deposition was 2.0×10^{-7} torr. The resulting structure comprised nanoislands on graphene on copper foil (nanoisland/Gr/Cu). 200 nm of poly(methylmethacrylate) (PMMA) (1 kDa) was spin coated (1% wt solution in anisole at 4 kRPM for 60 s) onto the nanoisland side of the nanoisland/Gr/Cu sample. The backing copper foil was etched by floating the sample copper-side-down in an aqueous ammonium persulfate solution (50 mg/mL) for approximately 3 h. The samples were then transferred onto a 1 in × 3 in glass slide. The PMMA layer was then dissolved using neat acetone at 40 °C.

6.2.2 Scanning-Electron Microscopy (SEM)

An FEI XL30 SFEG with an FEI Sirion column and Through Lens Detector was used for SEM micrographs of metal nanoislands. An accelerating voltage of 10 kV and spot of 50 μm was used for imaging.

6.2.3 Temperature Coefficient of Resistance Measurements

Resistance measurements were obtained using a Keithley 2400 sourcemeter. All resistance measurements for wearable applications and TCR calculations were conducted using two-point measurements. To decouple possible effects of contact resistance of the carbon paint from the intrinsic resistance of the graphene-nanoisland films, we compared the resistances obtained using two-point measurements to those obtained using four-point measurements. The fact that the resistance values differed by less than 1% suggested that the contact resistance due to the carbon paint was negligible. All samples had the same

dimensions. Samples for TCR measurements were heated using an Instec FS1 heated stage with an Instec mK2000 temperature controller and electrically addressed with eutectic gallium-indium (EGaIn).

6.2.4 Image Analysis

An object-oriented Python code was developed to perform image analysis of the SEM images. This code made extensive use of the Mahotas package (See Supplementary Information) to distinguish metal from graphene, identify separate nanoislands and quantify the area of the individual nanoislands as well as their fractional coverage over the graphene. The code could be easily adapted for analysis of similar nanostructures and is openly available at github.

6.2.5 Rapid Thermal Annealing

Rapid thermal annealing was performed using an AG Associates Heat Pulse 610. The samples were heated from room temperature to 600 °C in 12 s (50 °C/s) under forming gas (5% hydrogen / 95% nitrogen) to aid reflow of the metal. The sample was held at the elevated temperature for 5 min.

6.3 Results and Discussion

6.3.1 Thermoresistive behavior of metal nanoislands

The relationship between electrical resistance, temperature, and thickness for metal nanoislands on graphene is summarized in **Figure 6.2a** (gold) and 6.**2b** (palladium). The reported thicknesses are the "nominal" values measured by the quartz crystal microbalance (QCM) in the evaporation chamber. (The true thickness is poorly defined because of the disconnected nature of the nanoisland films.) To find the TCR of

these samples, we measured the normalized resistance as a function of temperature (from 30 °C to 65 °C); the TCR is the slope of this curve. As we expected, the TCR of the composite films exhibited a strong dependence on nominal thickness of the metallic film. The SEM images shown in **Figure 6.2c-2h** suggest that the morphology—i.e., interconnectivity or fractional surface coverage—also influence the sensitivity to temperature.

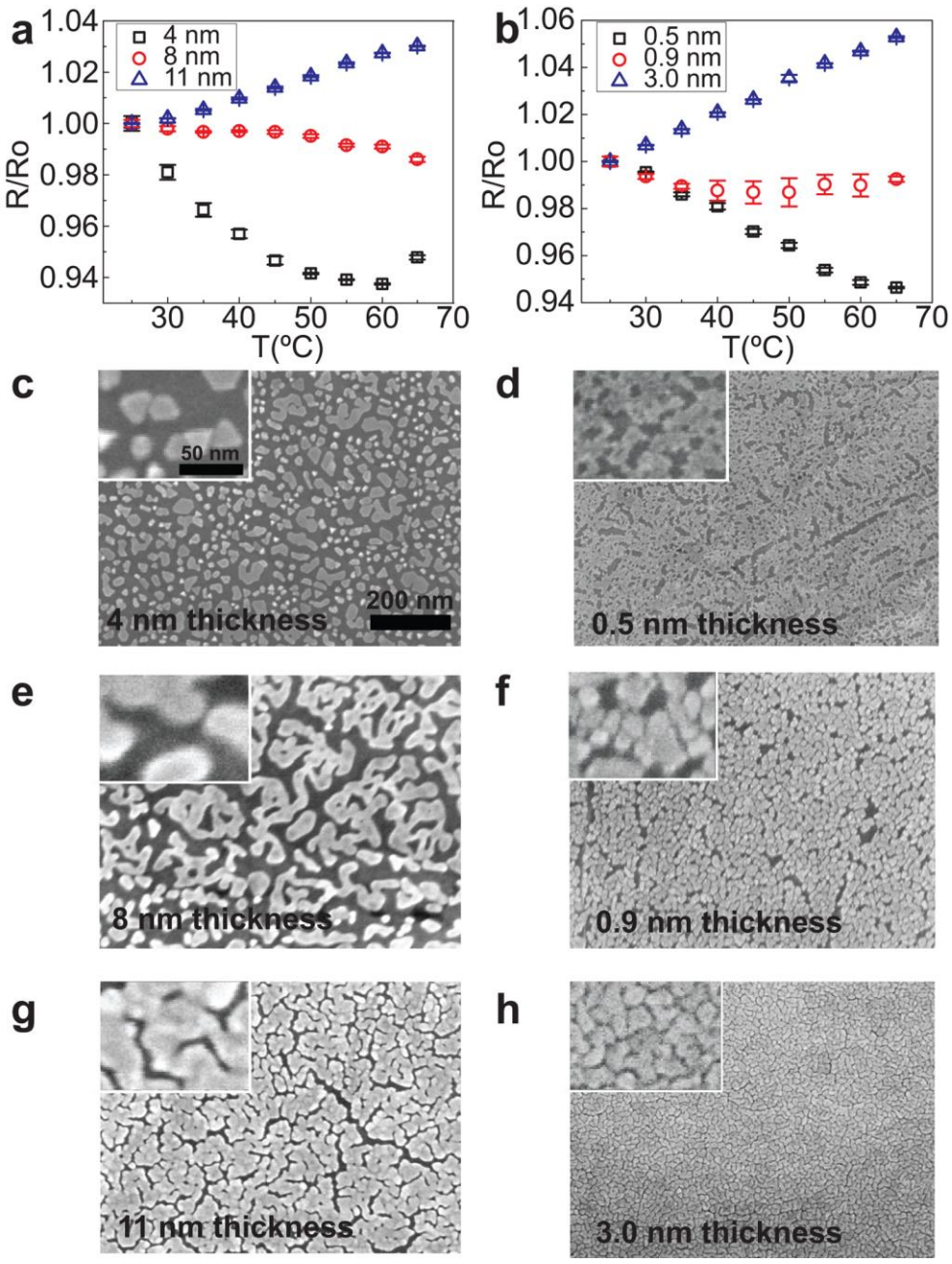

Figure 6.2. Thermoresistive behavior and morphology of gold and palladium nanoislands. The temperature-dependent normalized resistance is plotted for gold nanoislands (a) and palladium nanoislands (b) of varied nominal thicknesses. SEM micrographs depicting negative-TCR isolated nanoislands for 3 nm of gold (c) and 0.5 nm of palladium (d), near-zero TCR, partially percolated structures for 8 nm of gold (e) and 0.9 nm (f) of palladium, and positive TCR, fully percolated structures for 11 nm of gold (g) and 3.0 nm (h) of palladium. All SEM images are the same magnification.

The SEM images in **Figure 6.2c**, **d** show distinct differences between the morphologies of the negative TCR composites of gold and palladium, respectively. At a

nominal thickness of 4 nm, the gold assembles into large, separated islands with sharp crystalline facets. Palladium nanoislands, in contrast, are smaller than gold nanoislands at all nominal thicknesses. Moreover, they exhibit a higher fractional coverage at substantially lower nominal thicknesses (0.5 nm). It also appears that the palladium nanoislands may be interconnected.

The nominal thickness of deposition that gave near-zero TCR was 8 nm for gold and 0.9 nm for palladium. The SEM image in **Figure 6.2e** shows that gold forms fractal, partially percolated structures which result from isolated nanoislands coalescing in a disordered fashion during the growth process. On the other hand, the palladium nanoislands did not coalesce but did appear to be in intimate physical contact (**Figure 6.2f**). We attribute the differences in morphology to the differences in relative interaction energies between the surface and the metal nanoislands: palladium has a stronger attraction to the surface and a closer epitaxial registry (a smaller lattice constant).[21] Therefore, the palladium nanoislands are not as mobile during the growth process.[1] The SEM images in Figure 2g, h show that the gold and palladium form completely percolated nanostructures with nominal thickness greater than 11 nm and 3 nm respectively. Percolated structures in both materials yielded a positive TCR—evidence that the thermoresistive behavior approaches that of a thin film of metal.

In general, these results show that the TCR can be controlled as a function of nominal thickness of deposition. In cases when it is necessary to eliminate thermal drift, a substrate with a near-zero TCR can be repeatedly fabricated using either palladium or gold by targeting a specific thickness. Moreover, this procedure should be straightforward to transfer to any other transition metal of interest for a specific device

application. Interestingly, we found there to be a large difference in the nominal thickness that produced a near-zero TCR of palladium (0.9 nm) versus that for gold (8 nm). While morphologies can be reproduced by holding the deposition parameters constant (chamber pressure, evaporation rate, substrate, nominal thickness),[22] the nominal thickness is not a true indication of the thickness of individual nanoislands. Thus, we found it necessary to correlate the TCR with other morphological parameters to give a more sophisticated description of relationship between the TCR and the morphology of the metal nanoislands.

6.3.2 Image analysis and modeling of thermoresistive behavior of metal nanoislands

Image analysis was performed on the SEM micrographs of gold nanoislands to quantitatively analyze the trends between morphology and thermoresistive behavior. A thresholding algorithm known as Otsu's method[23] was implemented to differentiate the metal structures from graphene. The algorithm operates on the greyscale image by assuming two classes of pixels, which fall above or below a threshold value (metal vs. graphene). The optimum threshold value is defined as the one that minimizes the variance within each class of pixels. Once differentiated, distinct islands are labelled and various properties are computed including surface coverage and projected area. From **Figure 6.3a**, we can see that TCR varies linearly with coverage. Examples of processed images are given in **Figure 6.3b-d**, where the separate islands are colored by their area.

Given the observed dependence of TCR with coverage, we developed a model to describe the thermoresistive behavior of this composite material. Adomov et al.[24] have demonstrated that the TCR of vacuum deposited gold films depends on thickness, d, and can be described as:

$$\alpha_{Au} = \alpha_o \left(1 + \frac{3l}{8d}\right)^{-1}$$

where α_{Au} is the TCR of gold and l is the electron mean free path (400 Å). The actual island thickness can be related to the nominal thickness using the coverage, θ, and the following relation:

$$d = \frac{d^*}{\theta}$$

Finally, the TCR of the gold islands can be combined with the TCR of the supporting graphene (α_{Gr}) using a composite theory, with coverage as the fractional variable:

$$\alpha_c = \theta\alpha_{Au} + (1 - \theta)\alpha_{Gr}$$

The results of our model are compared to the experimental data in **Figure 6.3a**, and demonstrate good agreement. Additional details on the composite model are available in **Appendix D**.

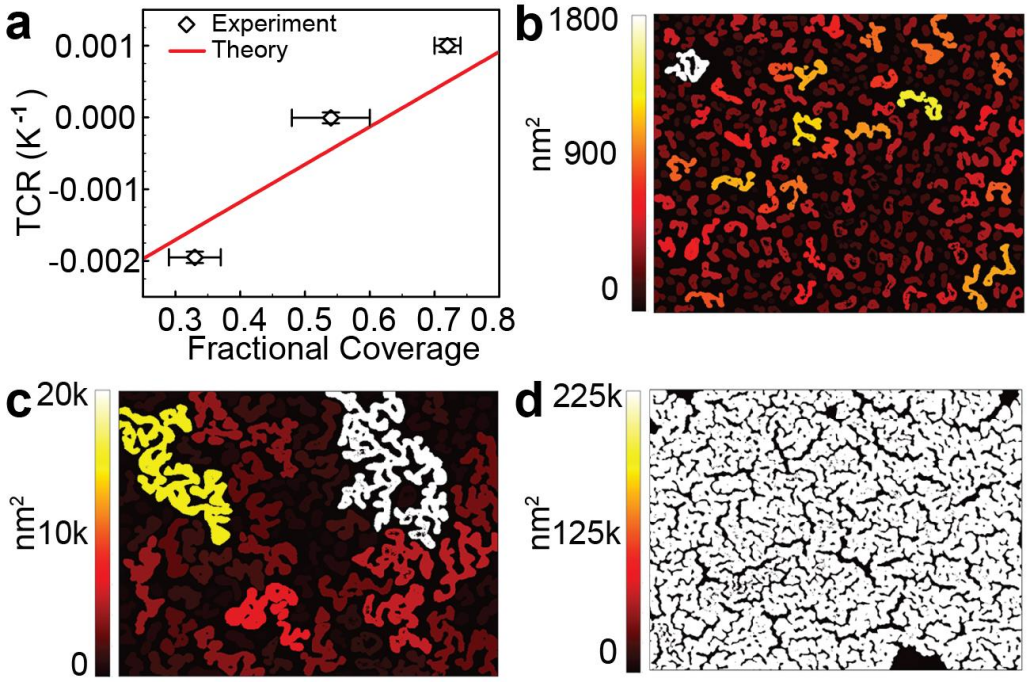

Figure 6.3. Morphological dependence of TCR of gold nanoislands obtained through image analysis. (a) Plot showing linear dependence of TCR on fractional coverage. Representative processed images for (b) negative TCR (4 nm), (c) near zero TCR (8 nm), and (d) positive TCR (11 nm) gold nanoislands. Islands are colored by projected area (nm^2). The film in (d) is entirely white because it is a single interconnected structure of area 225k nm^2

The results of our model suggested that the lateral distribution of the metal was more important than the total mass deposited. To test this idea, we subjected an 11 nm gold nanoisland sample to rapid-thermal annealing (RTA), a method that has commonly been used to change the morphology of metallic films on the nanoscale.[25,26] The sample was heated from room temperature to 600 °C in 12 s and held at the elevated temperature for 5 min. This thermal abuse changed the morphology of the metal from a percolated network to a distribution of isolated nanoparticles (**Figure D3**). The TCR of the sample changed concomitantly from positive to negative (**Figure D4**). This experiment unambiguously demonstrated the importance of interconnectivity and surface coverage of the metal islands on the TCR of the composite material.

6.3.3 Wearable application of sensor with near-zero TCR

To demonstrate the utility of thin films resistant to thermal drift, we fabricated a wearable sensor for detecting the human pulse using gold nanoislands. Nanoisland-graphene films with positive, negative, and near-zero TCRs were transferred onto Kapton tape, addressed with carbon paint, then adhered onto the wrist as depicted in **Figure 6.4a**. A schematic diagram of the sensor is shown in **Figure D7**. To simulate a plausible real-world scenario where an abrupt heating event would occur, we placed the sensor (on the wrist) over a solar simulator lamp to imitate the direct illumination of a sensor by the sun. As indicated by the gray shaded area in **Figure 6.4b**, the gold nanoislands with the near-zero TCR exhibited minimal thermal drift. On the other hand, the positive- and negative-TCR sensors experienced a substantial drift due to heating caused by direct illumination. When placed on the wrist, periodic strain caused by the contractions of the radial artery induced a periodic change in resistivity. This pulse signal was detected by the sensor (**inset Figure 6.4b**). To address whether the sensitivity of the wearable sensor was affected by changing the nominal thickness of metal to attain a near-zero TCR, we examined the data closely in **Figure 6.4b**. Assuming the strain caused by a pulse was constant (since the same subject was used for all measurements in **Figure 6.4b**), the pulse signal was most pronounced in the near-zero TCR sensor, indicating that the sensor performance was not diminished by changing the nominal thickness of metal. We then tested for any possible interference from temperature-dependent conductivity of the carbon paint itself. We attached copper wires to a gold film (50 nm) using a drop of carbon paint with similar dimensions to those used in the wearable sensors. Continuous measurement of resistance as a function of temperature from ambient to 60 °C revealed a

net increase in resistance of <1%. Given this small effect and the fact that the samples were all connected using the same materials, we could confirm that the observed differences in TCR between the graphene-nanoisland films were due to the coverage and interconnectivity of the nanoislands.

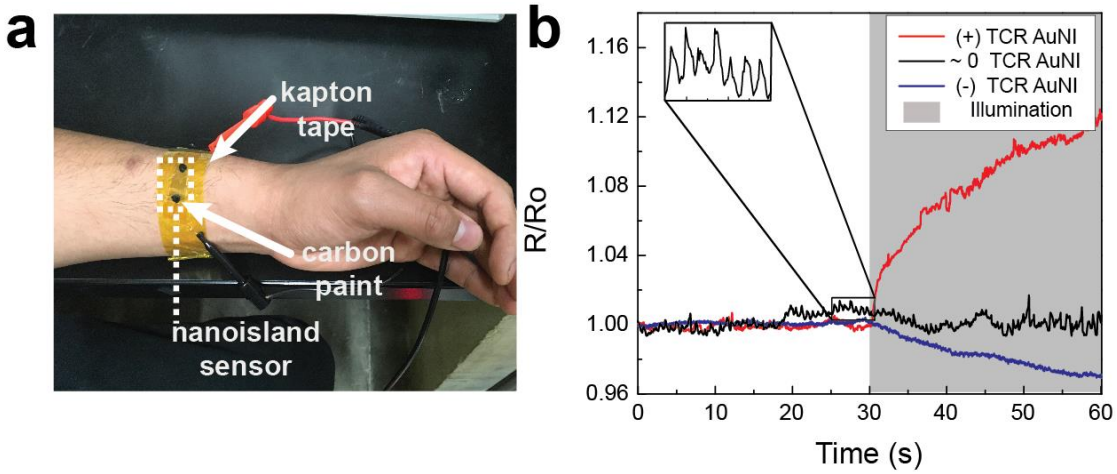

Figure 6.4. Thermal drift of a wearable pulse sensor under simulated sunlight. (a) A wearable pulse sensor with the nanoisland portion outlined in black dashed lines. (b) Normalized resistance is plotted versus time with a period of illumination by a solar simulator lamp, which is marked by the gray shaded area. The lamp heated the sensor to a steady-state temperature of approximately 45 °C after 30 s as measured by an infrared thermometer. The inset shows a clear pulse, with dicrotic notches clearly visible.

6.4 Conclusions

We reported a new strategy to suppress thermal drift in sensors. This strategy is based on the precise control of materials in sensors composed of graphene decorated with metal nanoislands. By systematically varying the nominal thickness of metal deposited, we found optimal deposition parameters to produce composite thin films with near-zero TCR for both gold and palladium on graphene. Differences in the self-assembly process of gold nanoislands suggested that surface coverage and interconnectivity were the most

important morphological parameters in determining the TCR of the composite material. Image analysis of SEM images provided quantitative evidence to support this conclusion, and enabled the development of a model to describe the thermoresistive behavior of the composite material. Proof-of-concept wearable sensors were fabricated to demonstrate the stability of the electrical signal to variations in surface temperature produced by sunlight. This materials-design strategy should be easily generalizable to other transition metals for device-specific applications (e.g., chemical sensing), and provides a robust platform for the development of devices that minimize fluctuations due to temperature. More generally, these experiments demonstrate how well known materials can be combined in new ways to design thin-film composites with useful properties for device applications.

Acknowledgments

This work was supported by the National Institutes of Health Director's New Innovator Award, grant 1DP2EB022358-01 to D. J. L., and by a Diversity Supplement (for B. C. M.) under the same award number. E. A. received partial support from the CA-NASA/UCSD Space Grant Consortium. This work was performed in part at the San Diego Nanotechnology Infrastructure (SDNI), a member of the National Nanotechnology Coordinated Infrastructure, which is supported by the National Science Foundation (Grant ECCS-1542148).

Chapter 6, in full, is a reprint of the material as it appears in ACS Omega, 2017, 2(2), 626-630. The American Chemical Society 2017. Brandon C. Marin, Samuel E. Root, Armando D. Urbina, Eden Aklile, Rachel Miller, Aliaksandr V. Zaretski, and

Darren J. Lipomi. The dissertation author was the primary investigator and author of this material.

References

(1) Zaretski, A. V.; Root, S. E.; Savchenko, A.; Molokanova, E.; Printz, A. D.; Jibril, L.; Arya, G.; Mercola, M.; Lipomi, D. J. Metallic Nanoislands on Graphene as Highly Sensitive Transducers of Mechanical, Biological, and Optical Signals. *Nano Lett.* 2016, *16* (2).

(2) Marin, B. C.; Liu, J.; Aklile, E.; Urbina, A. D.; Chiang, A. S.; Lawrence, N.; Chen, S.; Lipomi, D. J. SERS-Enhanced Piezoplasmonic Graphene Composite for Biological and Structural Strain Mapping. *Nanoscale* 2016. DOI: 10.1039/c6nr09005b.

(3) Shao, Q.; Liu, G.; Teweldebrhan, D.; Balandin, A. A. Higherature Quenching of Electrical Resistance in Graphene Interconnects. *Appl. Phys. Lett.* 2008, *92* (19).

(4) Mott, N. F. The Resistance and Thermoelectric Properties of the Transition Metals. *Proc. R. Soc. Lond. A. Math. Phys. Sci.* 1936, *156* (888), 368–382.

(5) Yi, L.; Jiao, W.; Zhu, C.; Wu, K.; Zhang, C.; Qian, L.; Wang, S.; Jiang, Y.; Yuan, S. Ultrasensitive Strain Gauge with Tunable Temperature Coefficient of Resistivity. *Nano Res.* 2016, *9* (5), 1–12.

(6) Neugebauer, C. A.; Webb, M. B. Electrical Conduction Mechanism in Ultrathin, Evaporated Metal Films. *J. Appl. Phys.* 1962, *33* (1), 74–82.

(7) Fu, B.; Gao, L. Tantalum Nitride/Copper Nanocomposite with Zero Temperature Coefficient of Resistance. *Scr. Mater.* 2006, *55* (6), 521–524.

(8) Lee, S.-E.; Sohn, Y.; Chu, K.; Kim, D.; Park, S.-H.; Bae, M.; Kim, D.; Kim, Y.; Han, I.; Kim, H.-J. Suppression of Negative Temperature Coefficient of Resistance of Multiwalled Nanotube/silicone Rubber Composite through Segregated Conductive Network and Its Application to Laser-Printing Fusing Element. *Org. Electron.* 2016, *37*, 371–378.

(9) Pang, H.; Zhang, Y. C.; Chen, T.; Zeng, B. Q.; Li, Z. M. Tunable Positive Temperature Coefficient of Resistivity in an Electrically Conducting Polymer/graphene Composite. *Appl. Phys. Lett.* 2010, *96* (25).

(10) Pang, H.; Chen, C.; Bao, Y.; Chen, J.; Ji, X.; Lei, J.; Li, Z. M. Electrically Conductive Carbon Nanotube/ultrahigh Molecular Weight Polyethylene Composites with Segregated and Double Percolated Structure. *Mater. Lett.* 2012, *79* (November 2016), 96–99.

(11) Li, G.; Hu, C.; Zhai, W.; Zhao, S.; Zheng, G.; Dai, K.; Liu, C.; Shen, C. Particle Size Induced Tunable Positive Temperature Coefficient Characteristics in Electrically Conductive Carbon Nanotubes/polypropylene Composites. *Mater. Lett.* 2016, *182*, 314–317.

(12) Sun, P.; Zhu, M.; Wang, K.; Zhong, M.; Wei, J.; Wu, D.; Zhu, H. Small Temperature Coefficient of Resistivity of Graphene/graphene Oxide Hybrid Membranes. *ACS Appl. Mater. Interfaces* 2013, *5* (19), 9563–9571.

(13) Lin, J. C.; Wang, B. S.; Tong, P.; Lin, S.; Lu, W. J.; Zhu, X. B.; Yang, Z. R.; Song, W. H.; Dai, J. M.; Sun, Y. P. Tunable Temperature Coefficient of Resistivity in C- and Co-Doped $CuNMn_3$. *Scr. Mater.* 2011, *65* (5), 452–455.

(14) Lin, S.; Wang, B. S.; Lin, J. C.; Huang, Y. N.; Lu, W. J.; Zhao, B. C.; Tong, P.; Song, W. H.; Sun, Y. P. Tunable Room-Temperature Zero Temperature Coefficient of Resistivity in Antiperovskite Compounds Ga1−xCFe3 and Ga1−yAlyCFe3. *Appl. Phys. Lett.* 2012, *101* (1), 011908.

(15) Bonavolontà, C.; Camerlingo, C.; Carotenuto, G.; Nicola, S. De; Longo, A.; Meola, C.; Boccardi, S.; Palomba, M.; Pepe, G. P.; Valentino, M. Characterization of Piezoresistive Properties of Graphene-Supported Polymer Coating for Strain Sensor Applications. *Sensors Actuators A Phys.* 2016. DOI: 10.1016/j.sna.2016.11.002.

(16) Lee, S.; Lim, E. J.; Jo, I. S.; Yoo, K. W.; Han, Y. Temperature-Insensitive Strain Sensor Using a Microfiber Mach-Zehnder Interferometer. In *Asia-Pacific Optical Sensors Conference*; 2016; Vol. 2, pp 3–5.

(17) Geim, A K.; Novoselov, K. S. The Rise of Graphene. *Nat. Mater.* 2007, *6* (3), 183–191.

(18) Shivaprasad, S. M.; Angadi, M. A. Temperature Coefficient of Resistance of Thin Palladium Films. *J. Phys. D. Appl. Phys.* 1980, *13* (9), L171.

(19) Zaretski, A. V; Lipomi, D. J. Processes for Non-Destructive Transfer of Graphene: Widening the Bottleneck for Industrial Scale Production. *Nanoscale* 2015, *7* (22), 9963–9969.

(20) Zaretski, A. V.; Marin, B. C.; Moetazedi, H.; Dill, T. J.; Jibril, L.; Kong, C.; Tao, A. R.; Lipomi, D. J. Using the Thickness of Graphene to Template Lateral

Subnanometer Gaps between Gold Nanostructures. *Nano Lett.* 2015, *15* (1), 635–640.

(21) Buch, A. *Pure Metals Properties: A Scientific and Technical Handbook*, First.; ASM International: Materials Park, OH, 1999.

(22) Mattox, D. M. *Handbook of Physical Vapor Deposition (PVD) Processing*, Second Edi.; Elsevier: Oxford, 2010.

(23) Otsu, N. A Threshold Selection Method from Gray-Level Histograms. *Automatica* 1979, *11* (285), 23–27.

(24) Adamov, M.; Perovic, B.; Nenadovic, T. Electrical and Structural Properties of Thin Gold Films Obtained by Vacuum Evaporation and Sputtering. *Thin Solid Films* 1974, *24* (1), 89–100.

(25) Jia, K.; Bijeon, J.-L.; Adam, P.-M.; Ionescu, R. E. Large Scale Fabrication of Gold Nano-Structured Substrates Via High Temperature Annealing and Their Direct Use for the LSPR Detection of Atrazine. *Plasmonics* 2012, *8* (1), 143–151.

(26) Strekal, N.; Maskevich, A.; Maskevich, S.; Jardillier, J. C.; Nabiev, I. Selective Enhancement of Raman or Fluorescence Spectra of Biomolecules Using Specifically Annealed Thick Gold Films. *Biopolymers* 2000, *57* (6), 325–328.

Appendix A

Supporting Information for Chapter 2: Plasmon-Enhanced Two-Photon Absorption in Photoluminescent Semiconductor Nanocrystals

Brandon C. Marin, [†a] Su-Wen Hsu, [†a] Li Chen,[b] Ashley Lo,[a] Darwin W. Zwissler,[a] Zhaowei Liu.[b] and Andrea R. Tao[a*]

([†] Equal contribution)

[a] *NanoEngineering Department, University of California, San Diego. 9500 Gilman Drive MC 0448, La Jolla, CA 92093-0448*

[b] *Department of Electrical and Computer Engineering. University of California, San Diego.*

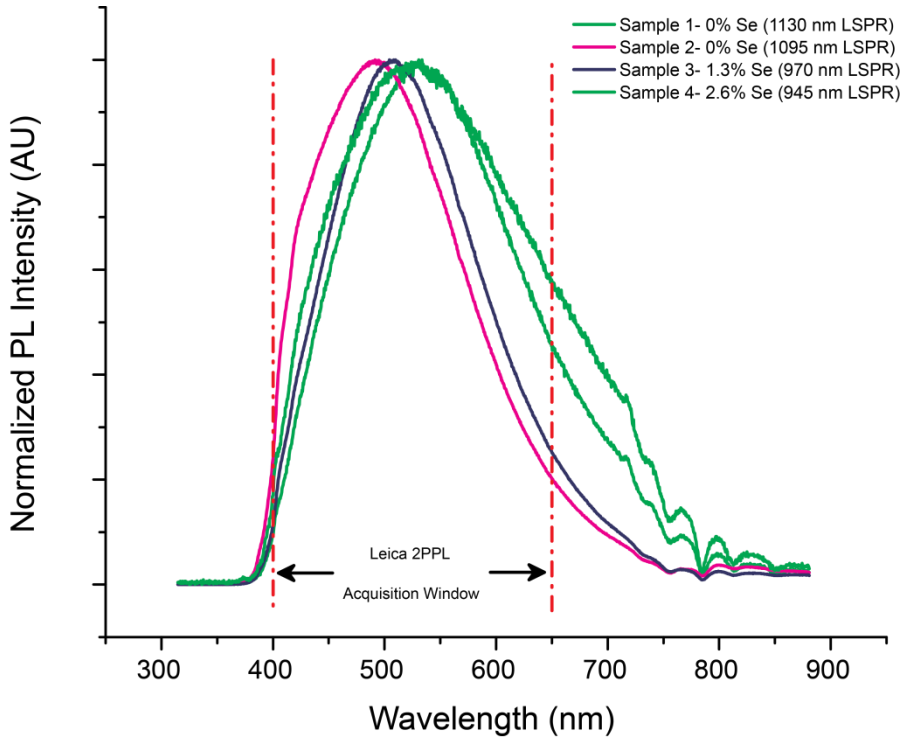

Figure A1. Typical PL spectra for doped CuS samples of varying concentrations. Window for signal acquisition during 2PE measurements is illustrated.

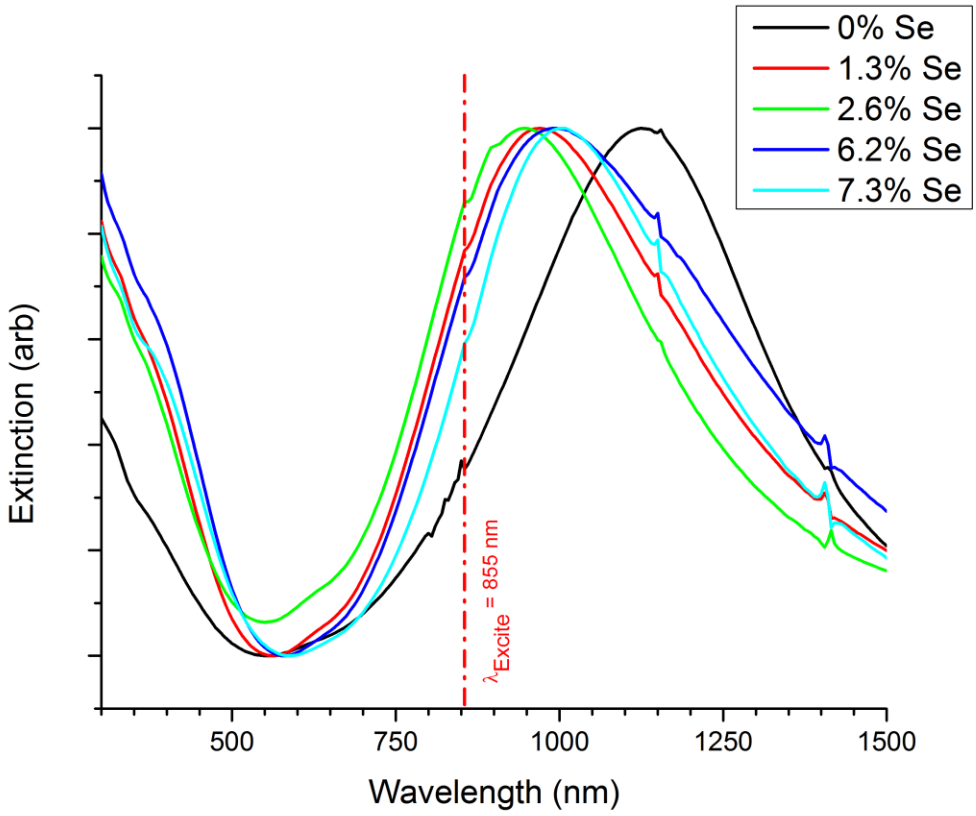

Figure A2. Extinction spectra for Se-doped CuS at various dopant concentrations. The blue-shifting of the LSPR wavelength is maximized at 2.6% Se-doping. The optimal laser excitation wavelength (λ_{Excite}) is highlighted to illustrate where the samples are stimulated during 2PE measurements.

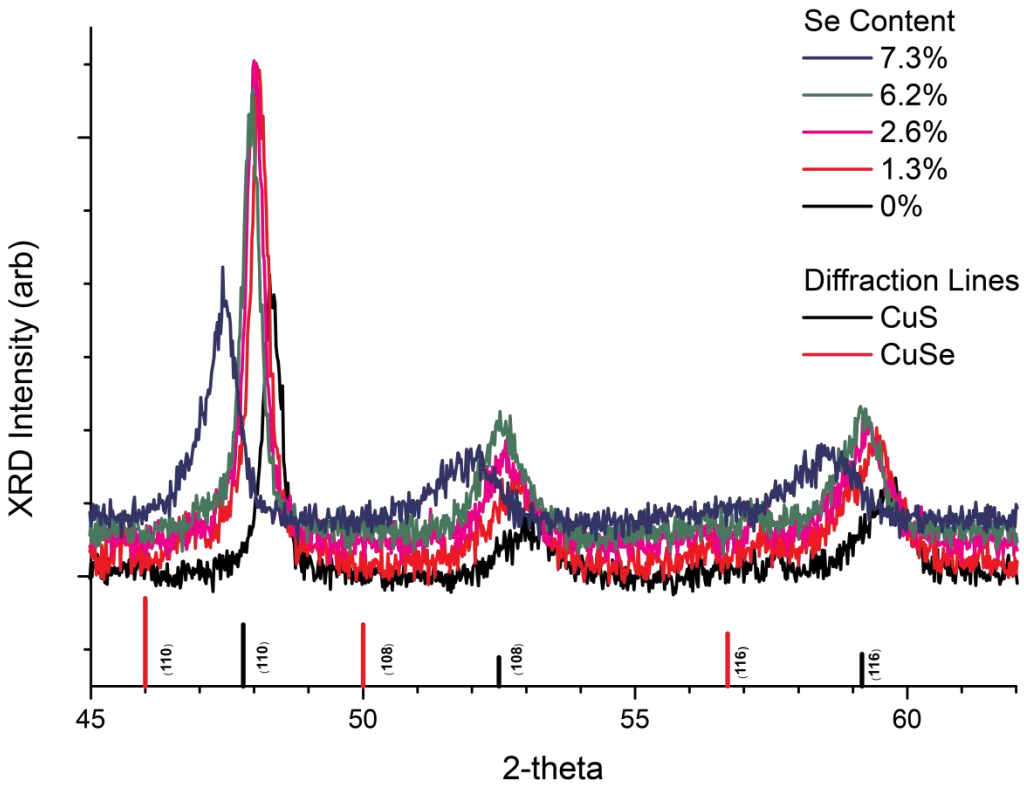

Figure A3. Powder XRD spectra for Se-doped CuS at various dopant concentrations. Diffraction pattern lines for CuS (covellite) phase and CuSe (klockmannite) phase are depicted for comparison. Peak shifting is observed for higher Se content, which suggests direct substitution of Se into the covellite lattice.

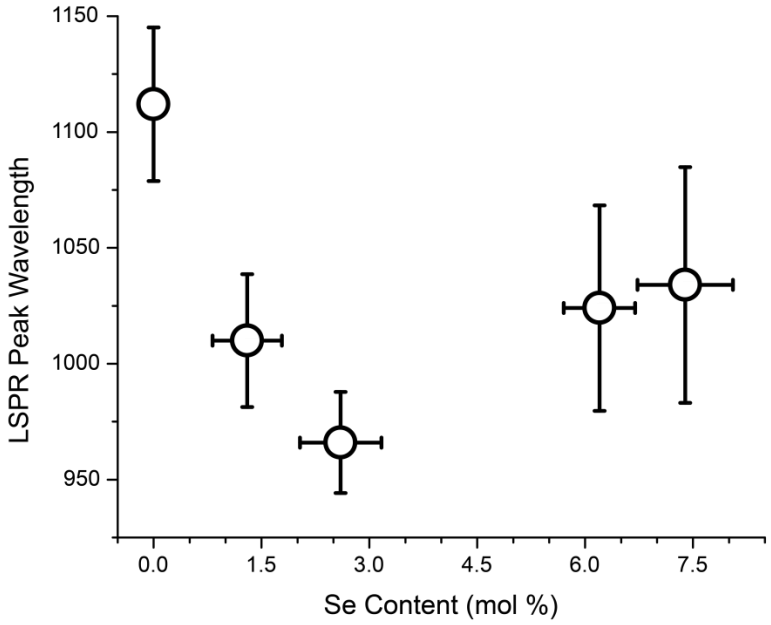

Figure A4. Dependence of λ_{LSPR} on Se-dopant concentration. Se concentration was determined by energy-dispersive spectroscopy (EDS) measurements.

Table A1. Table summarizing the morphology and optical properties of Se-doped CuS nanodisks. Averages and deviations were obtained from an analysis of >150 nanoparticles from TEM images.

Sample	Morphology				Optical Properties		
	Diameter (nm)	Thickness (nm)	Aspect Ratio	Se Content (%mol)	λ_{LSPR} (nm)	Action Cross Section (GM)	Molar Absorptivity at 855 nm (10^7 $cm^{-1}M^{-1}$)
1	32.23 ± 7.79	6.02 ± 1.52	5.03 ± 1.58	2.3	945	7211.5	4.67
2	31.11 ± 1.33	6.52 ± 0.88	4.69 ± 0.92	1.3	970	4551.7	4.29
3	31.99 ± 2.67	6.49 ± 1.27	4.81 ± 1.03	1.3	970	4481.5	4.33
4	30.50 ± 3.71	7.57 ± 1.66	3.88 ± 1.71	6.2	990	2849.7	4.03
5	29.01 ± 9.34	7.51 ± 1.81	3.91 ± 1.53	7.3	1090	2560.9	2.76
6	30.01 ± 1.41	5.81 ± 1.03	4.93 ± 1.28	0	1125	2322.2	2.15
7	29.25 ± 3.57	5.74 ± 0.96	4.95 ± 1.13	0	1150	2293.9	2.16
8	36.59 ± 15.40	6.18 ± 1.42	5.81 ± 1.59	0	1155	2255.2	1.72

A1. Calculation of Action Cross Section

Two-photon action cross sections were calculated using Equation 1 below and the method cited in the manuscript by Webb et Al. and others.[1,2] Briefly stated, the σ_S and ϕ_S are the sample's two-photon absorption absolute cross section and quantum efficiency, respectively. Their product ($\sigma_S\phi_S$) is the sample's two-photon action cross section, which is a measure of the sample's "brightness" under two-photon excitation. This is often reported over the absolute cross section, as the quantum efficiency is often difficult to determine. S_S, C_S, and n_S are the sample emission intensity, sample concentration, and sample solvent refractive index, respectively. Chloroform was used as a solvent for both sample and reference (n_R = n_S= 1.45). To calculate the action cross section for a sample, the action cross section for a reference ($\sigma_R\phi_R$) is needed. In this study, we used Lucifer Yellow as a reference. Lucifer Yellow has an action cross section value of $\sigma_R\phi_R$ = 0.95 GM (1 GM = 10^{-50}cm^{4}s/photon) as reported by Webb et Al.[3] Using the reported $\sigma_R\phi_R$ value, the concentration of reference used (C_R= 200 μM), the reference signal with our instrumentation (S_R = 235.6 cts), the sample signal (S_S), the solvent refractive indices (n), and the nanoparticle concentration (C_S) we can calculate the appropriate sample action cross section values ($\sigma_S\phi_S$). For example, for Sample 1 with C_S = 20 nM and S_S = 178.8 cts for Sample 1, we calculate a value of $\sigma_S\phi_S$ = 7211.5 GM.

$$\boldsymbol{\sigma_S\phi_S = \frac{S_S}{S_R}\frac{C_R}{C_S}\frac{n_R}{n_S}\sigma_R\phi_R} \quad (1)$$

Acknowledgments

This work is funded by a grant from the National Science Foundation (CHE, Award No. 1508755). The authors would like to thank the UCSD School of Medicine Microscopy Core for the use of their facility and acknowledge its supporting grant, NS047101. A.R.T. gratefully acknowledges financial support from the Arthur P. Sloan Foundation.

Appendix A, in full, is a reprint of the material as it appears in *ACS Photonics*, 2016, 3 (4), 526- 531. The American Chemical Society, 2016. Brandon C. Marin,[†] Su-wen Hsu,[†] Li Chen, Ashley Lo, Darwin W. Zwissler, Zhaowei Liu, and Andrea R. Tao. ([†] Equal contribution). The dissertation author was the primary investigator and author of this paper.

References

(1) Albota, M. A.; Xu, C.; Webb, W. W. Two-Photon Fluorescence Excitation Cross Sections of Biomolecular Probes from 690 to 960 nm. *Appl. Opt.* 1998, *37*, 7352–7356.

(2) Wang, X.; Tian, X.; Zhang, Q.; Sun, P.; Wu, J.; Zhou, H.; Jin, B.; Yang, J.; Zhang, S.; Wang, C.; Tao, X.; Jiang, M.; Tian, Y. Assembly, Two-Photon Absorption, and Bioimaging of Living Cells of a Cuprous Cluster. *Chem. Mater.* 2012, *24*, 954–961.

(3) Xu, C.; Webb, W. W. Measurement of Two-Photon Excitation Cross Sections of Molecular Fluorophores with Data from 690 to 1050 nm. *J. Opt. Soc. Am. B* 1996, *13*, 481.

Appendix B

Supporting Information for Chapter 3: Scalable and Templated Fabrication of Gold Nanobulbs for Surface-enhanced Raman Spectroscopy (SERS)-based Biosensing

Brandon C. Marin, [†a] Sameer S. Walavalkar, [†b], Chieh-Feng Chang, [†b]Andrea R. Tao,[a]

Axel Shearer,[c] and Scott Fraser[b]

([†] Equal contribution)

[a]*NanoEngineering Department, University of California, San Diego. 9500 Gilman Drive MC 0448, La Jolla, CA 92093-0448*

[b] *University of Southern California, Translational Imaging Center, 401 Irani Hall (RRI),1050 Childs Way, Los Angeles, CA 90089*

[c] *California Institute of Technology, Applied Physics Dept. MC 200-36, Pasadena, CA 91126*

B.1 Fabrication

Detail of the fabrication procedure is shown below in **Figure B1** as well as in previous work;[1–3] the numbering of the steps below corresponds to **Figure B1**. Fabrication is performed on intrinsic 2" [100] Si wafers. Wafers are rinsed with solvents in the following order: 1) IPA, 2) Acetone, 3) IPA, 4) Dichloromethane, 5) and IPA, followed by an N2 dry. PMMA A4 950

(MicroChem) is spun onto the wafer and baked at 180 ^{o}C to remove anisole. The pattern, circular regions corresponding to sets of nanopillars, is written using a Leica EBPG 5000+ at a 1200 $\frac{\mu C}{cm^2}$ dose and the PMMA is developed in a 1:3 MIBK:IPA solution. This creates the "negative" pattern seen in (i). Approximately 30 nm of stoichiometric[1] Al_2O_3 is deposited via reactive DC magnetron sputtering using an aluminum target and a mixed Ar:O_2 plasma (ii). Lift-off to define the hard-mask pattern is performed via sonication in a dichloromethane bath (iii). Pillars are etched in an Oxford Plasmalab Inductively Coupled Plasma Reactive Ion Etcher (ICP-RIE) 380 using a mixed mode, "pseudo-Bosch" etch. During the etch both the etching (SF_6) and passivation (C_4F_8) gases are present in the plasma. Etching is achieved under dynamic equilibrium conditions where the ICP power is used to control the rate of conformal C_4F_8 deposition and the forward power is used to accelerate ionized SF_6 species towards the substrate defining the milling rate on horizontal surfaces. The etch is balanced such that the milling rate is just able to overcome the passivation on the horizontal surfaces, allowing the etch to proceed vertically into the wafer as defined by the mask (iv and v). The resulting pillars are oxidized in a dry oxidation furnace at 1000 ^{o}C for 8 hours (vi). The gold layer is deposited via RF sputtering in an argon ambient to a thickness of 225nm (vii). The

reflow step is performed in a rapid thermal annealer under forming gas (5%H_2:95%N_2) environment. In this process the temperature is ramped to 675^{o}C in 30 seconds, held for 7 minutes and returned to room temperature over 2.5 minutes (viii).

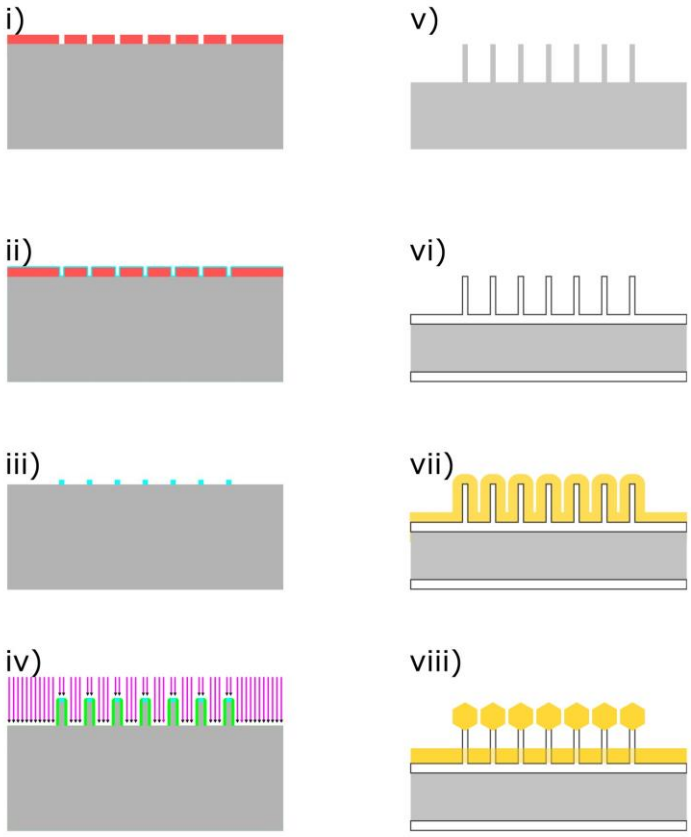

Figure B1. Fabrication and reflow of SERS substrates. (i) E-beam patterning to define negative of mask design. (ii) Reactive sputtering of Al2O3. (iii) Al2O3 mask pattern after lift-off. (iv) Pseudo-Bosch etching to define pillars. (v) Vertical silicon pillars (vi) Thermal oxidation to produce glass pillars. (vii) Sputter deposition of gold layer. (viii) Thermal reflow in RTA forms final structures.

B.2 Enhancement Factor Calculation

When comparing SERS substrates with varying geometries the definition of the most informative "Enhancement Factor" (EF), (and the methodology used to calculate it) is frequently a point of confusion. To provide the maximum clarity and transparency with

respect to our EF calculations we have provided a theoretical derivation of our definition of both the SERS substrate enhancement factor (SSEF) and the analytic enhancement factor (AEF), including any simplifying assumptions we have made. While the definition of the AEF is straightforward[4] our calculation of the SSEF required a combined approach that used our experimentally collected spectra (both SERS and bulk Raman) as well as geometric parameters calculated from finite difference time domain (FDTD) modeling of our nanobulb arrays.

Thiophenol was chosen as a molecular probe to test the SERS enhancement – representative SERS and neat spectra are shown in **Figure B2** along with a table of peak and symmetry assignments. We defined and calculated four enhancement factors at specific peaks, corresponding to known vibrational modes, present in both the SERS and bulk Raman spectra. These four EFs were the SSEF calculated from the area under corresponding peaks ($SSEF_{AREA}$), the SSEF calculated from the peak intensity at corresponding peaks($SSEF_{PKCTS}$), the AEF calculated from the area under corresponding peaks(AEF_{AREA}), and the AEF calculated from the peak intensity at corresponding peaks(AEF_{PKCTS}).

Figure B2 lists spectral locations of peaks found in the SERS spectrum along with their corresponding Wilson notation and symmetry. Included are a set of sum tones seen in the SERS signal only.

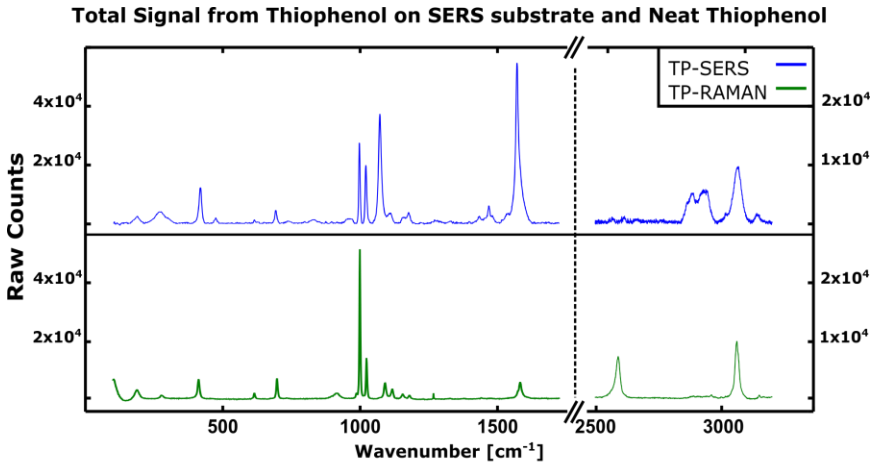

Wavenumber [cm-1]	Wilson Notation	Symmetry Type	Assignment
186	10b	B1	γ(C-S)
271	NA	NA	ν(Au-S)
417	7a	A1	ν(C-S)+β(C=C)
473	16b	B1	γ(C=C)
615	6b	B2	β(C=C)+ν(C-S)
693	6a	A1	β(C=C)+ν(C-S)
739	11	B1	γ(C-H)
830	10a	A2	γ(C-H)
897	17b	B2	γ(C-H)
959	17a	A2	γ(C-H)
998	12	A1	β(C=C)
1022	18a	A1	β(C-H)
1073	1	A1	ν(C=C)
1159	15	B2	β(C-H)
1178	9a	A1	β(C-H)
1280	3	B2	β(C-H)
1330	14	B2	ν(C=C)
1436	19b	B2	ν(C=C)
1471	19a	A1	ν(C=C)
1574	8a	A1	ν(C=C)
3059	2	A1	ν(C-H)

Wavenumber [cm-1]	Wilson Notation	Symmetry Type	Assignment
1110	7a+6a	A1	417+693
1757	6b+15	B2	615+1159
2247	15x2	B2	1159x2
2543	12+8a	A1	998+1574
2595	3+14	B2	1280+1330
2643	1+8a	A1	1073+1574
2870	19bx2	B2	1436x2
2915	19ax2	A1	1471x2
3005	19a+8a	A1	1471+1574
3139	8ax2	A1	1574x2

Figure B2. Measurement of thiophenol adsorbed on nanobulb arrays. Comparison of volume Raman signal (green) and SERS signal (blue). Below are assignments for peaks observed in the SERS spectrum. The peaks listed on the right are the harmonics or sum tones.

B.2.1 Theoretical Approach - AEF

The analytic enhancement factor (AEF) was calculated following the method given in Le Ru *et. al.* (2007).[4] We consider two situations; a volumetric analyte solution with a concentration c_{RS} which provides a bulk Raman signal I_{RS}, and a SERS substrate with an analyte concentration c_{SERS} which produces a signal I_{SERS}. Provided that these

signals are collected under similar experimental conditions (same objective lens, spectrometer, etc.)[4] the AEF is defined as:

$$\text{AEF} = \frac{I_{SERS}/c_{SERS}}{I_{RS}/c_{RS}}. \quad (1)$$

This is not a particularly useful definition when attempting to compare surface and volume signals as in the case of the surface the concentration is not well defined. Without having to focus on the details of the contribution to the EF from substrate geometry, a slightly more useful definition for the AEF that can better compare a signal from a surface to one from a bulk volume is:

$$\text{AEF} = \frac{I_{SERS}/N_{SERS}}{I_{RS}/N_{RS}}, \quad (2)$$

where the N are the number, rather than concentration, of probe molecules that contribute to the signal.

In our case N_{RS} is $c_{RS} \times V_{RS}$ where the volume is given by the focal paraboloid. To define N_{SERS} we note that the bulbs constitute the surfaces that contribute to the enhanced signal, therefore if we assume equal contribution from each bulb within the laser spot (an assumption treated in detail in the SSEF section), and an equal contribution over the surface area of a single bulb, we can define N_{SERS} as $N_{BULB} \times \mu_{SERS} \times A_{BULB}$, where the terms represent the number of bulbs in the laser spot, the areal density of thiophenol adsorbed on the bulbs, and the surface area of a single bulb, respectively. Note that the assumption of equal contribution to the signal from the entire bulb surface area is certainly not true (as shown in the SSEF section), however it does allow us to ignore the details of the specific substrate geometry and calculate an enhancement factor purely from experimental results. Finally, although we collected both the bulk and SERS signal

using the same lens and focus conditions, signal saturation considerations required us to decrease the power used when performing the SERS measurement requiring the addition of scaling terms P_{SERS} and P_{RS}. Adding these terms to equation 2 yields the following formula for the AEF:

$$\text{AEF} = \frac{I_{SERS}/(N_{BULB} \times \mu_{SERS} \times A_{BULB} \times P_{SERS}}{I_{RS}/(c_{RS} \times V_{RS} \times P_{RS})} \quad (3)$$

which can be calculated from experimental parameters alone.

B.2.2 Theoretical Approach - SSEF

To calculate our SERS substrate enhancement factor (SSEF) we have to link our experimental data to simulated parameters in order to characterize the unique substrate geometry of the nanobulbs. This is done through the following theoretical approach, which is an extension of the derivation found in Le Ru *et. al.* (2007).[4] We start with the representation of the SERS enhancement factor for a single molecule (SMEF) in terms of the Raman cross section,

$$\sigma_{SERS} = \text{SMEF} \times \sigma_{RS}. \quad (4)$$

In this case SMEF is defined as the ratio between the intensity collected from a single molecule via SERS and the intensity collected from standard Raman spectroscopy, where the Raman intensity is averaged over all possible molecular orientations (as in a solution): $SMEF = \frac{I_{SERS}^{SM}}{\langle I_{RS}^{SM} \rangle}$. Expressing the single molecule SERS intensity in terms of a differential cross section gives the following:

$$I_{SERS}^{SM} = \frac{\mathrm{d}\sigma_{SERS}}{\mathrm{d}\Omega} S_o \delta\Omega \quad (5)$$

which can be rewritten using equation 4 as:

$$I_{SERS}^{SM} = \lfloor \mathrm{SMEF} \rfloor \frac{\mathrm{d}\sigma_{RS}}{\mathrm{d}\Omega} S_o \delta\Omega \tag{6}$$

where S_o is the input laser intensity and $\delta\Omega$ is the collection solid angle. Here [SMEF] is taken to be the orientation averaged SMEF – in our case we make our first assumption that the monolayer of thiophenol is attached in a single orientation on the nanobulb surface with respect to the enhanced electric field, collapsing the averaging to a single case. Previous theoretical and experimental work indicates that while there is some debate over the specific orientation on the surface[5–8] the covalent nature of the gold-thiol bond ensures that the orientation is regular over the surface.

As the FDTD simulation shown in the main text and the one shown below in **Figure B3**, the SMEF is strongly dependent on the position of the molecule on the bulb surface; in general we can write *SMEF* = *SMEF*(**r**). From Le Ru *et. al.*(2007)[4] we introduce the definition of the SSEF as:

$$SSEF = \frac{1}{A_{laser}} \int_{A_{laser}} SMEF(\bar{\mathbf{r}}) \mathrm{d}S \tag{7}$$

To link this relationship to a measurement, we define the contribution to an experimentally collected spectrum from a single point on the nanobulb surface to the SMEF as follows:

$$I(\bar{\mathbf{r}}) = SMEF(\bar{\mathbf{r}}) \frac{\mathrm{d}\sigma_{RS}}{\mathrm{d}\Omega} S(\rho) \delta\Omega \tag{8}$$

Note that this is the orientation averaged SMEF, (brackets omitted for clarity), and this representation additionally takes into account the intensity variation of laser over the excitation spot as $S(\rho)$.

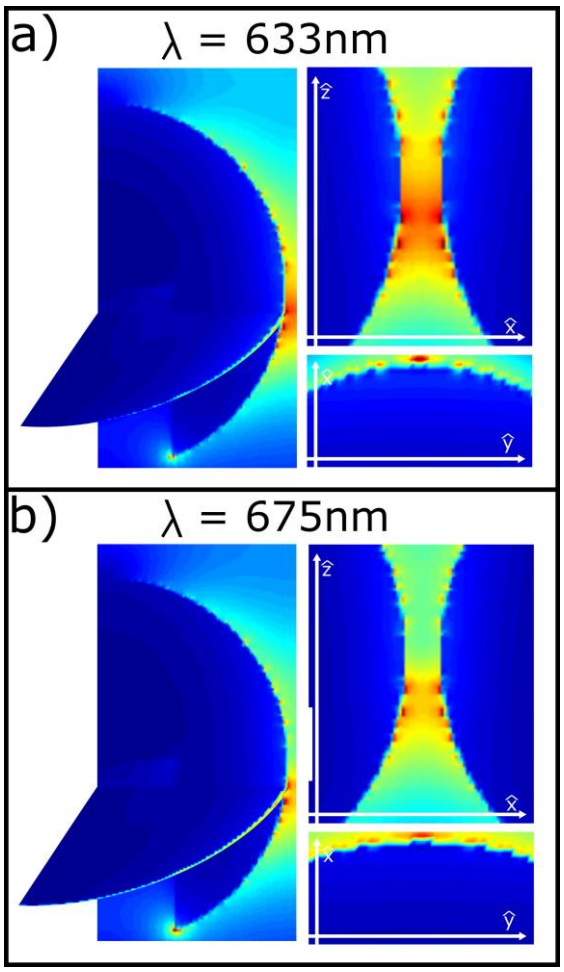

Figure B3. FDTD simulated field profiles for a representative set of bulbs (400 nm period, 10 nm gap). (a) Excitation field profile at 633nm. (b) Emission field profile, simulated at 675 nm which corresponds to a 1000 cm^{-1} wavenumber shift. Insets show details of the field profile in the gap between the bulbs

From equation 8 it is clear that in order to relate I(**r**) to our experimental results we have to obtain the spatial distribution of SMEF(**r**). We can estimate this distribution through the use of our FDTD simulation. The FDTD simulation was performed using the freely available MEEP software package.[9] The Lorentz-Drude model was used to describe the permittivity of the Au structures[10] tailored for accuracy in the 1.24-2.48eV (500-1000 nm) range. Parameters describing the substrate (e.g. bulb diameter, height, spacing, etc.) were obtained from SEM analysis of the specific substrate used to collect

the data presented below. The incident laser excitation was modeled as a linearly-polarized plane wave at 633 nm. Simulations were also performed with excitation at 675 nm and 724 nm to calculate the local field enhancement at 1000 cm^{-1} and 2000 cm^{-1} wavenumber shifts, respectively. Further simulation was also done with a plain Au surface to double check the lack of field enhancement in the absence of nanostructures.

We can use the field profiles calculated via FDTD simulation to directly find the SMEF – previous theoretical treatments[11] have shown that the SMEF from a SERS substrate is a function of the local electric field enhancement at both the incident and emitted wavelengths:

$$SMEF(\bar{\mathbf{r}}, \lambda_I, \lambda_E) \approx \frac{|E(\bar{\mathbf{r}}, \lambda_I)|^2}{|E_{inc}|^2} \cdot \frac{|E(\bar{\mathbf{r}}, \lambda_E)|^2}{|E_{inc}|^2} \tag{9}$$

where the increased local field intensity stems from the nanostructured metal surface. Depending on the mode profile, for small wavenumber shifts, $|E(\mathbf{r},\lambda_I)|^2 \sim |E(\mathbf{r},\lambda_E)|^2$ and the traditional $|E(\mathbf{r})|^4$ scaling of the SMEF is obtained. As mentioned earlier, however, we decided to explicitly calculate the field enhancement at 1000 and 2000 cm^{-1} wavenumbers to ensure the SSEF remains high across several peaks specific to thiophenol.

Several cross-sections of the simulated mode profile on the the nanobulb surface at 633 nm excitation and 675 nm emission is shown in **Figure B3** (note the overlap in local field enhancement between 633 and 675 nm). It is clear that the SMEF is highly anisotropic on the bulb surface, a fact that must be taken into account when calculating both I(**r**) and the SSEF. To help relate these two quantities and simplify equation 8 we have the following relationship from Le Ru *et. al.* (2007),[4]

$$I_{RS} = c_{RS} V_{RS} \frac{\mathrm{d}\sigma_{RS}}{\mathrm{d}\Omega} P_{RS} \delta\Omega \tag{10}$$

which gives the Raman signal intensity (I_{RS}) of a bulk solution of the probe molecule at a concentration c_{RS} collected with power P_{RS} and a focal paraboloid of V_{RS}. Applying the above relationship to equation 8 we obtain:

$$I(\bar{\mathbf{r}}, \lambda_I, \lambda_E) = SMEF(\bar{\mathbf{r}}, \lambda_I, \lambda_E) S(\rho) \left(\frac{I_{RS}}{c_{RS} V_{RS} P_{RS}} \right) \tag{11}$$

This simplification is valid only because we collected both the bulk Raman and SERS spectra using the same lens, geometry, and focus conditions – ensuring that the collected solid angle $\delta\Omega$ was equal in both cases. Now we integrate I(**r**) from equation 11 over the laser spot:

$$\int_{spot} I(\bar{\mathbf{r}}, \lambda_I, \lambda_E) \mathrm{d}S = \left(\frac{I_{RS}}{c_{RS} V_{RS} P_{RS}} \right) \times \int_{spot} SMEF(\bar{\mathbf{r}}, \lambda_I, \lambda_E) S(\rho) \mathrm{d}S \tag{12}$$

where the term on the left is just the experimentally collected SERS signal I_{SERS}. To aid in simplifying equation 12 we make the following assumptions: 1) The laser spot is larger than a single nanobulb, and therefore the total collected signal comes from more than one nanobulb. 2) The laser intensity within the spot is considered to be constant at an average intensity such that the total power is conserved (ie. a rectangular rather than gaussian beam profile). 3) The contribution from identical points on different bulbs is considered to be equal within the laser spot. A schematic of these assumptions is given in **Figure B4**. The first assumption is shown to be true based on our measurement of the beam diameter and nanobulb spacing. The diameter of the laser spot was calculated to be approximately 2.8μm using the "knife-edge" measurement method[4,12] and the representative nanobulb

substrate had a center to center nanobulb spacing of approximately 400nm with an average edge to edge gap of 10nm. Although the excitation and collection efficiency within the spot are not uniform (assumptions 2 and 3) the fact that the signal strength is roughly uniform when measured over an entire ($L \geq 35\mu m$) square array of nanobulbs lets us treat each bulb as equal. Therefore, the combined effect of the decreasing collection/excitation efficiency near the edge of the laser spot can be thought of as simply scaling down the effective *number* of bulbs within the laser spot. In such a model the number of bulbs within the disk defined by the beam diameter would be the upper bound of the number of contributing bulbs. By choosing this number as the effective number of bulbs within the laser spot we will overestimate the contribution from each bulb and therefore underestimating the total enhancement factor.

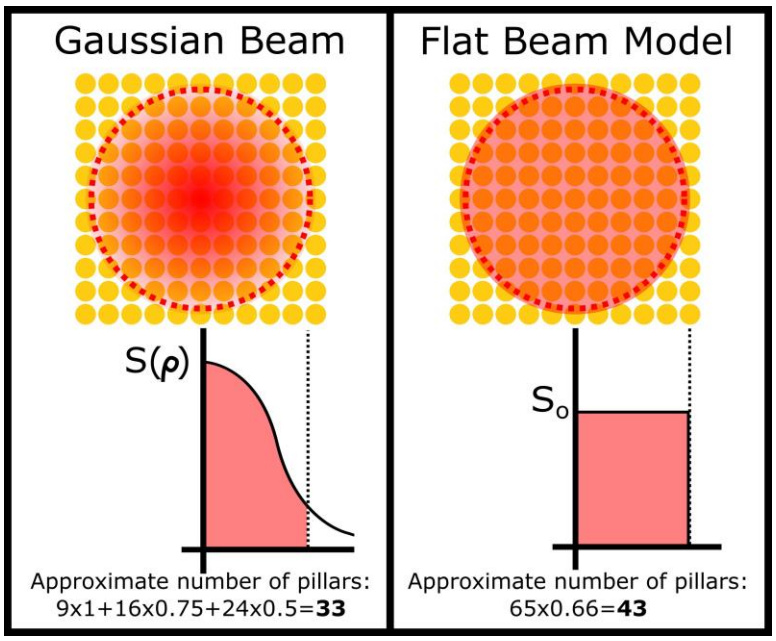

Figure B4. Schematic of assumptions used for SSEF estimation. The Gaussian beam profile is approximated as a uniform beam with an intensity given by the laser power divided by beam area. Both the excitation and collection efficiency from individual bulbs found within this beam diameter is assumed to be 100%. This assumption underestimates the SSEF as it overestimates the number of bulbs that contribute to the total signal.

This makes assumptions 2 and 3 reasonable as this allows for the calculation to be considered a "conservative" estimate, or "lower bound" of the enhancement factor. Using the above two assumptions (ie. integrating the SMEF over one bulb and summing this result over the total number of bulbs in the laser spot) equation 12 can be simplified to:

$$I_{SERS} = \left(\frac{I_{RS}}{c_{RS} V_{RS} P_{RS}}\right) \times \sum_{\#\ bulbs} \int_{bulb} SMEF(\bar{\mathrm{r}}, \lambda_I, \lambda_E) S_o \mathrm{d}S, \tag{13}$$

where S_o is the average laser intensity on a single nanobulb. Based on the measured uniformity of the enhancement factor (shown in the main text) the summation can be replaced with a multiplication by the N_{bulbs} in the laser spot. For a fixed areal density

(μ_{SERS}) of the thiophenol probe molecule on the bulb surface and expanding SMEF in terms of equation 9 the above equation simplifies to:

$$I_{SERS} = \left(\frac{I_{RS}}{c_{RS}V_{RS}P_{RS}}\right) \times N_{bulbs} \times \int_{bulb} S_o \cdot \mu_{SERS} \cdot \frac{|E(\bar{\mathbf{r}}, \lambda_I)|^2}{|E_{inc}|^2} \cdot \frac{|E(\bar{\mathbf{r}}, \lambda_E)|^2}{|E_{inc}|^2} \mathrm{d}S, \tag{14}$$

We define the term $SSEF_{MAX}$ at $\mathbf{r} = \mathbf{r_o}$ to be:

$$SSEF = SMEF_{MAX} = \frac{|E(\mathbf{r_o}, \lambda_I)|^2}{|E_{inc}|^2} \cdot \frac{|E(\mathbf{r_o}, \lambda_E)|^2}{|E_{inc}|^2} \tag{15}$$

allowing us to write equation 14 as:

$$I_{SERS} = \left(\frac{I_{RS}}{c_{RS}V_{RS}P_{RS}}\right) N_{bulbs} \cdot P_{SERS} \cdot \mu_{SERS} \cdot SSEF \times \int_{bulb} \frac{|E(\bar{\mathbf{r}}, \lambda_I)|^2}{|E(\mathbf{r_o}, \lambda_I)|^2} \cdot \frac{|E(\bar{\mathbf{r}}, \lambda_E)|^2}{|E(\mathbf{r_o}, \lambda_E)|^2} \mathrm{d}S \tag{16}$$

The right-most term is an effective surface area (A_{eff}), based on the weighted contribution from the spatial and wavelength dependence of the electric field enhancement and is calculated directly from a point by point convolution of the field distributions obtained using the FDTD simulations. Rearranging the terms we can write:

$$SSEF(\lambda_I, \lambda_E) = \frac{I_{SERS}/(N_{bulbs}\mu_{SERS}P_{SERS}A_{eff})}{I_{RS}/(c_{RS}V_{RS}P_{RS})}. \tag{17}$$

where each term on the right hand side of the equality is an parameter set during the experiment, directly measured during the experiment, or computed via FDTD simulation.

B.2.3 Calculated AEF and SSEF

Calculated AEF and SSEF values for 16 specific peaks are given in **Figure B5**. Enhancement factors for each peak were calculated based on the maximum peak intensity as well as peak area for comparison. (Peak area was obtained by fitting Lorentzian curves to each peak in both the SERS and bulk Raman spectra.) Note that this necessitated that well-defined peaks, corresponding to identical vibrational modes, be found in both the

SERS and bulk spectra. The two peaks marked with asterisk had uncertain bulk Raman peak parameters. The average SSEF over all peaks, based on peak area was 1.3×10^{10} and based on peak intensity was 9×10^{9}. The average AEF based on both peak area and intensity was approximately 2×10^{8}.

Wavenumber [cm^{-1}]		SSEF		AEF		Mode Properties	
SERS	Raman	Peak Area	Peak intensity	Peak Area	Peak intensity	Wilson Number	Symmetry
186.4	188.62	3.57E+09	1.77E+09	7.64E+07	3.79E+07	10b	B1
417.54	412.79	5.05E+09	3.55E+09	1.12E+08	7.87E+07	7a	A1
615.16	615.9	2.99E+09	1.48E+09	6.82E+07	3.38E+07	6b	B2
693.11	698.31	1.66E+09	1.17E+09	3.83E+07	2.70E+07	6a	A1
739.41	733.25	2.18E+10	7.75E+09	5.06E+08	1.80E+08	11	B1
897.24*	898.06	6.68E+08	1.63E+09	1.59E+07	3.88E+07	17b	A2
961.06*	916.33	1.93E+09	1.77E+09	4.63E+07	4.23E+07	17a	B2
998.37	999.88	1.22E+09	9.96E+08	2.94E+07	2.40E+07	12	A1
1022.2	1024.4	3.22E+09	2.71E+09	7.71E+07	6.50E+07	18a	A1
1073.3	1091.7	1.04E+10	1.16E+10	2.46E+08	2.75E+08	1	A1
1110.7	1117.7	2.59E+09	1.58E+09	6.10E+07	3.71E+07	7a+6a	A1
1159.2	1156	5.39E+09	2.40E+09	1.26E+08	5.60E+07	15	B2
1178	1180.3	1.08E+10	5.46E+09	2.51E+08	1.27E+08	9a	A1
1280.1	1268.5	3.46E+10	6.19E+09	7.86E+08	1.41E+08	3	B2
1330	1327.8	2.18E+10	6.36E+09	4.90E+08	1.43E+08	14	B2
1436	1442.1	1.87E+10	1.35E+10	4.12E+08	2.98E+08	19b	B2
1471.4	1474.2	5.11E+10	6.32E+10	1.11E+09	1.38E+09	19a	A1
1574.4	1583.4	2.20E+10	1.82E+10	4.69E+08	3.87E+08	8a	A1
3059.8	3057.5	2.19E+09	1.10E+09	4.21E+07	2.12E+07	2	A1

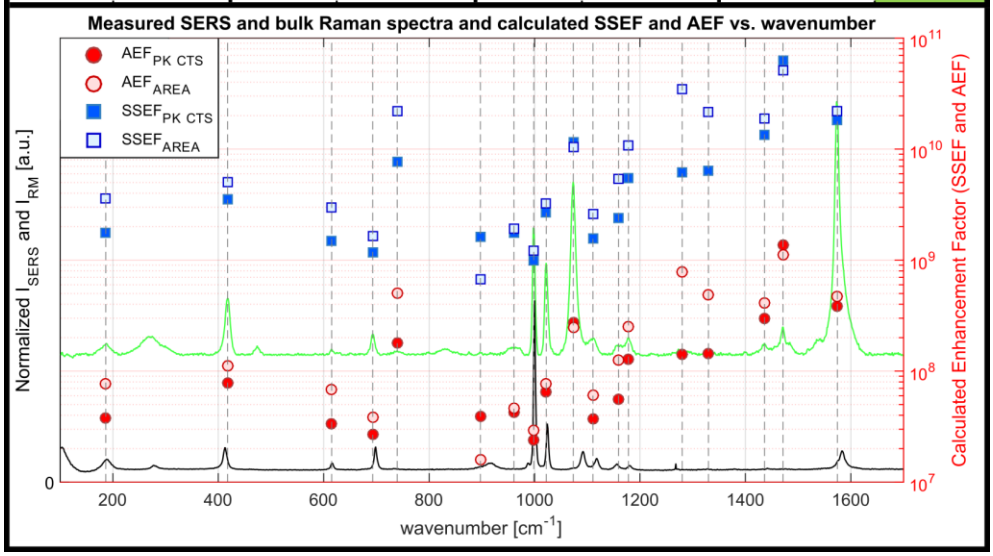

Figure B5. Calculated SSEF and AEF based on peak area and maximum intensity. Note that these values were calculated for peaks that were well defined in both the SERS and bulk Raman spectra. The average SSEF over all peaks, based on peak area was 1.3×10^{10} and based on peak intensity was 9×10^{9}. The average AEF based on both peak area and intensity was approximately 2×10^{8}.

B.3 Tracheal Cytotoxin Peak Assignment

The tables in **Figures B6** and **B7** contain assignments of the peaks seen in the TCT spectra presented in the main text. Peaks of interest that stem from identical features but are shifted due to hydrogen bonding are highlighted with the same color to aid in comparing the wet and dry spectra.

wavenumber [cm^{-1}]	Key Structure(s)	Component	Name	Mode	Note
168	NAG/NAM	N-ACETYL	Acetyl torsion (N)	τ(CN)+τ(NC)	
250	NAG/NAM	N-ACETYL	Acetyl torsion and deformation	$\tau(CCH_3)+\delta$(CNC)	
322	NAG/NAM	RING	3 atom CCC ring deformation	δ(CCC)	
403	NAG/NAM	CC(OH)	3 atom CCO exocyclic deformation	δ(CCO) - EXO	
450/470/482.5	NAG/NAM	RING	3 atom CCO endocyclic deformation	δ(CCO) - ENDO	450-pyranose, 470-furanose
500	β(1-4') GLY	NAG-O-NAM	Glycosidic link deformation	$\delta(CO_2C)$ - EXO	Between NAG-NAM
554	NAM	LAC AC	Lactic acid ether deformation	δ(COC) - EXO	Between NAM-LAC
593	NAG/NAM	RING	Endocyclic COC deformation	δ(COC) - ENDO	Endocyclic ether deformation
636	NAG/NAM/GLU/DAP/ALN	N-ACETYL/LAC	Acetyl and carboxylic acid carbonyl out of plane deformation	δ(NC=O)/δ(CC=O)	
704	β(1-4') GLY	NAG-O-NAM	Glycosidic link torsion	$\tau(CO_2)$	Torsion around glycosidic link
722	GLU/DAP	CH2	Methylene rocking	$\delta_{ROCK}(CH_2)$	
742	NAG/NAM	CHOH-2nd	Torsion around COH bon	τ(COH)	
757	NAM	COOH	Carbonyl in plane bending of lactic acid group	β(C=O)	
792	GLU/DAP/ALN	COOH	Carboxylic acid carbonyl in plane bending	β(C=O)	C=O in plane bending
807/818	NAG/NAM	RING	Endocyclic symmetric COC stretch (6 member ring)	ν_s(C-O-C)	For 6-member rings
835	ALN/ALY	CH3	Methyl group stretching	ν(C-CH_3)	
842	β(1-4') GLY	NAG-O-NAM	Glycosidic link symmetric stretching	ν_s(C-O_G-C)	β(1-4') glycosidic link, symmetric stretch
880	NAG/NAM/ALY/GLU/DAP/ALN	SKEL	Amide skeletal stretch	ν(R'C-NR)	Backbone amide stretch
936	NAM	RING	Endocyclic symmetric COC stretch (5 member ring)	ν_s(C-O-C)	For 5-member rings
982	GLU/DAP/ALN	COOH	Carboxylic acid out of plane deformation	δ_{OOP}(COOH)	Out of plane carboxyl group deformation
1018	NAG/NAM	RING	Ring based secondary alcohol C-O stretch	ν(C-OH)	Aliphatic ring secondary alcohols
1031	DAP	NH2	CN stretch of primary amine	ν(CN)	Primary amine CN stretch blue shifted by H+ bonding
1078	NAM	ANH RING	Endocyclic asymmetric COC stretch (5 member ring)	ν_a(C-O-C)	5 member ring, asymmetric glycoside stretch
1125	NAG/NAM	RING	Endocyclic asymmetric COC stretch (6 member ring)	ν_a(C-O-C)	6 member ring, asymmetric glycoside stretch
1138	NAM	LAC AC	NAM to lactic acid ether link, asymmetric glycoside vibration	ν_a(C-O-C)	NAM ether link to lactic acid
1159	β(1-4') GLY	NAG-O-NAM	Glycosidic link asymmetric stretching	ν_a(C-O_G-C)	β(1-4') glycosidic link, asymmetric stretch
1220-1260	GLU/DAP+DAP/ALN+LAC/ALY+ALY/GLU	AMIDE	Amide III - chain, trans	ν(CN)+β(NH)	Amide III, in phase combination of CN stretch and NH in plane bending (for trans amino acids)
1285	GLU/DAP	CH2	Methylene twisting	$\delta_{TWIST}(CH_2)$	
1326(sh)	NAG/NAM (ACE)	N-ACETYL	Amide III - acetyl/cis form	ν(CN)+β(NH)	Amide III, in phase combination of CN stretch and NH in plane bending (for cis acetyl group)
1339	NAG/NAM	CHOH-2nd	Secondary alcohol OH in plane bend	β(OH)	Present on ring
1354	GLU/DAP/ALN	COOH	Carboxylic acid in plane OH bend (monomer)	β(OH)	Protonated carboxylic acid OH in plane bending
1379	NAG/NAM	N-ACETYL/CH3	Symmetric methyl group deformation	$\delta_s(CH_3)$	Umbrella mode for CH3 symmetric deformation (N-Acetyl Group)
1399	ALN/ALY	PEPT/CH3	Symmetric methyl group deformation	$\delta_s(CH_3)$	Umbrella mode for CH3 symmetric deformation (Peptide Mode)
1435	NAG/NAM/ALN/ALY	N-ACETYL/CH3	Asymmetric methyl group deformation	$\delta_a(CH_3)$	Degenerate mode for CH3 asymmetric deformation
1480-1490	GLU/DAP	CH2	Methylene scissoring	$\delta_{SCI}(CH_2)$	Scissoring mode for glu/dap chains of $(CH2)_x$
1539	NAG/NAM	N-ACETYL	Amide II - Acetyl	ν(CN)-β(NH)	Amide II, out of phase combination of CN stretch and NH in plane bending
1572	LAC/ALY+ALY/GLU+GLU/DAP+DAP/ALN	AMIDE	Amide II - Peptide chain	ν(CN)-β(NH)	Amide II, out of phase combination of CN stretch and NH in plane bending
1602	DAP	NH2	NH2 scissoring	$\delta_{SCI}(NH_2)$	
1620	NAM (ACE)	N-ACETYL	Amide I - Acetyl	ν(C=O)-ν(CN)- δ(CCN)-β(NH)	Amide I, C=O stretch with small contribution from out of phase CN stretch, CCN deformation, and NH bending
1635	NAG (ACE)	N-ACETYL	Amide I - Acetyl	ν(C=O)-ν(CN)- δ(CCN)-β(NH)	Amide I, C=O stretch with small contribution from out of phase CN stretch, CCN deformation, and NH bending
1650-1680	LAC/ALY+ALY/GLU+GLU/DAP+DAP/ALN	AMIDE	Amide I - Peptide chain	ν(C=O)-ν(CN)- δ(CCN)-β(NH)	Amide I, C=O stretch with small contribution from out of phase CN stretch, CCN deformation, and NH bending
1704	DAP/ALN	COOH	Carboxylic acid - C=O stretch, end of chain	ν(C=O)	Carboxylic acid C=O stretch, influenced by chain length
1719	GLU	COOH	Carboxylic acid - C=O stretch, middle of chain	ν(C=O)	Carboxylic acid C=O stretch, influenced by chain length
2110	KETENE	C=C=O	Ketene asymmetric stretch	ν_a(C=C=O)	Ketene from plasmonically reduced carboxylic acid group, asymmetric stretch

Figure B6. Peaks for 100nM dry TCT spectrum. Abbreviations: NAG: N-Acetyl Glucosamine, NAM: N-Acetyl Muramyl, ALYL: Alanyl, GLU: Glutamine, DAP: Diaminopimelic acid, ALN: Alanine, GLY: Glycoside link $\beta(1–4)$. Vibrations: δ: Out of plane deformation, β: In plane bending, ν: Stretching +: In phase, -: Out of phase.

wavenumber [cm^{-1}]	Key Structure(s)	Component	Name	Mode	Note
168	NAG/NAM	N-ACETYL	Acetyl torsion (N)	τ(CN)+τ(NC)	
250	NAG/NAM	N-ACETYL	Acetyl torsion and deformation	$\tau(CCH_3)$+δ(CNC)	
322	NAG/NAM	RING	3 atom CCC ring deformation	δ(CCC)	
403	NAG/NAM	CC(OH)	3 atom CCO exocyclic deformation	δ(CCO) - EXO	
450/470/482.5	NAG/NAM	RING	3 atom CCO endocyclic deformation	δ(CCO) - ENDO	450-pyranose, 470-furanose
500	β(1-4') GLY	NAG-O-NAM	Glycosidic link deformation	$\delta(CO_2C)$ - EXO	Between NAG-NAM
554	NAM	LAC AC	Lactic acid ether deformation	δ(COC) - EXO	Between NAM-LAC
593	NAG/NAM	RING	Endocyclic COC deformation	δ(COC) - ENDO	Endocyclic ether deformation
636	NAG/NAM/GLU/DAP/ALN	N-ACETYL/LAC	Acetyl and carboxylic acid carbonyl out of plane deformation	δ(NC=O)/δ(CC=O)	
704	β(1-4') GLY	NAG-O-NAM	Glycosidic link torsion	$\tau(CO_2)$	Torsion around glycosidic link
722	GLU/DAP	CH2	Methylene rocking	$\delta_{rock}(CH_2)$	
742	NAG/NAM	CHOH-2nd	Torsion around COH bon	τ(COH)	
757	NAM	COOH	Carbonyl in plane bending of lactic acid group	β(C=O)	
792	GLU/DAP/ALN	COOH	Carboxylic acid carbonyl in plane bending	β(C=O)	C=O in plane bending
807/818	NAG/NAM	RING	Endocyclic symmetric COC stretch (6 member ring)	ν_s(C-O-C)	For 6-member rings
835	ALN/ALY	CH3	Methyl group stretching	ν(C-CH_3)	
842	β(1-4') GLY	NAG-O-NAM	Glycosidic link symmetric stretching	ν_s(C-O_g-C)	β(1-4') glycosidic link, symmetric stretch
880	NAG/NAM/ALY/GLU/DAP/ALN	SKEL	Amide skeletal stretch	ν(R'C-NR)	Backbone amide stretch
936	NAM	RING	Endocyclic symmetric COC stretch (5 member ring)	ν_s(C-O-C)	For 5-member rings
982	GLU/DAP/ALN	COOH	Carboxylic acid out of plane deformation	δ_{out}(COOH)	Out of plane carboxyl group deformation
1018	NAG/NAM	RING	Ring based secondary alcohol C-O stretch	ν(C-OH)	Aliphatic ring secondary alcohols
1031	DAP	NH2	CN stretch of primary amine	ν(CN)	Primary amine CN stretch blue shifted by H+ bonding
1078	NAM	ANH RING	Endocyclic asymmetric COC stretch (5 member ring)	ν_a(C-O-C)	5 member ring, asymmetric glycoside stretch
1125	NAG/NAM	RING	Endocyclic asymmetric COC stretch (6 member ring)	ν_a(C-O-C)	6 member ring, asymmetric glycoside stretch
1138	NAM	LAC AC	NAM to lactic acid ether link, asymmetric glycoside vibration	ν_a(C-O-C)	NAM ether link to lactic acid
1159	β(1-4') GLY	NAG-O-NAM	Glycosidic link asymmetric stretching	ν_a(C-O_g-C)	β(1-4') glycosidic link, asymmetric stretch
1220-1260	GLU/DAP+DAP/ALN+LAC/ALY+ALY/GLU	AMIDE	Amide III - chain, trans	ν(CN)+β(NH)	Amide III, in phase combination of CN stretch and NH in plane bending (for trans amino acids)
1285	GLU/DAP	CH2	Methylene twisting	$\delta_{twist}(CH_2)$	
1326(sh)	NAG/NAM (ACE)	N-ACETYL	Amide III - acetyl/cis form	ν(CN)+β(NH)	Amide III, in phase combination of CN stretch and NH in plane bending (for cis acetyl group)
1339	NAG/NAM	CHOH-2nd	Secondary alcohol OH in plane bend	β(OH)	Present on ring
1354	GLU/DAP/ALN	COOH	Carboxylic acid in plane OH bend (monomer)	β(OH)	Protonated carboxylic acid OH in plane bending
1379	NAG/NAM	N-ACETYL/CH3	Symmetric methyl group deformation	$\delta_s(CH_3)$	Umbrella mode for CH3 symmetric deformation (N-Acetyl Group)
1399	ALN/ALY	PEPT/CH3	Symmetric methyl group deformation	$\delta_s(CH_3)$	Umbrella mode for CH3 symmetric deformation (Peptide Mode)
1435	NAG/NAM/ALN/ALY	N-ACETYL/CH3	Asymmetric methyl group deformation	$\delta_a(CH_3)$	Degenerate mode for CH3 asymmetric deformation
1480-1490	GLU/DAP	CH2	Methylene scissoring	$\delta_{scis}(CH_2)$	Scissoring mode for glu/dap chains of $(CH2)_n$
1539	NAG/NAM	N-ACETYL	Amide II - Acetyl	ν(CN)-β(NH)	Amide II, out of phase combination of CN stretch and NH in plane bending
1572	LAC/ALY+ALY/GLU+GLU/DAP+DAP/ALN	AMIDE	Amide II - Peptide chain	ν(CN)-β(NH)	Amide II, out of phase combination of CN stretch and NH in plane bending
1602	DAP	NH2	NH2 scissoring	$\delta_{scis}(NH_2)$	
1620	NAM (ACE)	N-ACETYL	Amide I - Acetyl	ν(C=O)-ν(CN)- δ(CCN)-β(NH)	Amide I, C=O stretch with small contribution from out of phase CN stretch, CCN deformation, and NH bending
1635	NAG (ACE)	N-ACETYL	Amide I - Acetyl	ν(C=O)-ν(CN)- δ(CCN)-β(NH)	Amide I, C=O stretch with small contribution from out of phase CN stretch, CCN deformation, and NH bending
1650-1680	LAC/ALY+ALY/GLU+GLU/DAP+DAP/ALN	AMIDE	Amide I - Peptide chain	ν(C=O)-ν(CN)- δ(CCN)-β(NH)	Amide I, C=O stretch with small contribution from out of phase CN stretch, CCN deformation, and NH bending
1704	DAP/ALN	COOH	Carboxylic acid - C=O stretch, end of chain	ν(C=O)	Carboxylic acid C=O stretch, influenced by chain length
1719	GLU	COOH	Carboxylic acid - C=O stretch, middle of chain	ν(C=O)	Carboxylic acid C=O stretch, influenced by chain length
2110	KETENE	C=C=O	Ketene asymmetric stretch	ν_a(C=C=O)	Ketene from plasmonically reduced carboxylic acid group, asymmetric stretch

Figure B7. Peaks for 100nM wet TCT spectrum. Abbreviations: NAG: N-Acetyl Glucosamine, NAM: N-Acetyl Muramyl, ALYL: Alanyl, GLU: Glutamine, DAP: Diaminopimelic acid, ALN: Alanine, GLY: Glycoside link β(1–4). Vibrations: δ: Out of plane deformation, β: In plane bending, ν: Stretching +: In phase, -: Out of phase, BS: Blue-shifted, RS: Red-shifted.

Acknowledgements

This work was supported by the Gordon and Betty Moore Foundation under the MSN156910 grant. The authors would like to thank the Goldman research group at the University of North Carolina for the supply of purified TCT and also the staff of the Kavli Nanoscience Institute for their continued help. B.C.M. and A.R.T. acknowledge support from the Office of Naval Research (Award No. N000141210574) and a DURIP grant (Award No. N000141310655).

Appendix B, in part, is currently being prepared for submission for publication of the material by Brandon C. Marin, † Sameer S. Walavalkar, † Chieh-feng Chang, † Andrea

R. Tao, Axel Shearer, and Scott Fraser. (†Equal contribution) The dissertation author was the primary investigator and author of this material.

References

(1) Henry, M. D.; Walavalkar, S.; Homyk, A.; Scherer, A. Alumina etch masks for the fabrication of high-aspect-ratio silicon micropillars and nanopillars. *Nanotechnology* 2009, 20, 255305.

(2) Walavalkar, S. S.; Hofmann, C. E.; Homyk, A. P.; Henry, M. D.; Atwater, H. A. Scherer, A. Tunable Visible and Near-IR Emission from Sub-10 nm Etched Single-Crystal Si Nanopillars. *Nano Lett*. 2010, 10, 101004110737018.

(3) Walavalkar, S. S.; Latawiec, P.; Homyk, A. P.; Scherer, A. Scalable method for the fabrication and testing of glass-filled, three-dimensionally sculpted extraordinary transmission apertures. *Nano Lett.* 2014, 14, 311–7.

(4) Le Ru, E. C.; Blackie, E.; Meyer, M.; Etchegoin, P. G. Surface Enhanced Raman Scattering Enhancement Factors: A Comprehensive Study. *J. Phys. Chem. C* 2007, 111, 13794–13803.

(5) Polubotko, A. M. Some anomalies of the SER spectra of symmetrical molecules adsorbed on transition metal substrates: Consideration by the dipole-quadrupole SERS theory. *J. Raman Spectrosc.* 2005, 36, 522–532.

(6) Fan, X.; Chi, Q.; Liu, C.; Lau, W. From Nondissociative to Dissociative Adsorption of Benzene-thiol on Au(111): A Density Functional Theory Study. *J. Phys. Chem. C* 2012, 116, 1002–1011.

(7) Joo, T. H.; Kim, K.; Kim, M. S. Surface-enhanced Raman scattering of benzenethiol in silver sol. J. Mol. Struct. 1987, 162, 191–200.

(8) Nara, J.; Higai, S.; Morikawa, Y.; Ohno, T. Density functional theory investigation of benzenethiol adsorption on Au(111). *J. Chem. Phys.* 2004, 120, 6705–11.

(9) Oskooi, A. F.; Roundy, D.; Ibanescu, M.; Bermel, P.; Joannopoulos, J. D.; Johnson, S. G. Meep: A flexible free-software package for electromagnetic simulations by the FDTD method. *Computer Physics Communications* 2010, 181, 687–702.

(10) Vial, A.; Grimault, A.-S.; Macias, D.; Barchiesi, D.; de la Chapelle, M. L. Improved analytical fit of gold dispersion: Application to the modeling of

extinction spectra with a finite-difference time-domain method *Phys. Rev. B* 2005, 71, 085416.

Appendix C

Supporting Information for Chapter 5: SERS-Enhanced Piezoplasmonic Graphene Composite for Biological and Structural Strain Mapping

Brandon C. Marin,[a] Justin Liu,[a] Eden Aklile,[a] Armando D. Urbina,[a] Andrew S-C. Chiang,[a] Natalie Lawrence,[a] Shaochen Chen,[a] and Darren J. Lipomi[a]

[a]NanoEngineering Department, University of California, San Diego. 9500 Gilman Drive MC 0448, La Jolla, CA 92093-0448

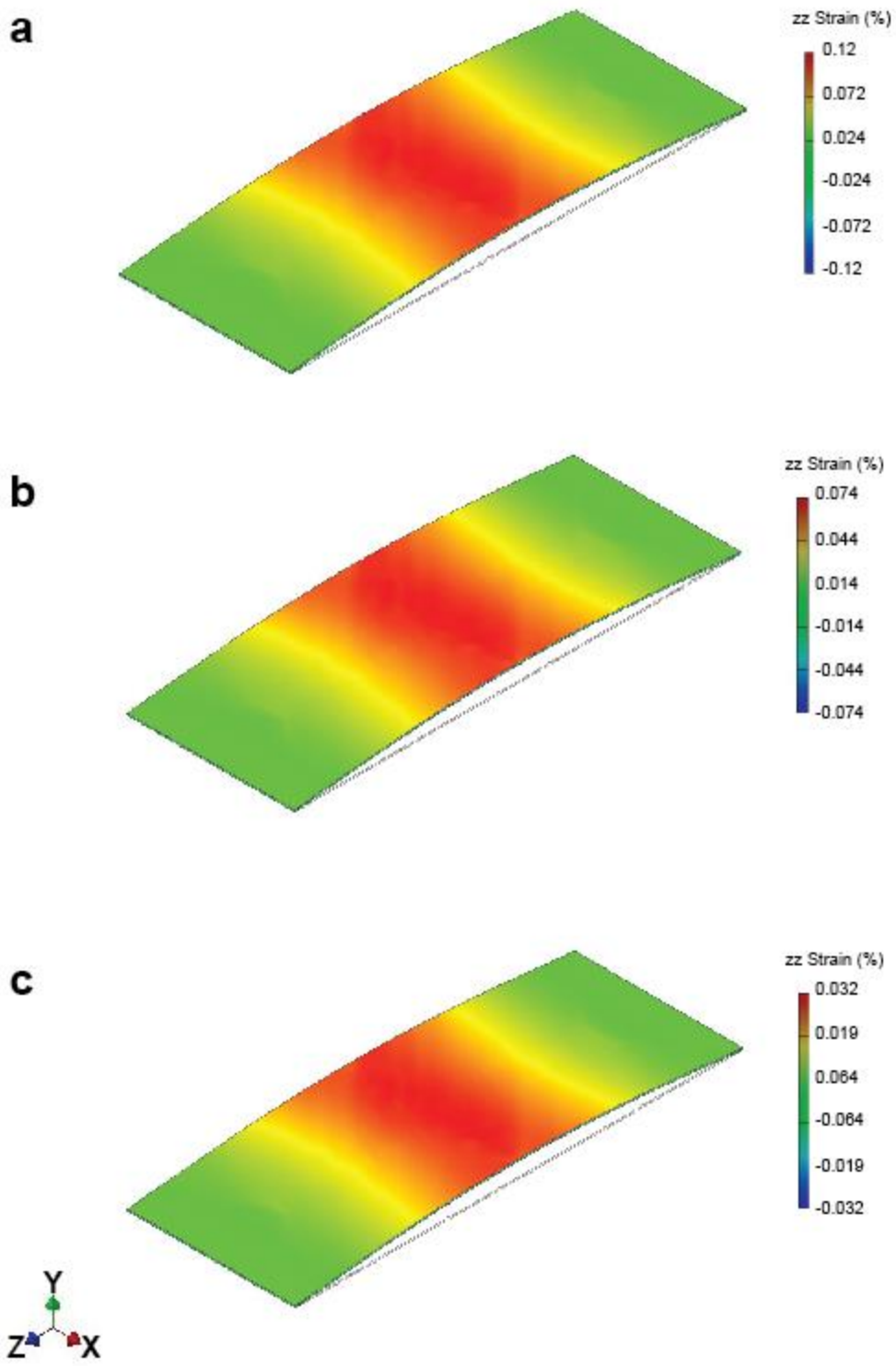

Figure C1. Finite-Element Simulation of Strained Glass slide. The strain distribution (zz-component) of bent 50.8 mm x 19.05 mm x 0.20 mm glass slides is depicted. The strain at the apex (in y-direction) of the glass slides is 0.12 % (a), 0.074 % (b), and 0.032 % (c). Note that direction orthogonal to the glass slide is defined as the y-direction.

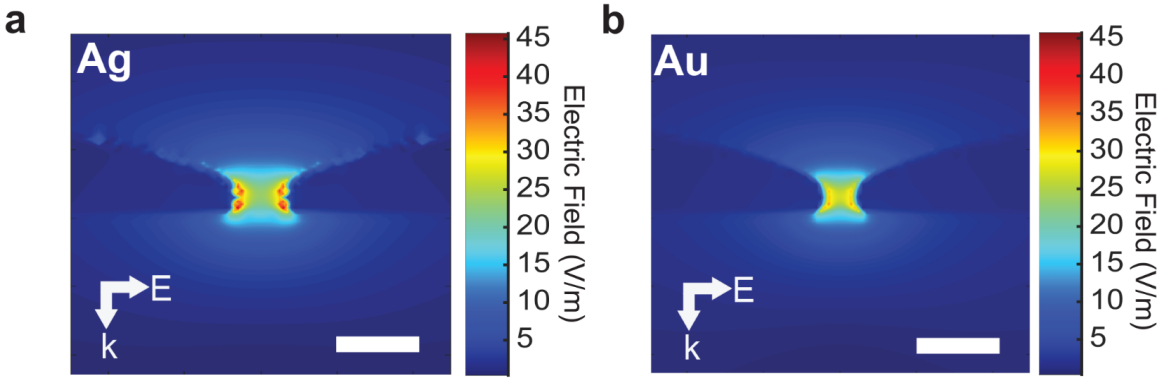

Figure C2. Two-dimensional finite-difference time-domain (FDTD) simulations of gaps between noble metal nanoislands. The electric field magnitude is plotted in 2D space for silver (a) and gold (b) nanoislands with a 5 nm gap under 633 nm excitation. Nanoislands are on a 3-Å thick monolayer of graphene supported by silica. Scale bars are 10 nm. The polarization and propagation of incident light is defined by the white arrows. The simulated nanoisland shape was approximated by SEM and TEM images.

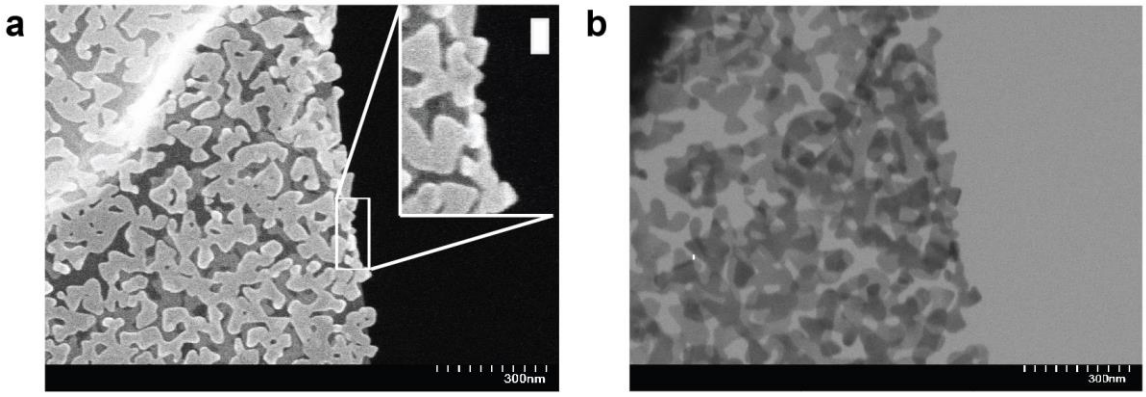

Figure C3. Scanning/Transmission Electron Micrographs of Gold Nanoislands. Electron micrographs of folded over gold nanoisland on graphene film are depicted in scanning (a) and transmission (b) modes. The samples are free standing on a TEM copper grid and only supported by the graphene monolayer. The inset in a) depicts the side profile of metal nanoislands (scale bar 20 nm).

Table C1. Strain Values along Length of Glass Slides. Strain values as a function of distance from the apex are depicted as obtained from finite-element simulations. Slides A, B, and C correspond to slides with a maximal strain of 0.12, 0.072, and 0.032 %, respectively.

z-distance from apex (mm)	Slide A zz-Strain (%)	Slide B zz-Strain (%)	Slide C zz-Strain (%)
0.00	0.11790	0.07272	0.03150
0.25	0.11740	0.07239	0.03131
0.50	0.11640	0.07176	0.03103
0.75	0.11540	0.07114	0.03076
1.00	0.11460	0.07068	0.03057
1.25	0.11410	0.07034	0.03042
1.50	0.11330	0.06985	0.03021
1.75	0.11230	0.06926	0.02995
2.00	0.11140	0.06873	0.02972
2.25	0.11060	0.06823	0.02951
2.50	0.11020	0.06796	0.02390
2.75	0.10980	0.06770	0.02928
3.00	0.10920	0.06734	0.02912
3.25	0.18500	0.06694	0.02895
3.50	0.10790	0.06654	0.02878
3.75	0.10680	0.06589	0.02885
4.00	0.10580	0.06529	0.02240
4.25	0.10480	0.06468	0.02797
4.50	0.10360	0.06391	0.02764
4.75	0.10230	0.06308	0.02728
5.00	0.10090	0.06226	0.02692

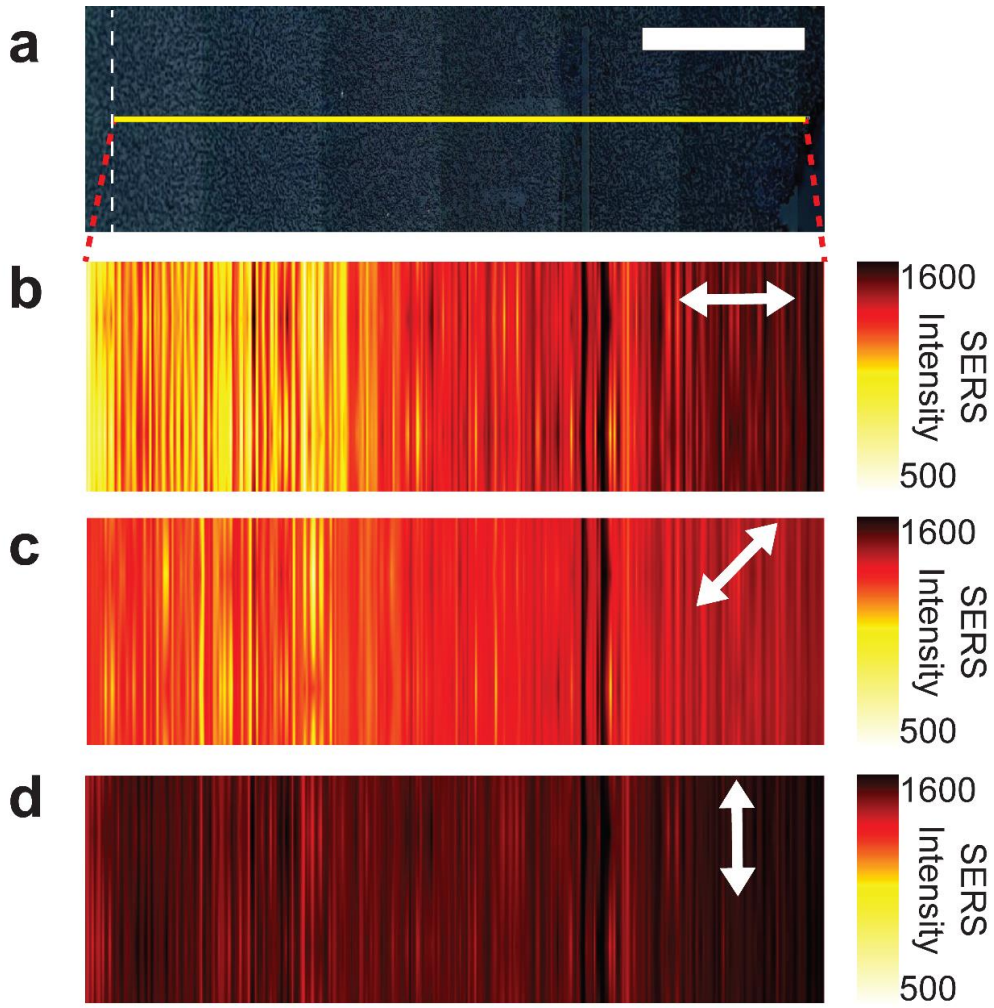

Figure C4. 2D Raman mapping of strain gradients using a bent glass substrate bearing silver nanoislands on graphene. A bright-field image (a) of AgNIs on a bent glass substrate is shown. Scale bar is 500 μm. The yellow box near the center of the image is the selected area (2100 μm × 6 μm) that was mapped using a Raman microscope. The apex of the bent substrate is marked by the dotted white lines and has a strain of 0.032%. (b-d) Raman maps of the selected area under various polarizations (0°, 45°, and 90° respectively) of the electric field. Polarization is denoted by the white arrows and the legend shows the intensity of the Raman signal. Vertical artifacts in Raman maps are due to overlapping samples in horizontal rastering of collected signal.

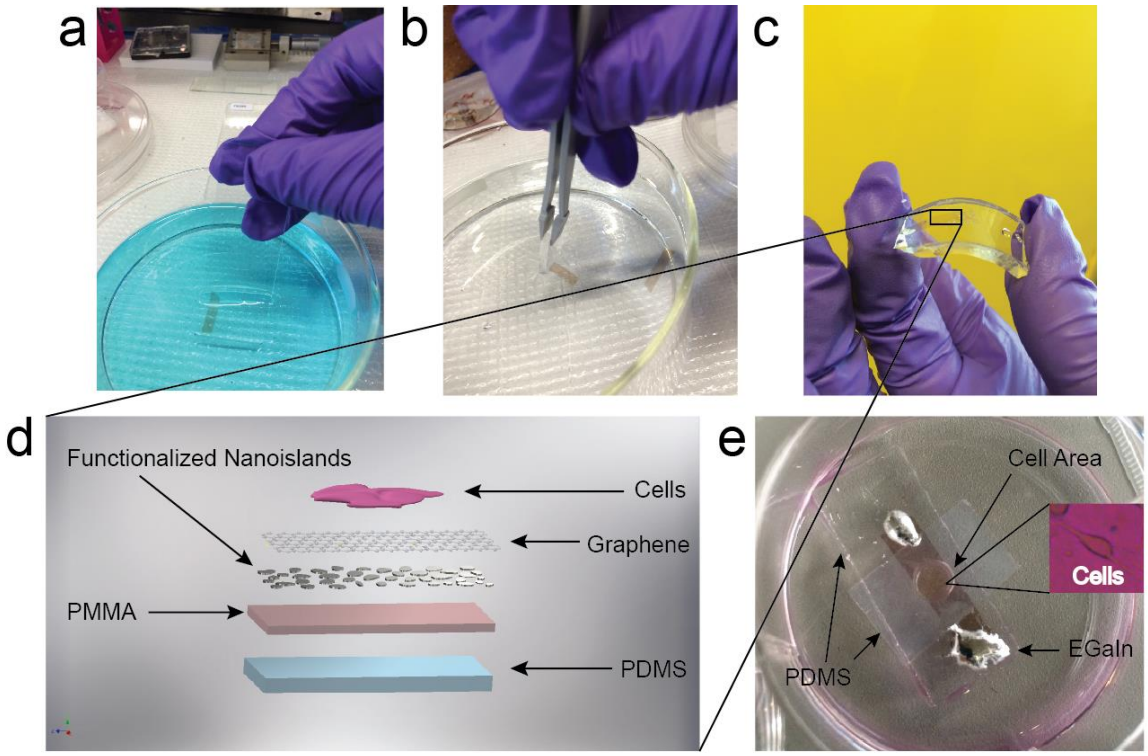

Figure C5. Silver Nanoislands for Muscoskeletal Cell Strain Detection. Camera images showing transfer of PMMA/NI_{func}/Gr samples onto glass from ammonia persulfate etching solution (a). Samples are transferred into a clean DI water container and transferred onto a PDMS slab graphene side up (b). Once on PDMS samples are remarkably flexible (c). A diagram showing the layers of the sample on the PDMS is depicted (d). A camera image of the final substrate with cells is shown in (e), note that there is a PDMS barrier added to contain liquid media to feed the cells and EGaIn contacts on the ends for electrical addressing. The inset in (e) depicts a myoblast cell image for illustrative purposes.

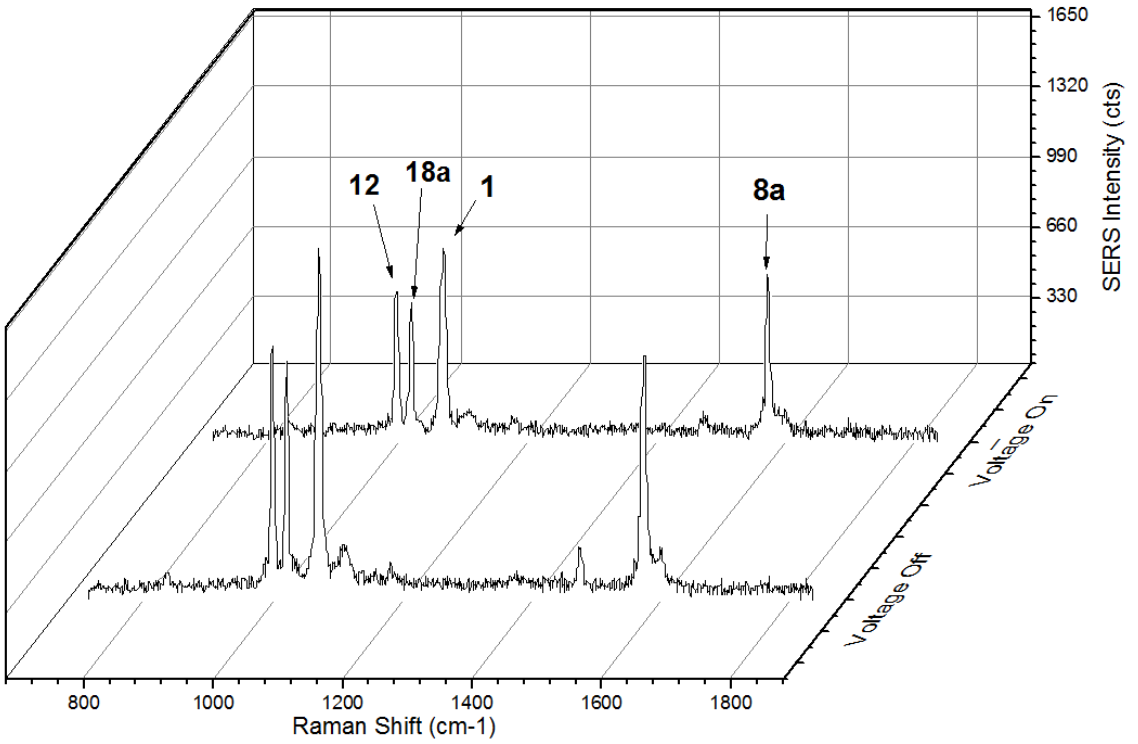

Figure C6. SERS spectra of myoblast cells on an inverted silver nanoisland substrate. The SERS spectra of benzenethiolate functionalized silver nanoislands under myoblast cells is depicted when a 2HZ/5V square wave voltage pulse is on and off. Note that the signal decreases as the voltage is turned on, suggesting that nanoislands are being pulled apart. It should also be noted that the signal of benzenethiolate dominates the spectra and there is a minimum amount of cross talk from the other materials on the substrate (cells/PDMS/PMMA). Vibrational modes for benzenethiol are labeled using Wilson notation for benzene derivatives.[1]

Acknowledgments

This work was supported by the National Institutes of Health Director's New Innovator Award, grant 1DP2EB022358-01 to D.J.L. and by a Diversity Supplement (for B.C.M.) under the same award number. A.S-C.C. was supported by the UC LEADS program, and E.A. received partial support from the CA-NASA/UCSD Space Grant Consortium. J.L. and S.C. are supported in part by California Institute for Regenerative Medicine (RT3-07899) and National Institutes of Health (R01EB021857). This work was performed in part at the San Diego Nanotechnology Infrastructure (SDNI), a member of

the National Nanotechnology Coordinated Infrastructure, which is supported by the National Science Foundation (Grant ECCS-1542148). B.C.M. would like to acknowledge the use of the UCSD Cryo-Electron Microscopy Facility which is supported by NIH grants to Dr. Timothy S. Baker, the tireless efforts of Dr. James Bouwer, and a gift from the Agouron Institute to UCSD. The authors acknowledge Prof. Andrea R. Tao for use of her lab's Renishaw Raman Spectrometer which was purchased with a DURIP Grant (N000141310655).

Appendix C, in full, is a reprint of the material as it appears in *Nanoscale*, 2017, 6, 1292-1298. The Royal Society of Chemistry, 2017. Brandon C. Marin, Justin Liu, Eden Aklile, Armando D. Urbina, Andrew S-C. Chiang, Natalie Lawrence, Shaochen Chen, and Darren J. Lipomi. The dissertation author was the primary investigator and author of this paper.

References

(1) Wilson, E. B. The Normal Modes and Frequencies of Vibration of the Regular Plane Hexagon Model of the Benzene Molecule. *Phys. Rev.* **1934**.

Appendix D

Supporting Information for Chapter 6: Graphene-Metal Composite Sensors with Near-Zero Temperature Coefficient of Resistance

Brandon C. Marin, Samuel E. Root, Armando D. Urbina, Eden Aklile, Rachel Miller, Aliaksandr V. Zaretski, Darren J. Lipomi[a]

[a]*NanoEngineering Department, University of California, San Diego. 9500 Gilman Drive MC 0448, La Jolla, CA 92093-0448*

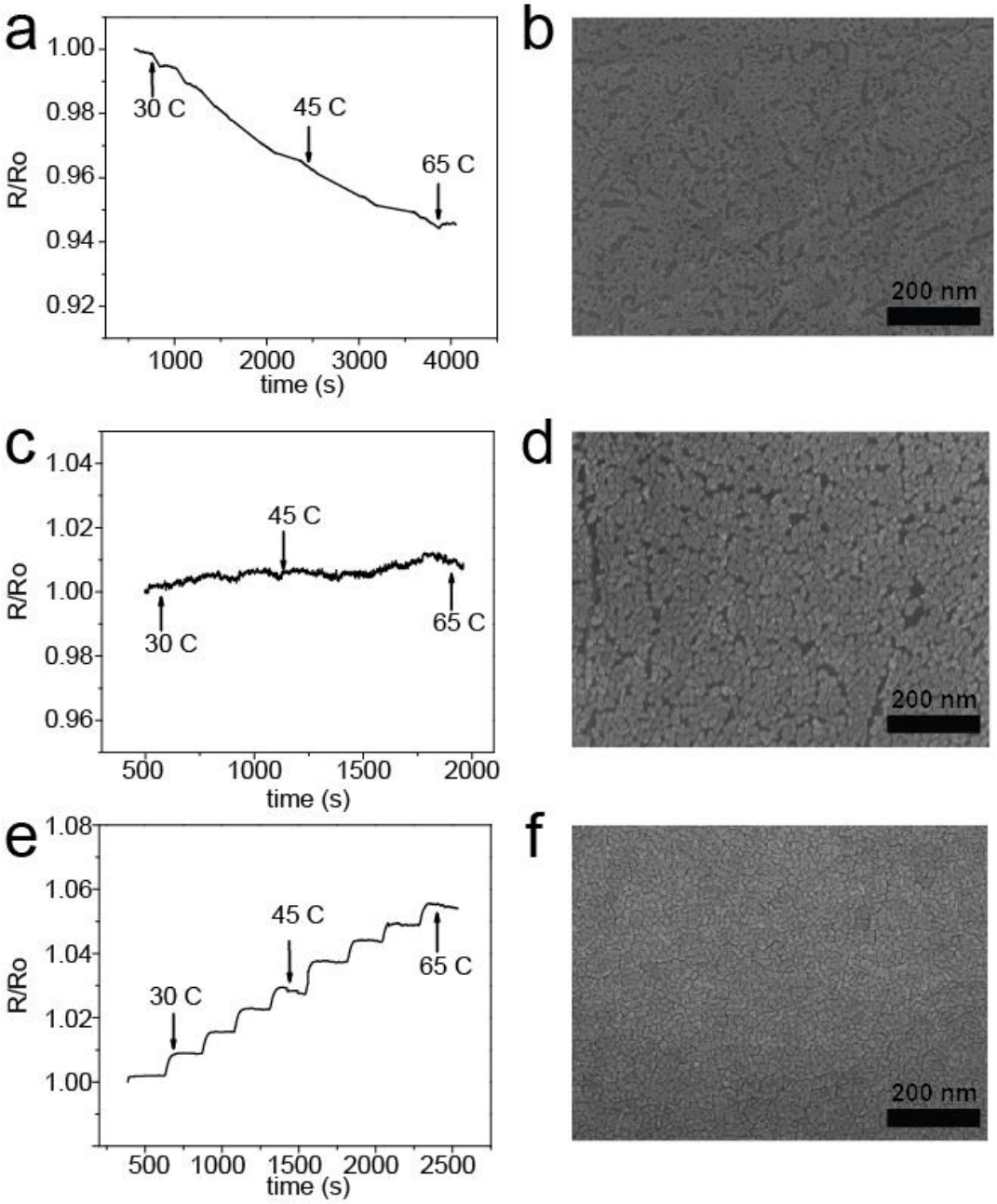

Figure D1. Thermal sensitivity and morphology of palladium nanoisland films. Normalized resistance as a function of time for palladium nanoislands of 0.5 nm (a), 0.9 nm (c), and 3 nm (e) films. The samples were heated from 30 C to 65 C over the course of the resistance measurement. SEM micrographs of 0.5 nm (b), 0.9 nm (d), and 3 nm (f) films are shown for comparison of the morphologies.

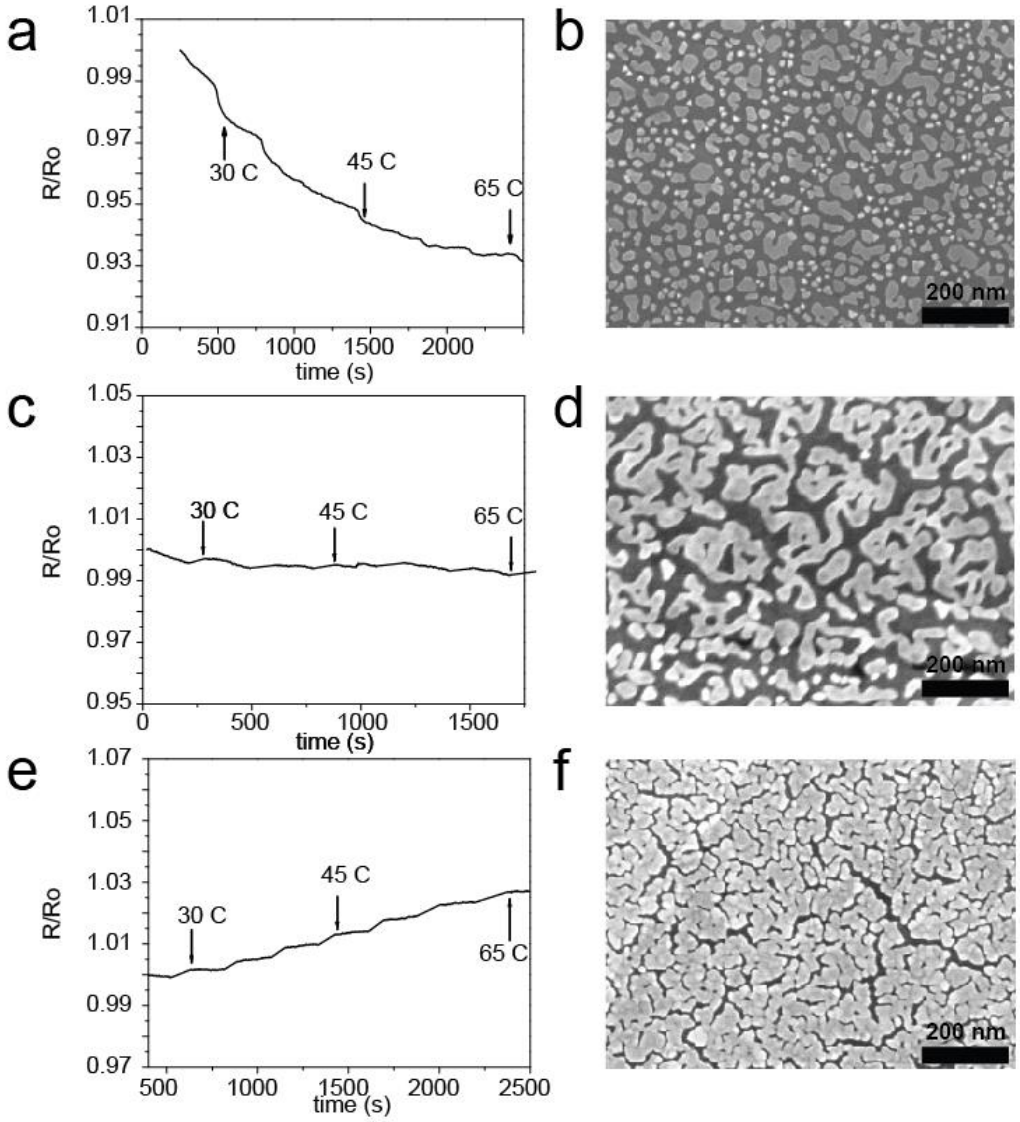

Figure D2. Thermal sensitivity and morphology of gold nanoisland films. Normalized resistance as a function of time for palladium nanoislands of 4 nm (a), 8 nm (c), and 11 nm (e) films. The samples were heated from 30 C to 65 C over the course of the resistance measurement. SEM micrographs of 4 nm (b), 8 nm (d), and 11 nm (f) films are shown for comparison of the morphologies.

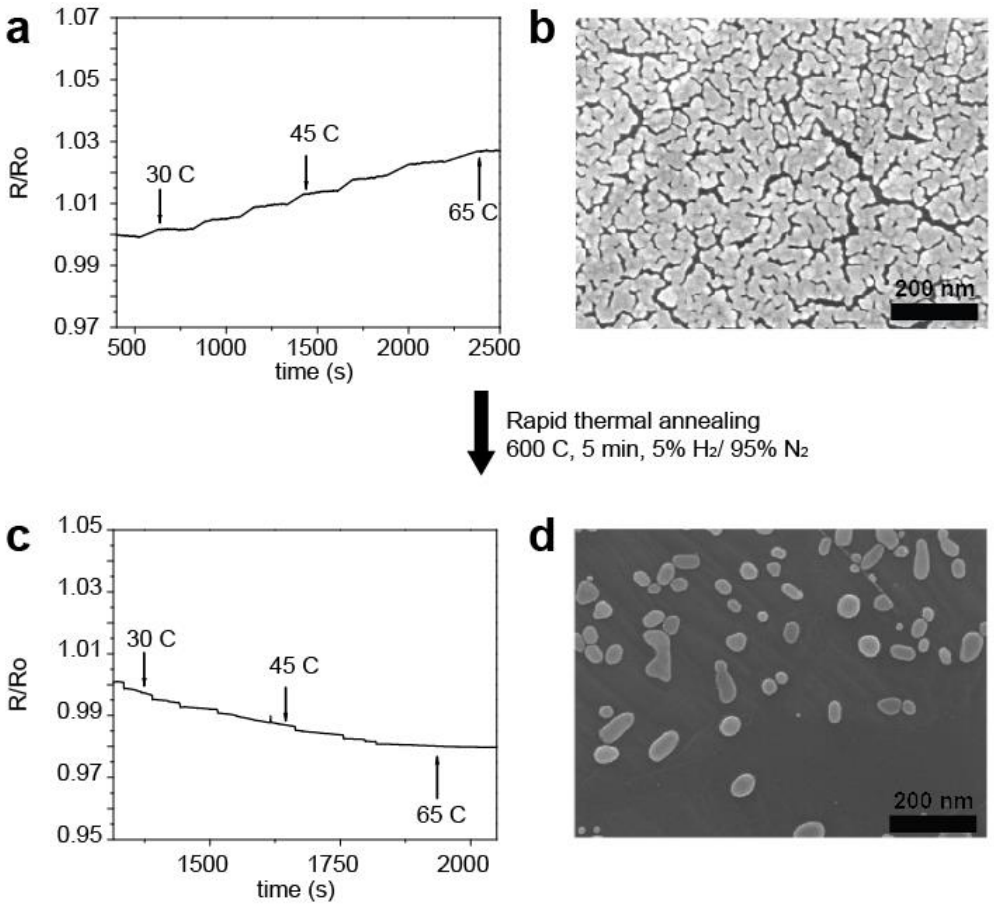

Figure D3. Effect of rapid thermal annealing on an 11 nm gold nanoisland sample. Normalized resistance as a function of time for an 11 nm gold nanoisland sample (a) and an SEM micrograph of the morphology. After rapid thermal annealing the normalized resistance as a function of time is shown (c) and the new morphology (d).

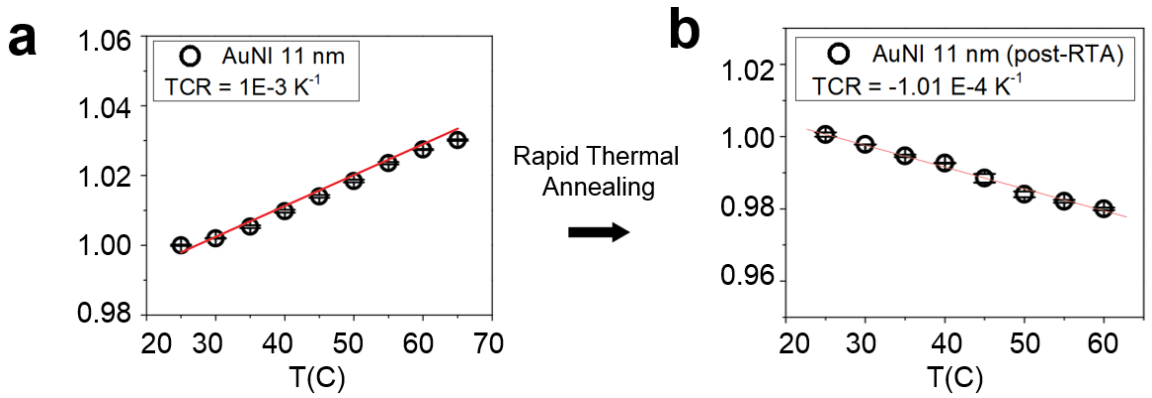

Figure D4. Effect of rapid thermal annealing on the thermal coefficient of resistance (TCR). The TCR of 11 nm gold nanoisland films is plotted before (a) and after (b) rapid thermal annealing.

D.1 Image Analysis.

SEM images were analyzed using a custom python code. This code is available freely at (https://github.com/seroot/SEM_Image_Analysis). An overview of the analysis is given in **Figure D5**. First, an SEM image in the .tif format is imported and an SEM_IM object is instantiated. Next, the bottom of the image is cropped out, and a threshold is defined using Otsu's method, as implemented in the Mahotas python image analysis package. Finally, distinct islands are labeled separately and various properties are computed including (1) coverage and (2) pixelated area of distinct islands. The quality of the image analysis is inherently limited by the resolution of the SEM image. While the algorithm works nicely for gold nanoislands, it has problems with the palladium nanoislands because of limitations on SEM resolution and contrast between the two materials.

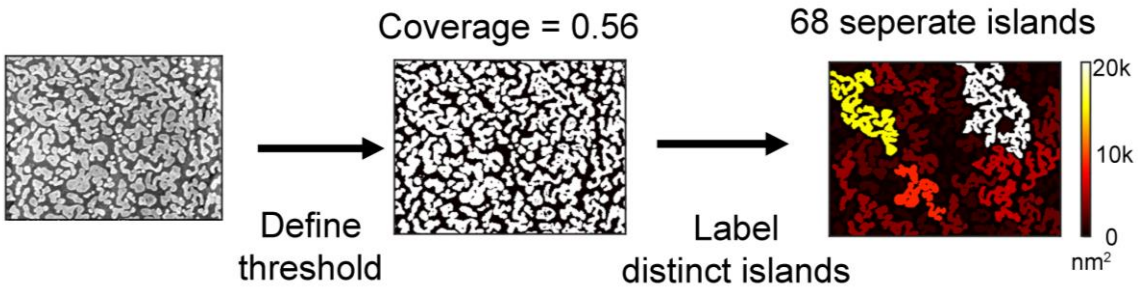

Figure D5. Image analysis of scanning electron micrographs. The flow for processing micrograph images is shown, a threshold for contrast is defined which allows nanoislands to be discerned from the underlying graphene. Average surface areas for nanoislands can then be determined.

D.2 Composite Model

A model was developed to describe the effect of surface coverage and nominal deposition thickness on the TCR of the composite material. Thin films of gold have been demonstrated to exhibit a TCR that depends on thickness. Adomov et al.[2] have proposed the following relation to describe this behavior:

$$\alpha_{Au} = \alpha_o \left(1 + \frac{3l}{8d}\right)^{-1}$$

Here α_{Au} is the TCR of the gold thin film, α_o is the bulk TCR of gold (3400 PPM), d is the thickness and l is the electron mean free path of gold (400 Å). This equation shows that the TCR of gold decreases with thickness following the trend shown in **Figure D6a**. The average thickness of the gold islands can be approximated as

$$d = \frac{d^*}{\theta}$$

where d^* is the nominal thickness that is measured using a quartz crystal microbalance and θ is the surface coverage computed from the image analysis.

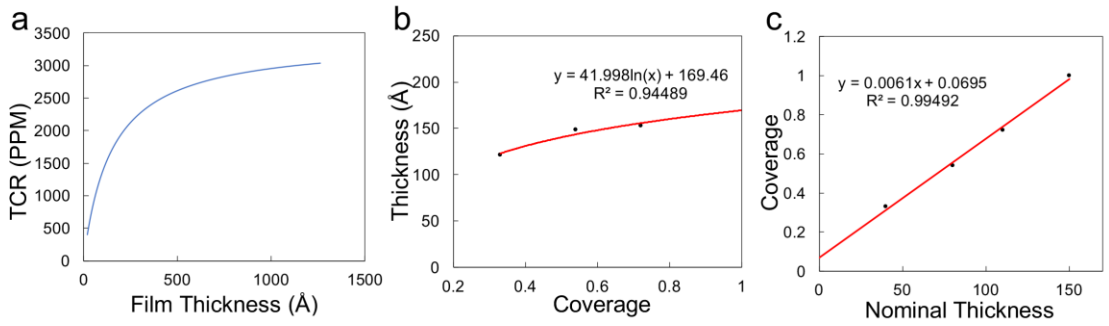

Figure D6. Theoretical Models on the TCR. Adomov's model on the relation between TCR and film thickness is shown (a). Coverage as a function of true film thickness (b). The coverage is plotted as a function of nominal thickness, as measured by QCM.

As shown in **Figure D6b**, the actual thickness of the islands does not increase strongly with nominal deposition because most of the added material goes towards increasing the surface coverage, until the surface is completely covered, at which point the nominal thickness and the actual thickness should be approximately equal. Furthermore, as shown in **Figure D6c**, we observed that in the surface coverage was linearly related to the nominal deposition thickness in the island regime ($\theta < 1$).

Assuming surface coverage as the relevant fractional variable (as opposed to mass or volume fraction), we incorporated these relations into a composite theory based on the following expression:

$$\alpha_c = \theta\alpha_{Au} + (1-\theta)\alpha_{Gr}$$

where α_{Gr} is the TCR of graphene, which we measured to be approximately -3000 PPM. After some algebra, the following expression can be obtained:

$$\alpha_c = \alpha_{gr} - \theta\left(\frac{\alpha_o}{1+\frac{3l\theta}{8d^*}} - \alpha_{gr}\right)$$

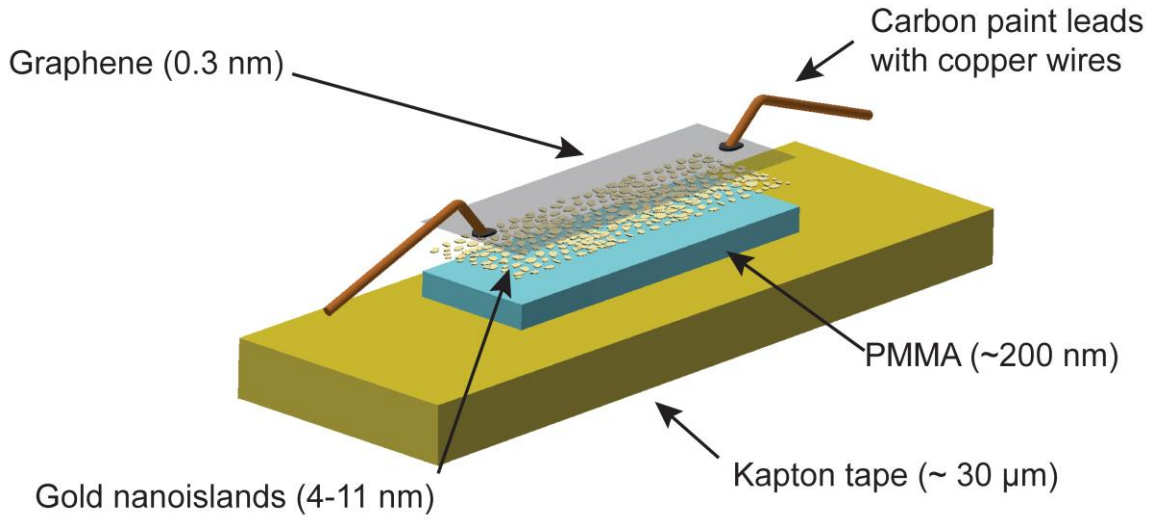

Figure D7. Schematic drawing of a near-zero TCR wearable sensor. A schematic is shown showing the order of thin film layers on a wearable sensor and their thicknesses.

Acknowledgments

This work was supported by the National Institutes of Health Director's New Innovator Award, grant 1DP2EB022358-01 to D. J. L., and by a Diversity Supplement (for B. C. M.) under the same award number. E. A. received partial support from the CA-NASA/UCSD Space Grant Consortium. This work was performed in part at the San Diego Nanotechnology Infrastructure (SDNI), a member of the National Nanotechnology Coordinated Infrastructure, which is supported by the National Science Foundation (Grant ECCS-1542148).

Appendix D, in full, is a reprint of the material as it appears in *ACS Omega*, 2017, 2(2), 626-630. The American Chemical Society 2017. Brandon C. Marin, Samuel E. Root, Armando D. Urbina, Eden Aklile, Rachel Miller, Aliaksandr V. Zaretski, and Darren J. Lipomi. The dissertation author was the primary investigator and author of this material.

References

(1) Coelho, L. P. Mahotas: Open Source Software for Scriptable Computer Vision. *J. Open Res. Softw.* **2013**, *1* (1), 1–13.

(2) Adamov, M.; Perovic, B.; Nenadovic, T. Electrical and Structural Properties of Thin Gold Films Obtained by Vacuum Evaporation and Sputtering. *Thin Solid Films* **1974**, *24* (1), 89–100.